TECHNISCHE UNIVERSITÄT WIEN

MASTER THESIS

Photopolymerization-assisted freeze-templating of polymer-derived ceramics

TU Wien
Institute of Chemical Technologies and Analytics
Getreidemarkt 9/164
1060 Wien

under instructions of Assistant Prof. Dipl.-Ing. Dr.techn. Thomas Konegger
and Ao.Univ.Prof. Dipl.-Ing. Dr.techn. Roland Haubner

by

Gregor Mikl BSc

Fallgasse 1/24
1060 Wien

Wien, November 2018

Abstract

Macroporous polymer-derived ceramics were fabricated by developing and using a method for a process called photopolymerization-assisted solidification templating (PASST). The focus was kept on finding a structuring agent, which would provide a tubular unidirectional porosity in the final ceramic. Polyvinylsilazane was the used preceramic precursor and tetrathiol acted as a crosslinking agent. Two different photoinitiators for the photopolymerization step were tested, camphorquinone and Ethyl (2,4,6-trimethylbenzoyl) phenylphosphinate. The latter was faster and therefore implemented in the final method. Bearing in mind the various necessary prerequisites, four structuring agents were identified, and their performance tested during this thesis. These were camphene, bornyl acetate, p-xylene and dimethyl carbonate.

Camphene yielded dendritic pores whereas the other three caused the samples to have lamellar pores. Directionality was high with pore channels running through the ceramic. Various nucleating agents were examined to see if the microstructure could be refined. Si_3N_4 could be identified as acting very efficiently when used with bornyl acetate. Not only would the pore size get smaller, but the pore morphology also changed from lamellas to spirals and tubes. A special focus was therefore kept on bornyl acetate by varying the monomer content and examining its influence on several ceramic properties. Challenging difficulties like supercooling were faced and partly overcome.

The influence of structuring and nucleating agents on permeation behaviour, pore size, porosity, density, compressive strength and microstructure was studied. Mercury intrusion porosimetry, scanning electron microscopy and the immersion test method were utilized to obtain values for structural properties. Permeability was measured by designing a set-up, which could handle the delicate samples without destroying them prior to the measurement. Darcian permeability ranged from $2.56 \cdot 10^{-13}$ to $1.17 \cdot 10^{-10}$ m^2, Non-Darcian permeability from $2.21 \cdot 10^{-08}$ to $2.82 \cdot 10^{-5}$ m. Median pore opening diameters from 6.7 to 72.1 µm could be obtained. Apparent porosity showed values between 53.7 and 77.8 %. Depending on the structuring agent, compressive strength ranged from 0.69 to 50.76 MPa.

Kurzfassung

Makroporöse polymerabgeleitete Keramiken wurden unter der Entwicklung und Verwendung einer Methode, genannt photopolymerisationsunterstützter Gefrierguss polymerabgeleiteter Keramiken (photopolymerization-assisted solidification templating = PASST), hergestellt. Der Fokus lag darin, ein strukturgebendes Lösungsmittel zu finden, welches eine unidirektionale tubuläre Porosität in der fertigen Keramik erzeugen würde. Polyvinylsilazan wurde als präkeramisches Polymer und Tetrathiol als quervernetzendes Agens eingesetzt. Zwei verschiedene Photoinitiatoren, Campherchinon und Ethyl(2,4,6-trimethylbenzoyl)phenylphosphinat, wurden auf ihre Eignung im Prozess getestet. Der letztgenannte war in der Geschwindigkeit überlegen und wurde deshalb in die finale Methode implementiert.

Unter Beachtung aller notwendigen Voraussetzungen, die das strukturgebende Agens mitbringen musste, wurden vier verschiedene Lösungsmittel identifiziert und untersucht. Diese waren Camphen, p-Xylol, Dimethylcarbonat und Bornylacetat. Camphen erzeugte dendritische Poren, während die anderen drei vorwiegend lamellare Porosität hervorbrachten. Hohe Direktionalität mit Kanälen, die die ganze Keramik durchzogen, konnte beobachtet werden. Verschiedene Keimbildner wurden verwendet, um eine Verfeinerung oder Veränderung der Mikrostruktur zu bewirken. Si_3N_4 agierte sehr effizient darin, die Porengröße und Porenmorphologie von Keramiken zu verkleinern beziehungsweise zu verändern, wenn sie mit Bornylacetat als Strukturgeber hergestellt worden waren. Die Präsenz des ebengenannten Keimbildners bewirkte eine Änderung der Porenstruktur von lamellar zu spiralförmig, mit tubulärem Anteil. Ein spezieller Fokus wurde daher auf Bornylacetat gelegt. Die Monomerbeladung wurde variiert, um ihren Einfluss auf verschiedene Eigenschaften der Keramik zu untersuchen.

Der Einfluss von Strukturgeber und Keimbildner auf Permeationsverhalten, Porengröße, Porosität, Dichte, Druckfestigkeit und Mikrostruktur wurde studiert. Quecksilberporosimetrie, Rasterelektronenmikroskopie und das Immersionsverfahren wurden verwendet, um ebengenannte Eigenschaften zu bestimmen. Für die Permeabilitätsmessungen wurde ein spezieller Versuchsaufbau entwickelt, um eine Messung der sehr empfindlichen Proben zu ermöglichen. Die gemessenen Darcy-Permeabilitätswerte befanden sich in einem Intervall von $2.56 \cdot 10^{-13}$ bis $1.17 \cdot 10^{-10}$ m^2, die Non-Darcy-Permeabilitätswerte zwischen $2.21 \cdot 10^{-08}$ und $2.82 \cdot 10^{-5}$ m. Der Median für den Porenöffnungsdurchmesser betrug zwischen 6.7 und 72.1 µm. Die scheinbare Porosität bewegte sich in einem Bereich von 53.7 bis 77.8 %. Abhängig vom Strukturgeber wurden Druckfestigkeiten zwischen 0.69 und 50.76 MPa erreicht.

Acknowledgements

First and foremost, I want to thank Dr. Thomas Konegger and Prof. Roland Haubner for giving me the opportunity to do my Master Thesis in their research group. Thomas´ dedication as well as his friendly, patient, and helpful attitude cannot be stressed enough.

A thank you goes to all members of the Institute of Chemical Technologies and Analytics, especially Christina Drechsel and Johannes Rauchenecker, for providing a nice atmosphere during the experimental part of my thesis.

I want to thank the Institute of Applied Synthetic Chemistry, especially Sebastian Schörpf and Shaghayegh Naghdi, for their differential photocalorimetry and differential scanning calorimetry measurements.

I thank my girlfriend Cinthia for all her support through this time. Finally, I am thankful for my family who supported me through all ups and downs during the whole time of my studies.

Table of contents

1 Introduction

1.1 Motivation

Porosity is generally undesired in technical ceramics, since it leads to a decrease in a wide range of properties, compared to bulk material. Several advantages of porous cellular ceramics though, inherent to their architecture, have been drawing attention to this type of ceramics in the past decades. They can have open or closed porosity, are lightweight, they exhibit high specific strength and can withstand high temperatures [1]. High temperature resistance is a property which sets ceramics apart in general from lots of other material classes. High oxidation resistance is equally important for a lot of industrial applications, usually being provided by technical ceramics to some extent. Porosity in the ceramic itself can be useful for purposes like insulation, filtering or as catalyst support. Today, ceramics with an engineered porosity are required in several industrial fields including pharmaceutics, manufacturing and energy [2].

Porous ceramics can only rise to their full potential when size, shape and the amount of porosity can be controlled properly. Partial sintering, replica templating and direct foaming are all processing routes that allow for the control over structure and functional properties to a certain extent [3]. Working with sacrificial fugitives is another method that allows for the control of the microstructure. When searching for versatile processing routes with environmentally friendly fugitives, freeze casting has drawn quite an interest in recent years. When using freeze casting, pore formation is based on the phase segregation of a two-component system achieved via solidification [2]. The amount of porosity, as well as size and shape of the pores can be controlled by choosing adequate chemicals and processing conditions.

Liquid preceramic polymers, used as precursors, can be an alternative to ceramic powders in fabrication of porous ceramics. They have the advantage of being processible with standard polymer processing routes and have seldom been used in freeze casting to this day. Typical problems that arise when handling ceramic powders, like the stability of the suspension, heterogeneous particle size distributions or agglomeration, vanish when working with liquid preceramic polymers. New challenges like solubility of the components, melting point reduction, or supercooling of the casting solution arise.

To further develop the freeze casting technique, used with preceramic polymers, and maximize its potential, the mentioned challenges must be faced and conquered. A difficult subject like the control over the porosity of a ceramic structure, to which this Master Thesis was dedicated, requires a lot of effort and time.

1.2 Aim of this Thesis

The aim of this thesis was to fabricate a porous ceramic exhibiting parallel, unidirectional, open tubular porosity. A preceramic polymer, poly(vinyl)silazane, was the basis of all experiments, acting as the precursor, and being transformed into said ceramic through a series of steps. A recently developed process called “photopolymerization-assisted solidification templating” [4] was the method of choice, with which such a goal could be reached. This method included, listed in the correct order, the preparation of a casting solution, freeze casting of the solution, photopolymerization of the preceramic

polymer with the help of a photoinitiator, sublimation of the solvent, thermal post-curing of the sample, and pyrolysis.

A chemical had to be found that could act as a sacrificial fugitive, providing the necessary structure upon an applied freeze casting step. Several prerequisites had to be borne in mind, including a suitable melting point, vapor pressure, as well as inertness to and excellent solubility for poly(vinyl)silazane and other chemicals used in the process.

Freeze casting, being part of the used method, had to be optimized in terms of casting parameters such as the cooling rate. Comparison between two different photoinitiators had to be performed to decide, which one was better suited for the process. This had to be done by testing different irradiation times and different temperatures.

The changes in microstructure had to be observed when adding nucleating agents to the casting solutions, changing the solvent, or altering other parameters. Several different ways of characterization had to be performed to get a better understanding of the process and influence of the solvent. These included density and porosity measurements, compressive strength tests, permeability measurements, as well as looking at the microstructure with a scanning electron microscope.

Differential scanning calorimetry experiments had to be performed to get estimates for melting point and enthalpy of fusion of the used solvents. Differential photocalorimetry measurements had to be done with solutions of each of the tested solvents. This was to investigate the reaction kinetics of the photopolymerization at low temperatures.

2 Theoretical background

2.1 Polymer-derived ceramics

Polymer-derived ceramics (PDCs) are synthesized by pyrolysis of preceramic polymers. Polymer precursors represent inorganic/organometallic systems that provide ceramics with a tailored chemical composition and a closely defined nanostructural organization by a controlled atmosphere and proper thermal treatment during curing and thermolysis processes.
Traditional ceramics preparation follows the powder route which can require the presence of sintering additives and heavily constrains technical applications. With preceramic polymers, composite materials, ceramic fibers or layers can be produced. Polymer-forming techniques such as polymer infiltration pyrolysis (PIP), injection molding, coating from solvent, resin transfer molding (RTM) or extrusion are accessible to process or shape preceramic polymers.
PDCs possess enhanced thermo-mechanical properties with respect to creep and oxidation, phase separation or crystallization up to 1500 °C and higher. They have been studied for their use as structural ceramics for high-temperature applications.
The most known classes of PDCs are in the binary systems Si_3N_4, SiC, AlN, and BN, ternary systems SiCN, SiCO, and BCN, as well as in the quaternary systems SiBCN, SiCNO, SiBCO, SiALCN, and SiAlCO. Pentanary systems of PDCs have been reported in recent years as well. [5]

2.1.1 Synthesis of preceramic organosilicon polymers

Macroscopic chemical and physical properties of PDCs can be adjusted and varied to a large extent by the design of the molecular precursor. Complete pyrolysis of silicon-based polymers can be achieved at relatively low temperatures at or below 1100 °C. An oversimplified representation of the molecular structure of preceramic organosilicon compounds is shown in Figure 1. Modification of the preceramic polymer on molecular level is done by altering the group in the polymer backbone (X) and/or by changing the substituents (R_1 and R_2). Changing (X) will result in different Si-based polymer classes. The functional groups R_1 and R_2 influence thermal and chemical stability as well as solubility of the polymer. Optical, electronic and rheological properties can also be adjusted. Figure 2 shows the main classes of preceramic organosilicon polymers. [5]

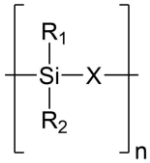

Figure 1: Oversimplified representation of the molecular structure of preceramic organosilicon compounds, after [5]

Educts for the synthesis of organosilicon polymers can be chlorosilanes, hydrosilanes, vinylsilanes, and alkenylsilanes. They enable polymerization by means of elimination, substitution or addition reactions. To be effective for the thermal decomposition process, preceramic polymers must fulfil some requirements. The molecular weight must be high enough to avoid volatilization of low molecular

components. Rheological properties and solubility should be compatible with the shaping process and latent reactivity has to be appropriate for the curing and cross-linking step. [5]

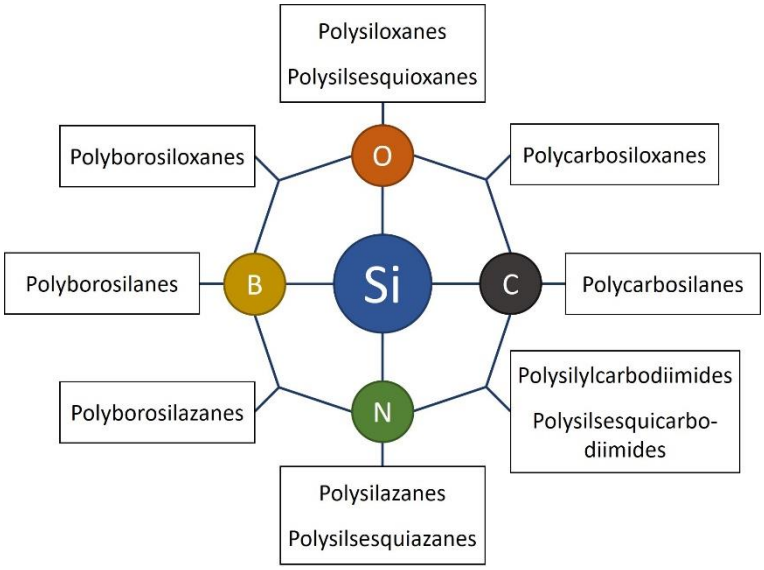

Figure 2: Main classes of preceramic organosilicon polymers, after [5]

2.1.1.1 Polyorganosilanes

Polyorganosilanes are composed of a Si-Si backbone with organic substituents attached to the silicon atoms. They show photo-conductivity, luminescence and high thermal stability. The earliest use for polysilanes was as preceramic precursors to β-silicon carbide. Other uses include semiconductors, hole-transporting materials and photoresists. Kipping [6] reported the first synthesis of a poly-(diphenylsilane) by a Wurtz-like coupling reaction of diphenyldichlorosilane with sodium in toluene in 1921. The reaction is shown in equation (1).

$$RR'SiCl_2 + 2\ Na \longrightarrow \left(RR'Si\right)_n + 2\ NaCl \qquad (1)$$

Despite some drawbacks like low yields and limited functional group tolerance, the old Wurtz-type reductive dehalogenation reaction, with some experimental modifications, is still the most viable general procedure for the preparation of high molecular weight, linear polysilane derivatives [7]. The catalytically dehydrogenative oligomerization of hydrosilanes in the presence of transition metal complexes proves to be an alternative [8, 9].

2.1.1.2 Polyorganocarbosilanes

The first approach for the synthesis of polyorganocarbosilanes was based on the thermal reorganization of a polymethylsilane to yield the polycarbosilane. This is known as the Kumada rearrangement. Figure 3 shows different types of precursors that can be used. The real structure, however, is much more complex containing Si-Si, Si-C bonds as well as hyperbranched structures.

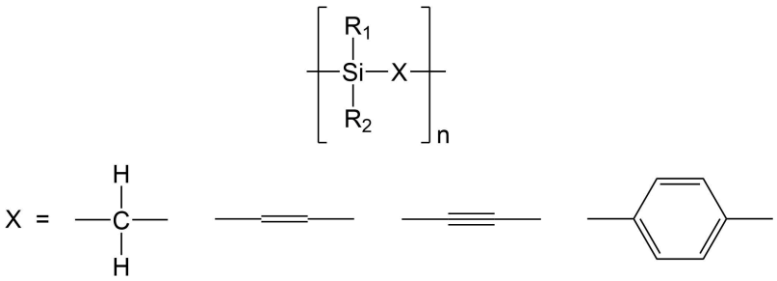

Figure 3: Types of polyorganocarbosilanes, oversimplified representation, after [5]

SiC-based fibers based on polymethylcarbosilane is the research topic where the most extensive studies were conducted. Polycarbosilanes as precursors for SiC-based fibers are used because of the high ceramic yield. [5]

2.1.1.3 Polyorganosiloxanes

Polyorganosiloxanes are widely used for sealing applications in construction. A great variety of usually inexpensive derivatives is commercially available. Polysiloxanes are usually synthesized by the reaction of chloroorganosilanes with water. A typical reaction is shown in equation (2).

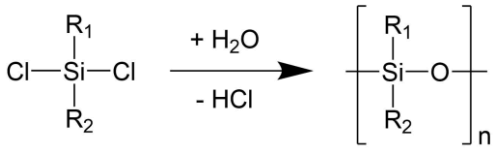

(2)

Silicon-rich polyorganosiloxanes, namely polysilaethers, have been synthesized in recent years combining the properties of polysilanes with those of polysiloxanes. Carbon-rich ceramics derived from polysiloxanes with a carbon content exceeding 20 wt% show enhanced stability against crystallization and high-temperature resistance. Cross-linked polysiloxanes can also be prepared via the sol-gel route through hydrolysis and condensation reactions of hybrid silicon alkoxides [5].

2.1.1.4 Polyorganosilazanes

The most common ways to create the Si-N bond are by ammonolysis or aminolysis of halo-genosilanes [10]. Other synthesis routes are also available and will be addressed later.

Ammonolysis of halogenosilanes

The halogenosilanes used for synthesis of oligo- and polysilazanes are produced on a large scale by the Müller-Rochow-Synthesis. The general synthetic route uses ammonia in an ammonolysis reaction to form silylamines out of the silane monomers. They can then condense to give (poly)silazanes. [11] Following are several different ways to get from the halogenosilane to the silazane:

Ammonolysis of monochlorosilanes R_3SiCl

The most important single source precursor for the preparation of Si/C/(N) from the gas phase is hexamethyldisilazane, or HMDS. Synthesis on industrial scale is performed by ammonolysis of chlorotrimethylsilane (equation (3)).

$$2\ (H_3C)_3SiCl + 3\ NH_3 \longrightarrow (H_3C)_3Si\text{-}NH\text{-}Si(CH_3)_3 + 2\ NH_4Cl \quad (3)$$

Possible solvents for this exothermic reaction are hexane, toluene and isododecane. The best performance is obtained when HMDS itself is used as a solvent. As long as the size of the substituents is comparable to methylgroups, like $(H_3C)(H_5C_2)_2SiCl$ [12], similar reactions with ammonia to form disilazanes can be observed. Chlorotrialkylsilanes with larger substituents tend to form primary silylamines R_3SiNH_2 [11, 13].

Ammonolysis of dichlorosilanes R_2SiCl_2

Reactions of dichlorosilanes with ammonia produce silazanes. This reactions are similar to the formation of linear and cyclic siloxane oligomers which are formed by hydrolysis of dichlorosilanes [14]. The size of the substituents as well as the reaction conditions influence the type of product gained from the reaction. Linear and cyclic oligomers will form in a mixture which can be separated by distillation.

These low molecular weight oligosilazanes have a volatility which usually is too high to serve as pyrolytic precursors for silicon nitride or silicon carbonitride. Special gas-phase pyrolysis methods or autoclave techniques are usable, though. Vinyl-functionalised silazanes assist in achieving an appropriate molecular weight and degree of cross-linking in the polymer. It is possible for the C=C-double bond to react with Si-H-, N-H-, or with other vinyl groups. The additional cross-linking is induced thermally or catalytically. [11]

The major cross-linking reactions are hydrosilylation of the vinyl groups in α- or β-position. Transamination reactions, dehydrocoupling reactions and polymerisation of the vinyl groups may also contribute to three-dimensional cross-linking, but to a smaller extent. Choosing different chlorosilanes and using amines instead of ammonia to prepare the polymer allows for a control of the type of occurring cross-linking reaction. [11, 15, 16]

Ammonolysis of trichlorosilanes $RSiCl_3$

Trichlorosilanes form monomeric, oligomeric or polymeric silazane compounds. Oligomeric and polymeric alkylsilsesquiazanes have been synthesised since the nineteen-sixties. A standard ammonolysis reaction using a 15 – 20 % solution of a trichlorosilane in benzene and dry gaseous ammonia at 15 – 20 °C [17] is shown in equation (4):

$$RSiCl_3 + 4.5\ NH_3 \longrightarrow 1/n\ [RSi(NH)_{1.5}]_n + 3\ NH_4Cl \quad (4)$$
$$R = -CH_3, -C_2H_5, -C_6H_{13}, -C_7H_{15}, -C_8H_{17}, -C_9H_{19}$$

Yields ranged from 11 – 56 % and oligomeric products with n = 6 and 8 could be isolated in this reaction [17]. It is practical to use trichlorosilanes and dichlorosilanes together to produce silazane precursors for Si/C/N-ceramics because the degree of cross-linking can be increased [11].

Ammonolysis of tetrachlorosilane $SiCl_4$

Ammonolysis of tetrachlorosilane leads to a polymeric solid, silicon diimide $[Si(NH_2)]_n$, provided that enough ammonia is used. Pyrolysis at 800 – 1100 °C leads to the formation of amorphous Si_3N_4. [11]

Ammonolysis of chlorosilane mixtures – copolysilazanes

Different silane mixtures can be used to prepare polysilazanes. The properties of the produced polymers can be controlled by simply varying the stoichiometry with monochlorosilanes acting as chain stoppers et cetera. [11]

Aminolysis of chlorosilanes

Amines can replace ammonia in the above described reactions to obtain precursors for Si/C/N-ceramics. Tertiary amines cannot be used because they do not react with chlorosilanes to form silazanes. Dichlorosilanes react with primary amines to give linear or cyclic oligomers. Secondary amines will react to form volatile molecular silylamines. They can be used for MOCVD (metal-organic chemical vapour deposition) due to their volatility. [11]

Hydrazinolysis of chlorosilanes

Si/C/N precursors can also be produced from chlorosilanes by a hydrazinolysis reaction. Hydrazine can be used to achieve nitrogen-rich precursors for the preparation of silicon nitride [18]. Hydrazine, H_2N-NH_2, is a strong base and behaves chemically similar to ammonia. Hydrazine forms HCl and Si-N bonds with chlorosilanes. Replacement from one up to all four hydrogen atoms of the hydrazine molecule with silyl groups is possible. [11]

Silazanolysis of chlorosilanes

The formation of HCl or the corresponding ammonium chloride is a problem which always arises when chlorosilanes are transformed into oligo- and polysilazanes. The separation of the side product is usually done by filtration. This problem can be overcome in an elegant way by using redistribution reactions of the following type (equation (5)):

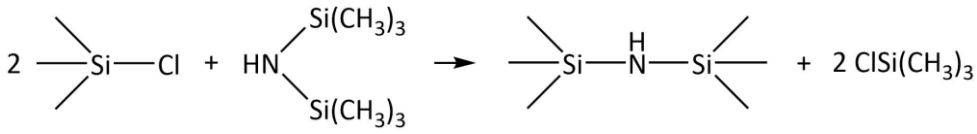

(5)

The high volatility of the chlorine-containing side product chlorotrimethylsilane is the biggest advantage of this approach because it can easily be removed by evaporation. [11]

2.1.1.5 Polyorganosilylcarbodiimides

Polyorganosilylcarbodiimides yield SiCN ceramics upon thermal decomposition. Their molecular structure looks as follows (equation (6)):

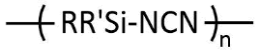

(6)

Compared to the polysilazanes, which also yield SiCN ceramics, they are more air-sensitive and exhibit enhanced thermal stability. The R and R' side groups, being for instance phenyl groups, are responsible for the raise of the carbon content in the final ceramics. The thermal stability of the SiCN ceramic is then enhanced because of the higher carbon content. [5, 19]

2.1.2 Processing of preceramic polymers

2.1.2.1 Shaping and cross-linking

The polymeric nature of preceramic polymers allows for an extensive variety of different forming methods. Table 1 contains shaping techniques applied to preceramic polymers. The precursor usually is a cross-linkable liquid, a meltable and curable solid, or an unmeltable but soluble solid. Some advantages of preceramic polymers include the following: They do not exhibit drying problems, the processing times for gelation and drying can be kept short and no flammable solvents are necessary. Furthermore, their solutions are quite stable in time, they can be processed in the molten state, and machining before ceramization avoids problems connected to tool wear and brittle fracture upon finishing of the component. [5] A unique feature surely is the possibility of using catalyst-containing preceramic polymers to create nanostructures directly during the pyrolysis [20].

Table 1: Techniques applied to preceramic polymers to manufacture a shaped-ceramic component, after [5]

Shaping technique	
◦ Casting/freeze casting	◦ Rapid prototyping
◦ Impregnation/infiltration	◦ Ink jetting
◦ Tape casting	◦ Electro-hydrodynamic-spraying/spinning
◦ Coating (spraying, dip- or spin-coating, chemical vapor deposition)	◦ Aerosol spraying
◦ Pressing (cold/warm-uniaxial, cold-isostatic)	◦ Self-assembly
◦ Injection molding	◦ Blowing/foaming
◦ Extrusion	◦ Microfluidics processing
◦ Fiber drawing	◦ Emulsion processing
◦ Machining	◦ Joining
◦ Microcomponent processing (UV/X-ray lithography, nano-/microcasting, replication, microextrusion, embossing/forging)	◦ Formation of nanostructures (tubes, fibers, wires, cables, belts, coils), directly by pyrolysis

2.1.2.2 Addition of fillers

A typical problem during the polymer-to-ceramic conversion is the formation of cracks or pores, when the dimension is above a few hundred micrometres. This occurs mainly because of gas release and shrinkage during conversion. Introduction of fillers of various nature (polymeric, metallic, ceramic) and shape/dimension can help in fabrication of bulk components by reducing shrinkage or by providing means of escape for gases generated during pyrolysis [21]. Macroporous structures can be fabricated by using polymeric fillers like ultra-high molecular weight polyethylene (UHMW-PE) [22].

2.1.2.3 Polymer-to-ceramic conversion (and fabrication)

Figure 4 shows the thermal decomposition behaviour of silicon-based polymers. Depending on the type of precursor, amorphous SiC, $Si_xC_yO_z$ and $Si_xC_yN_z$ ceramics can be obtained after a thermal treatment at about 1000 °C. Different organic substituents will result in a different Si/C ratio in the ceramic. Thermal gravimetric analysis (TGA) is the method of choice, when a detailed study of the decomposition behaviour and a quantitative analysis are required.
The polymer-to-ceramic transformation is illustrated in Figure 5, showing the temperature zones for the different states from polymer to final ceramic. During the conversion organic moieties as well as Si-H, Si-OH, or $Si-NH_x$ groups are decomposed or eliminated. The flowing gas removes the decomposition gases during oven pyrolysis, which is the most widely used method. [23]

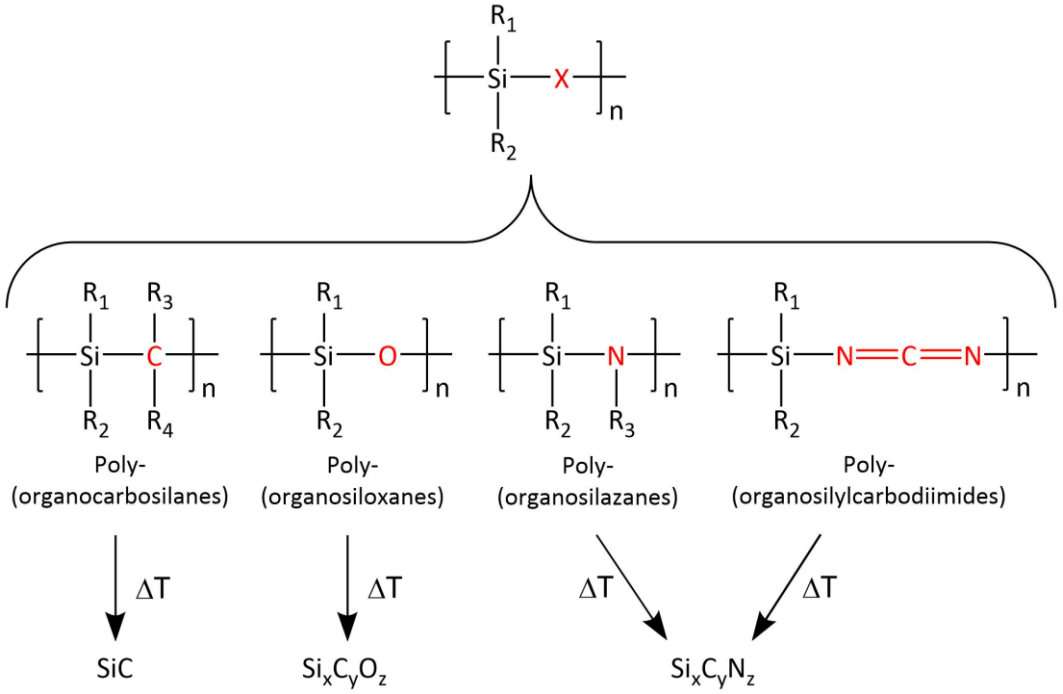

Figure 4: Thermal decomposition of silicon-based polymers, oversimplified molecular structure of the precursors, after [5]

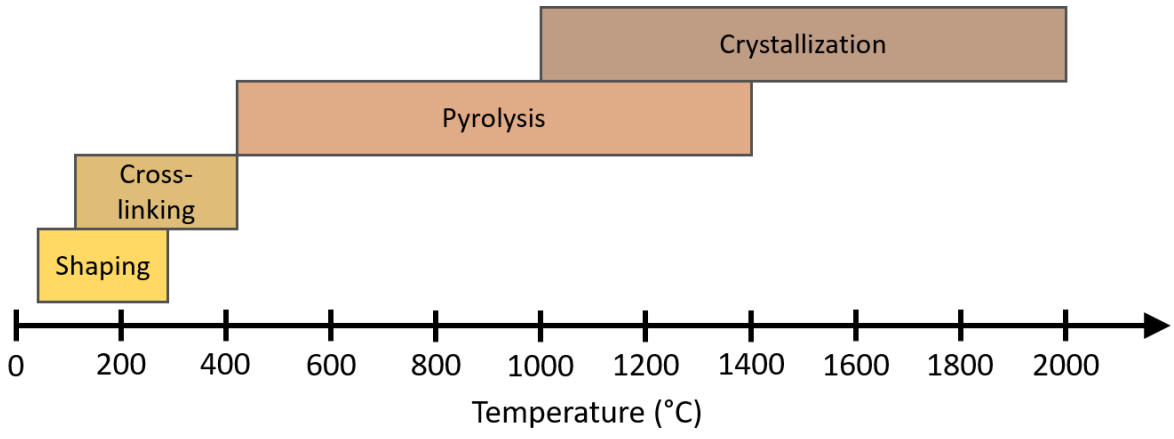

Figure 5: Polymer-to-ceramic transformation, temperature zones for different states, after [5]

Apart from the oven pyrolysis, a thermal consolidation method, several other thermal and non-thermal techniques are being used for the conversion from polymer to ceramic. These are hot isostatic pressing, hot uniaxial pressing, spark plasma sintering, chemical vapor deposition, plasma spraying, radiation pyrolysis, laser pyrolysis, microwave pyrolysis and ion irradiation. [5]

The fabrication of polymer-derived ceramics (PDCs) is influenced by several processing parameters. Microstructure, composition, density, ceramic yield and shape are some of the fundamental PDC features, that can and will be influenced by parameters like dwelling time, heating temperature, heating rate, atmosphere type, the characteristics of the precursor or by fillers. [5]

2.1.3 Microstructure of PDCs

The microstructure of the amorphous phase of the PDCs is responsible for the high-temperature properties like resistance to crystallization. Nanodomains persist up to very high temperatures in PDCs, which could be causing the remarkable resistance of PDCs to crystallization [24].
The initially amorphous network will start to redistribute its chemical bonds and phase separate at elevated temperatures. Nucleation and growth of nanocrystals follow. The separating “free” carbon phase undergoes a graphitization process. The amount of carbon not bonded to silicon in a ceramic is called “free” carbon. The microstructure can be analysed by numerous techniques such as XRD, Magic-Angle-Spinning-NMR (MAS-NMR), SAXS, FTIR, Raman spectroscopy, TEM, SEM and EELS. [5]
An investigation with MAS-NMR shows that polysilazanes yield a single-phase amorphous SiC_xN_y ($x + y = 4$) phase with Si bonding to C and N [25]. Figure 6 shows the molecular arrangement of ceramics obtained from polysilazane precursors.

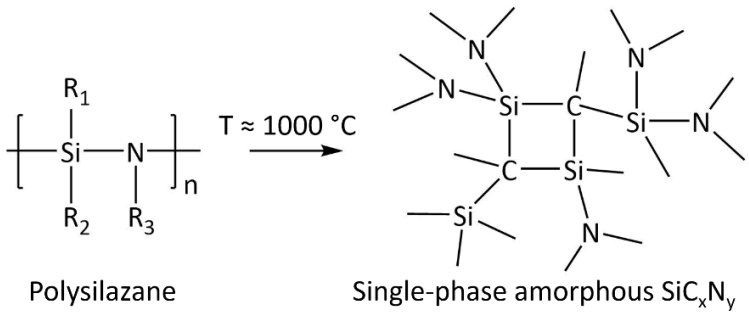

Figure 6: Molecular arrangement of amorphous SiCN ceramics derived from polysilazanes, after [25]

2.1.4 Properties of PDCs

Due to the large variety of precursors, PDCs exhibit a wide range of properties. When looking at electric properties for instance, the room-temperature DC conductivity varies up to 15 orders of magnitude (typically between 10^{-10} – 1 $(\Omega cm)^{-1}$). Magnetic properties are largely influenced by the addition of metals, for example iron. An elegant way to produce such kind of PDCs is to incorporate metallic iron in the backbone of the precursor by using substances like ferrocene. Since PDCs are generally black, the optical properties have not been studied overmuch. [5] Mechanical properties like the fracture toughness are hugely affected by the number of defects in the ceramic. Higher carbon content and pyrolysis temperature leads to a higher Vickers hardness [26]. Chemical properties are of special

importance to polymer-derived ceramics. Because of their high oxidation resistance, they can be used in high-temperature applications. A SiCO glass for example exhibits greater durability than pure silica glass in both acidic and basic media [27].

2.1.5 Applications of PDCs

Polymer-derived ceramics can be and are used as ceramic fibers, ceramic-matrix composites, highly porous components, microcomponents and coatings. Coatings are especially interesting because the preceramic polymers can be added with fillers and deposited on various kinds of substrates. C/C composites as well as carbon fibers have been covered with oxidation protection layers [28].

2.2 Fabrication of Porous ceramics

Many research efforts have been devoted in recent years to deliberately tailor sizes, amounts, shapes, locations, and connectivity of distributed pores in porous ceramics. This resulted in improved or unique properties and functions of porous ceramics. The goal in using porous ceramics is to combine intrinsic properties of ceramics with advantages, that dispersing pores in them, can provide. IUPAC classifies porous materials into three categories depending on the pore diameter. A material is deemed macroporous with pore diameters $d > 50$ nm, mesoporous with $2 \text{ nm} < d < 50$ nm, and microporous with $d < 2$ nm. [3]
Pores can be classified into two types: the first type, open pores, connects to the outside of the material whereas the second type, closed pores, is isolated from the outside and may contain a fluid. A special type of pores are penetrating pores, which have at least two openings located on two sides of a porous material.

The ceramics fabricated during this thesis were macroporous, which is why four representative processes for making macroporous ceramics are briefly introduced. These are partial sintering, replica templates, direct foaming and sacrificial fugitives. The aforementioned fabrication processes are depicted in Figure 7. [3]

2.2.1 Partial sintering

During sintering, particles of a powder are bonded due to evaporation-condensation processes or surface diffusion, enhanced by heat treatments. When the sintering is terminated before full densification, a homogeneous porous structure will form. The degree of partial sintering and the size of the starting powder control porosity and pore size, respectively. The microstructure is also greatly affected by factors such as the green density, the type and amount of additives, and the sintering conditions [29]. The mechanical properties heavily depend on the degree of neck growth between grains, as well as pore size and porosity. Porous materials generated by partial sintering usually show porosities below 50 %. [3]

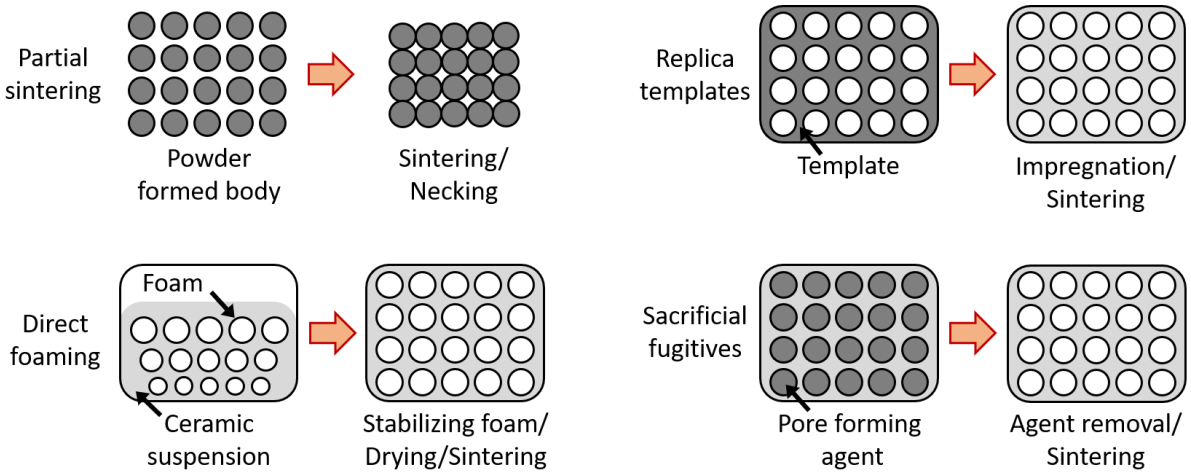

Figure 7: Fabrication processes of macroporous ceramics, after [3]

2.2.2 Replica templates

As a first step, a porous or cellular template is impregnated with a ceramic suspension or precursor solution. Natural cellular structures as well as synthetic templates like porous polymer sponges made of polyurethane are used. After getting soaked with the ceramic slurry or the precursor solution, the excess is usually drained and removed by roller compression or centrifugation. Viscosity and fluidity must be controlled to get a uniform ceramic layer over the sponge walls. The templates are dried, heat-treated and sintered to obtain the ceramic. The porosity can be higher than 90 % with interconnected open cells allowing fluids to pass through. The mechanical properties of ceramic reticulated foams are generally poor because of cracking of the struts during pyrolysis. One way to increase the compressive strength is to use vacuum infiltration of a ceramic slurry to fill up the struts in the presintered foam [30]. [3]

2.2.3 Direct foaming

According to Ohji et al. [3], “In direct foaming techniques, the ceramics suspension is foamed by incorporating air or gas and stabilized and dried, followed by sintering to obtain a consolidated structure.” The easy fabrication of ceramic materials with an exceptionally high porosity of 95 % or more and the low costs are clear advantages of this technique. [3] Continuous bubble formation in the ceramic slurry can be used to create unidirectional channels in porous ceramics. [31, 32] With this technique it is critical to stabilize the air or gas bubbles in the ceramic suspension to prevent coalescence due to thermodynamic instability. Direct foaming can also be performed by using preceramic polymer solutions instead of ceramic suspensions. [33]

2.2.4 Sacrificial fugitives

Porous ceramics can be created by mixing appropriate amounts of sacrificial fugitives as pore-forming agents with ceramic raw powder or preceramic polymer solutions. Evaporating or burning the fugitives out before or during sintering creates pores. Pore-forming agents can be classified into natural organic matters, synthetic organic matters, metallic and inorganic matters, and liquids. Polymer beads, organic

fibers, graphite, potato starch, charcoal, salicylic acid, liquid paraffin and coal are frequently used for pore formation.
The porosity can be controlled by the amounts of agents, whereas pore size and shape are affected by the size and shape of the agents. Pyrolysis is usually employed to remove solid fugitives like organic materials. Porous ceramics with unidirectional open channel-like porosity can be generated by using long fibers such as cotton thread [34] or natural tropical fiber [35]. [3]
One of the most frequently used approaches in recent years is freeze casting of water- or organic solvent-based slurries to produce unique structures in porous ceramics. Section 2.3 expands further on this topic, because freeze casting was the method used in this Master Thesis.

2.3 Freeze casting of porous ceramics

In freeze casting, pore formation is based on phase segregation of a two-component system achieved through solidification. A uniformly dispersed mixture consisting of a solid phase (e.g. alumina) and a liquid phase, usually water, is being frozen. The solidified liquid phase is acting as a sacrificial template. During solidification of the mixture the insoluble particles are being rejected at the freezing front to form an array of crystals, which are surrounded by “walls” comprised of solid particles. After completion of the freezing process, the sacrificial phase is removed through sublimation. The pore structure resembles the solidified liquid phase. Some important processing parameters, which have been studied, are particle size [36, 37], particle shape [38], freezing front velocity [39, 40] and choice of solvent. Phenomena like particle engulfment and sedimentation have to be taken into account as well when using suspension-based freeze casting [41].
Single-phase solutions have been used only in the recent past, with a focus on preceramic polymers. The process changes quite substantially, from segregation of a particulate suspension to solute rejection in a polymeric solution. Processing parameters like particle size and shape are no longer relevant. New factors such as polymer-solvent interactions and solvent compatibility must be considered. [2] The following is an example: SiC with dendritic pore structures can be made using polycarbosilane as a preceramic polymer and camphene as the solvent [42].

2.3.1 The freeze-casting process

A typical freeze-casting process can be divided into four steps, depicted in Figure 8. During the first step a stable suspension or a homogeneous polymer solution must be prepared. A mandatory requirement is that the temperature falls into a range where the solvent is liquid. Extra care must be taken when working with a suspension to avoid any segregation.
The second step, solidification, determines the characteristics of the future porosity and the structure is formed now. Continuous solvent crystals are grown. The direction and type of crystal growth depends on the solvent and if anisotropic or isotropic cooling is applied.
The third step follows directly after complete solidification, being the sublimation of the solvent. Reduced pressure and, if necessary, low temperature let the solvent sublimate and leave a green porous structure. The porosity resembles the solidified solvent structure.
In the fourth step, the green body is sintered with conventional sintering techniques or by pyrolytic conversion. Microporosity can be removed from the ceramic walls whilst retaining the macroporosity. [43]

A multitude of different ceramic materials have already been tested. This includes alumina [44], hydroxyapatite and tricalcium phosphate [45, 46], NiO-YSZ [47], Ni-YSZ [48], yttria-stabilised zirconia [49], titanium dioxide [50], silicon nitride [51], silica [52], silica-alumina [53] and silicon carbide [54]. Preceramic polymers such as polycarbosilane [42] and polymethylsiloxane [2] have also been investigated.

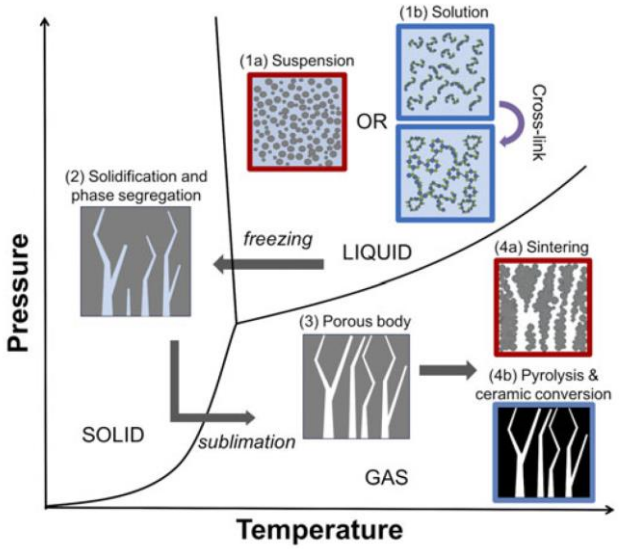

Figure 8: Schematic of the freeze-casting process for both suspension- and solution-based systems. (1a) A stable suspension or a (1b) homogeneous polymer solution (followed by partial cross-linking) is first prepared. (2) The temperature is lowered, initiating solidification and phase segregation. (3) A porous body is generated by sublimation of the frozen solvent. (4a) Sintering or (4b) pyrolysis of the ceramic or polymer, respectively, is performed to obtain a robust porous ceramic. (reprinted with permission from Cambridge University Press) [2]

2.3.2 Structure and properties of freeze-cast ceramics

The pore morphology can be varied, depending on the choice of solvent, slurries formulation / choice of preceramic polymer and the solidification conditions. When the sample is cooled with a carefully controlled temperature gradient, the solidification is directional with the porous channels often running from the bottom to the top of the samples.

The tortuosity of the porosity can be close to 1. In the case of water as a solvent, the ice front velocity along the fastest growing crystallographic axis is 10^2 to 10^3 times faster than perpendicular to this axis. In the case of camphene, clearly defined dendrites form upon solidification of the liquid camphene. The use of tert-butyl alcohol leads to prismatic channels [55]. Figure 9 shows typical microstructures obtained by freeze-casting of preceramic polymers. The resulting microstructure significantly changes with different solvents.

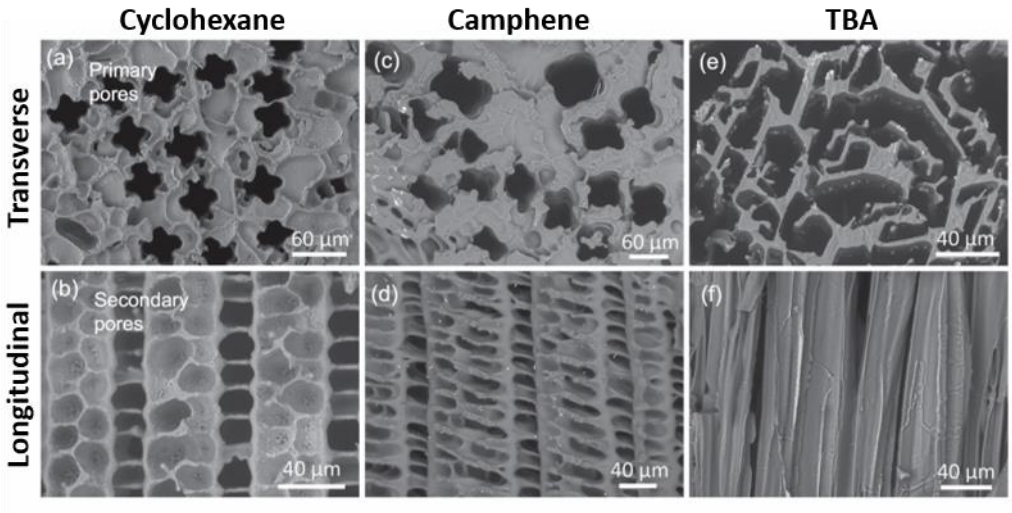

Figure 9: Effects of solvent choice on pore structure shown on SEM images; samples were made using (a, b) cyclohexane, (c, d) camphene, or (e, f) TBA, all with 20 wt% of a polysiloxane as preceramic polymer, (Silres® MK Powder, Wacker Chemie, $CH_3 – SiO_{1.5}$, Munich, Germany) (reprinted with permission from Elsevier) [56]

In most cases, the solvent crystals grow along the direction of the imposed thermal gradient. The occurring features at the surface of the pores, them being dendritic-like, lamellar or else, are homogeneous in size and distribution. Their relative size varies with the nature of the solvent, the freezing conditions, the characteristics of the educts (starting powder or preceramic polymer) and the sintering conditions. Ceramic bridges are another interesting occurring feature. They are locally bridging gaps in the structure. [43]

The type of solvent is of paramount importance to the resulting structure, and when looking for alternatives to existing solvents one has to bear in mind the following properties: solidification temperature, viscosity of the liquid, high vapor pressure in the solid state to allow reasonable conditions of temperature and pressure, a limited volume change at the phase transition and price considerations as well as environmental issues. Freezing kinetics also have a dramatic influence on the structure. A higher freezing rate leads to an increase of the solidification front speed and in further consequence to a refined microstructure. The final porosity relates directly to the volume of solvent in the suspension / solution. The porosity can range from 25 to 90 %. The pore morphology is influenced by several parameters which often are interconnected, the three main ones being the nature of the solvent, the freezing conditions and the particle size or type of preceramic polymer. The most critical one is the nature of the solvent, as the crystallographic properties of the solvent in its solid state define the main appearance of the structure. [43]

The required freezing time depends on the desired structure wavelength and the dimensions of the final piece. To this day most research was done with samples in the size range of 1 – 3 cm. With larger dimensions, maintaining the homogeneity of the temperature field and the freezing kinetics becomes increasingly difficult. Only a few properties of freeze-cast ceramics have been researched so far. One of the most critical properties is the compressive strength, especially for cellular ceramics. Dramatic improvements for potential candidates for bone replacement applications like hydroxyapatite were reported, when using water as a solvent [57].

2.3.3 Applications of freeze-cast ceramics

The structure of natural biomaterials like bone or nacre resembles the structure of porous ceramics [58], which makes freeze-casting particularly interesting for this kind of use. Applications that need open pore structures with good connectivity, low tortuosity, a large surface area and good mechanical properties can potentially profit from this technology. This includes SOFC, electrodes, sensors, filtration/separation devices and catalysts. Freeze-cast piezoelectrics with high hydrostatic figures of merit have been investigated, which could find use as transducers and actuators [59].

2.3.4 Crystal growth and the Jackson α-factor

The growth morphology of crystals is determined by the anisotropy of growth rates [60]. A higher growth rate for a specific crystallographic orientation results in a smaller participation in crystal form and it may even disappear from the crystal form. The crystallographic faces with low growth rates bound the crystal. Growth kinetics, which depend on the internal structure of the crystals and the external growth conditions, determine the growth rate and therefore the growth form of the crystal, seen from a statistical thermodynamics point of view. [61] The interface plays a large role for the growth morphology. Instabilities at the solid-liquid interface, as well as interfacial anisotropy lead to a breakdown of planar growth, resulting in different solidification microstructures. Correlation of the α-factor to the growth morphology of PDCs has already been done. [2] Figure 10 shows examples for two very different growth morphologies of crystals.

One method to correlate the interfacial anisotropy to the solidification microstructure is through the Jackson α-factor [62]:

$$\alpha = \frac{\eta}{Z}\frac{L}{kT_M} \tag{7}$$

η is the number of nearest neighbour sites adjacent to an atom in the plane of the interface. Z corresponds to the total number of nearest neighbours of an atom in the crystal. L is the enthalpy of fusion, k the Boltzmann constant, and T_M the melting point of the material. Large α-values predict smooth crystal faces on atomic scale resulting in faceted growth, whereas small α-values predict non-faceted growth. The factor η/Z is always less than 1, and $L/(kT_M)$ for metals typically 1, resulting in an α less than 2 for the metals. Their surfaces should therefore be rough on an atomic scale. Organic crystals as well as many minerals have values of $L/(kT_M)$ of 6 or similar, so they should have smooth faces which require surface nucleation. [62]

L/T_M is the entropy of fusion, which becomes, when dividing by k, dimensionless. It measures the difference in the degree of order between crystal and melt. The difference is small, when the crystallizing entities are spherical atoms or molecules. It becomes much larger, if a molecule must have the proper orientation to join the crystal. [62] Roughly speaking, when the α-value increases, the resulting microstructures should change from non-faceted to faceted, with an increase in anisotropy.

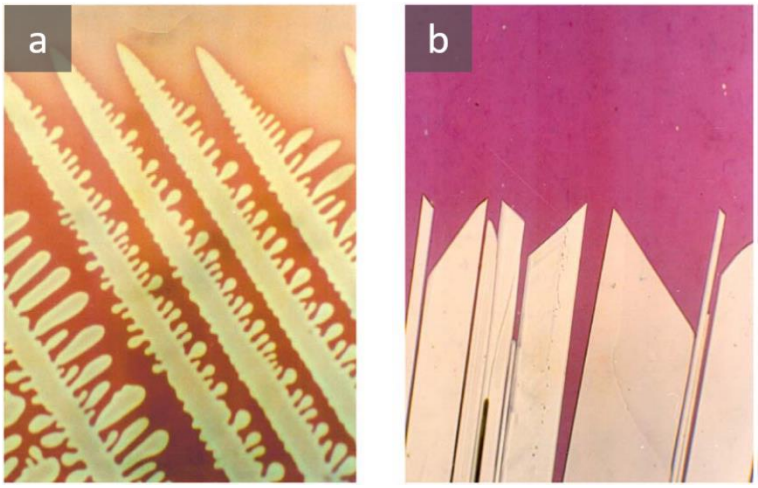

Figure 10: (a) Dendritically growing metal analogue, (b) Crystal showing well-developed facets. (With permission from Elsevier) [62]

2.4 Photopolymerization

2.4.1 Principles

During a polymerization reaction, many monomers, oligomers or prepolymers are added to each other, thereby creating a macromolecule. This reaction must be started by an initiation step, which corresponds to the decomposition of an initiator molecule usually obtained through a thermal process. An initiating species, e.g. a free radical, is produced, which can attack the first unit. Other units are now able to add on to form a macromolecule. [63]

Thermal activation can be replaced by other stimuli such as light, electron beam, X-rays, γ-rays, plasma, microwaves or pressure [64]. If a monomer/oligomer matrix is exposed to a suitable light source, the reaction is called photopolymerization reaction. Monomers or oligomers are usually not sensitive to the available lights, owing to their absorption properties. This makes the addition of a photoinitiator necessary. [63]

Typical sources of light can be conventional light sources such as mercury or xenon vapor lamps, laser beams, and light-emitting diodes (LEDs) [65]. Sunlight as a convenient and inexpensive source of light is used seldomly because of the restriction of the applications.

2.4.2 Photoinitiators for photopolymerization

The following types of photoinitiators are being used in photopolymerization: radical photoinitiators, cationic photoinitiators, anionic photoinitiators, as well as photoacid and photobase generators. [64] Radical photoinitiators were used in this thesis, which is why they shall be described further.

Radical photoinitiators

Photoinitiators, that work via a homolytic bond cleavage in the triplet state (type I photoinitiator) and lead to the generation of two radicals, are among the most efficient ones known to date. The cleavage usually takes place at a C-C or C-P bond at the α-position of a carbonyl group or at a C-S bond at the β-position of a carbonyl group.
Type II photoinitiators are using a two-component system based on a photoinitiator and a co-initiator. The co-initiator acts as a hydrogen donor (alcohol, amine, thiol, etc.). The process, were two radicals are formed, is either a direct hydrogen transfer or an electron transfer followed by a proton transfer. One of the radicals is formed on the photoinitiator and one on the hydrogen/electron donor. A polymer chain possessing labile hydrogens can also be a hydrogen donor. [64]

2.5 Thiol-ene Click chemistry

The relative weakness of the sulfur-hydrogen bond in thiols results in a plethora of chemical reactions with nearly quantitative yields, with an ability to initiate these reactions by several different methods under mild conditions. Two thiol reactions have been drawing special interest: The thiol-ene free-radical addition to electron-rich/electron-poor carbon-carbon double bonds, and the catalysed thiol Michael addition to electron-deficient carbon-carbon double bonds. Both mentioned reaction types are extremely efficient. The reaction of thiols with enes is the main focus in this thesis and shall be

described further. [66]
In principal, any non-sterically hindered terminal ene can participate in the radical-mediated thiol-ene process, with electron-rich and/or strained enes reacting faster than electron-deficient enes. These systems form cross-linked polymers that are the most ideal homogeneous network structures formed by free-radical polymerization to this day. [66]

Highly cross-linked polymer networks can be formed, when multifunctional monomers with an average functionality greater than two are utilized. They form via a step growth mechanism. Standard radical photoinitiators lead to the formation of thiyl radicals from thiols (Equation (8)). The propagation step involves the thiyl radical and a vinyl functional group (Equation (9)) and is followed by a chain transfer (Equation (10)) reaction. During this second step the thiyl radical is regenerated. Bimolecular radical recombinations can lead to the termination of the reaction, as seen in Equation (11). The addition of the thiol across the ene double bond is exothermic. [66] For a given thiol, electron-rich enes polymerize faster than electron-poor enes. [67, 68]

Thiyl radical formation:

$$RSH \xrightarrow[h\nu]{\text{Photoinitiator}} R\dot{S} \qquad (8)$$

Propagation [67]:

$$R\dot{S} + HCR'{=}CH_2 \longrightarrow R'\dot{C}H{-}CH_2SR \quad \text{(step 1)} \qquad (9)$$

Chain transfer [67]:

$$R'\dot{C}H{-}CH_2SR + RSH \longrightarrow R'CH_2{-}CH_2SR + R\dot{S} \quad \text{(step 2)} \qquad (10)$$

Termination [63]:

$$\begin{aligned} 2\,R\dot{S} &\longrightarrow RS{-}SR \\ 2\,R'\dot{C}H{-}CH_2SR &\longrightarrow RSH_2C{-}R'CH{-}R'CH{-}CH_2SR \\ R'\dot{C}H{-}CH_2SR + R''\dot{S} &\longrightarrow R''S{-}R'CH{-}CH_2SR \end{aligned} \qquad (11)$$

Literature reports show that four prominent thiol types typically are used for this sort of reactions. These are alkyl thiols, thiophenols, thiol propionates, and thiol glycolates. Tetrathiol (Pentaerythritol tetrakis(3-mercaptopropionate)) is a good example for a multifunctional thiol propionate, which was used in this thesis and in the literature [69].

Several critical problems are plaguing classical photopolymerization reactions, including inhibition by oxygen [70, 71], stress development and complicated volume relaxation [72, 73], complex polymerization kinetics [74, 75], and the formation of highly heterogeneous polymers/networks. [76, 77] The simple and robust mechanism of the thiol-ene photopolymerization reaction addresses each of these critical limitations by forming a homogeneous polymer network with significantly simplified polymerization kinetics, reduced stress and shrinkage, and insensitivity to oxygen inhibition. [66]

2.6 Differential scanning calorimetry (DSC)

2.6.1 Principles

Differential scanning calorimetry (DSC) is a technique for measuring the heat flow rate difference into a substance and a reference as a function of temperature while substance and reference are subjected to a controlled temperature program. This definition was taken from ASTM standard E473.
Figure 11 depicts the cross section of a typical DSC cell. Temperature measurement is being done with thermocouples. It is possible to purge the cell with inert gas via a gas purge inlet.

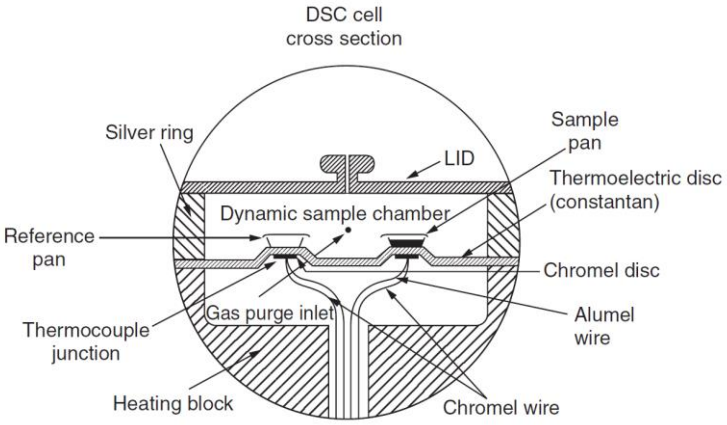

Figure 11: Cross-section of a typical DSC cell; Du Pont (now TA Instruments) 910, 2910, and 2920 DSC heat flux cell (Blaine, Du Pont Instruments bulletin; with permission from TA Instruments)

A DSC measurement provides information about thermal changes that do not involve a change in the sample mass. One of the most influential parameters which will affect the results is the purity of the sample. Impurities are the cause of shoulders on peaks and usually lower the melting point. Heating rate is also very important. An increase in the scanning rate increases sensitivity while a decrease leads to an increase in the resolution. To obtain thermal event temperatures close to the true thermodynamic value, slow scanning rates (e.g. 1–5 K/min) should be used.

DSC allows determination of the glass transition temperature (T_g), the heat capacity jump at the glass transition, the crystallization temperature (T_c), the melting temperature (T_m), heat of fusion, heat of reactions, very fast purity determination, fast heat capacity measurements, measurements of liquid crystal transitions and characterization of thermosets. Chemical reactions, such as cure, thermal and thermooxidative degradation, as well as the polymer crystallization can often be kinetically evaluated. [78]

A DSC curve shows endothermic events like melting, sublimation, solid-solid transition, desolvation and chemical reactions. Exothermic events include crystallization, solid-solid transition, decomposition and chemical reactions. The onset temperature is the extrapolated start temperature of a process. T_{onset} is defined by the extrapolated beginning of the curve. The beginning is defined by the point of intersection of the tangent with the point of maximum slope on the principal side of the peak, with the extrapolated base line.

2.6.2 Differential photocalorimetry (DPC)

Differential photocalorimetry (DPC) extends the application of DSC to measuring and quantifying the complete reaction of photo-cross-linkable materials by quantitatively measuring enthalpy or heat flow changes in a material during and after exposure to light. [78]

The sample is irradiated with light of a specific wavelength or spectrum of wavelengths while the DSC signal is recorded. The isothermal mode is almost always used for DPC runs. The first step is to equilibrate the unreacted sample at the desired isothermal temperature. Sample and reference are then irradiated with light of the desired wavelength which causes a shift in the DSC baseline. To identify the heat flow portion originating from the sample a second irradiation is being done which should, if the reaction is finished, only show the amount of heat introduced by the irradiation itself. Subtraction of the two curves results in a direct measure of conversion as a function of time. [78]

The cell should be purged with a high purity inert gas like argon, helium or nitrogen, since oxygen is a scavenger for free radicals formed in the visible light or UV radiation. Free radical photochemical reactions show very fast reaction rates which make it difficult for DPC instruments to follow since they do not have enough response time. Lower light intensities of the order of 10 mW/cm² can help to get accurate conversion data of the reaction. [78]

3 Experimental part

3.1 Set-up for photopolymerization-assisted solidification templating

3.1.1 The freeze caster

The freeze casting process calls for a suitable device to cool ceramic suspensions or solutions to low temperatures. The device should be based on a cooled plane to generate a freezing front with a controlled freezing front velocity. A freeze caster, called “Slurry-Kühler”, was built by staff of the Technical University of Vienna, namely Johannes Frank and Wolfgang Tomischko. The constructed device is a prototype.

The freeze caster is pictured in Figure 12. It uses liquid nitrogen as a cooling aid, which must be supplied by filling a polystyrene vessel to a certain height. Depending on cooling rate and temperature, a small motor lifts the vessel to a certain height, so that an aluminium cylinder immerses into the liquid nitrogen. A higher filling level of nitrogen and/or position of the vessel will result in a higher cooling rate. The aluminium cylinder is used for heat transfer from the sample, which is placed on top of the caster, usually in a cylindric mould. The freeze caster is equipped with a temperature control. Temperature measurement takes place directly below the surface of the aluminium plate, located on top of the freeze caster. The motor as well as the temperature sensor are connected to a PID process control unit. The freeze caster was built to reach a minimal temperature of -150 °C. Cooling rates can range from 1 K/min to approximately 10 K/min.

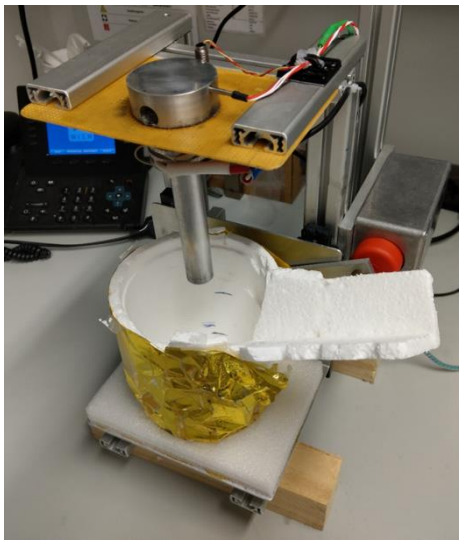

Figure 12: Freeze caster - "Slurry Kühler"; prototype built by Johannes Frank and Wolfgang Tomischko

3.1.2 Lamps used for photopolymerization

During this thesis, two different wavelengths were tested for photopolymerization. These were 470 nm and 400 nm. Two lamps had to be built, which could be used on top of the freeze caster. The lamps had to be manufactured in such a way, that the sample, being in the cylindrical mould, would get exposed to as close to a homogeneous irradiation from all sides as could be.

3.1.2.1 Lamp with 470 nm wavelength

The lamp with 470 nm wavelength was built by Richard Obmann, member of the research group, and can be seen in Figure 13. The lamp consists of a hexagonal array of 9 LEDs, which were positioned in a centrosymmetric manner. Heatsinks at the back of the LEDs prevent them from overheating.

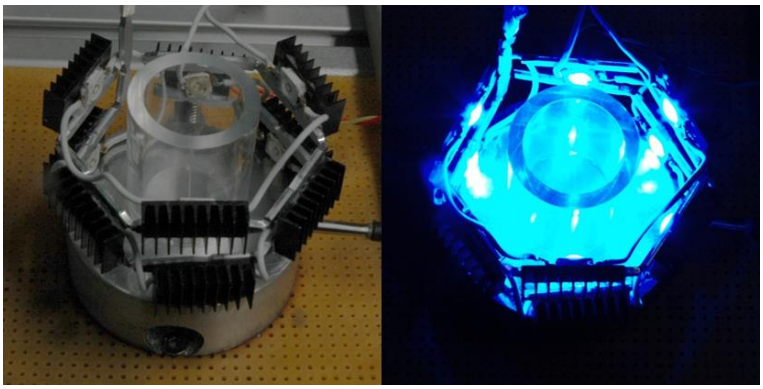

Figure 13: Lamp-array with 470 nm wavelength

3.1.2.2 Construction of a 400 nm lamp

The use of Ethyl (2,4,6-trimethylbenzoyl) phenylphosphinate as a photoinitiator called for a suitable lamp for the photopolymerization step during sample processing. Freeze casting was performed on a cylindrical aluminium block of 5 cm in diameter. A hexagonal lamp with an inner diameter of 5 cm that can be stuck onto the cylinder was built using the material in Table 2. The hexagon, which is the integral part of the lamp, consists of two aluminium plates. They were bent in 60° angles to get 4 faces on each plate. The two plates intertwined, and the overlapping planes were connected by applying heat paste in the centre framed by superglue. The 6 LEDs were glued onto the 6 inner sides of the hexagon. It is important to notice that each of the LEDs was mounted at the same height and in the horizontal centre of the plane. To enable better heat flux, heat paste was put at the centre of the back of the LEDs. It was then surrounded by a ring of superglue. The LEDs were connected in series with a stranded wire. After letting the superglue dry overnight the lamp was ready for use.

Table 2: Material used for building the 400 nm lamp

Material
Aluminium plate, 1 mm thick
Stranded wire
Superglue (Cyanacrylate)
Heat paste
6 LEDs, 400 nm
DC power supply

Specifications of the LEDs

The used LEDs with the product number PM2L-3LLE-LC are from ProLight Opto. The following Table 3 shows important parameters and characteristics of the diodes. The most important ones are the wavelength range of 390 – 410 nm and a typical peak wavelength of 400 nm. Figure 14 shows the color spectrum of the LEDs with the peak around 400 nm. The small inlay on the upper right is an actual picture of one LED. Figure 15 shows the lamp array in action. The light distribution inside seems to be quite homogeneous.

Table 3: Parameters & Characteristic of the 400 nm LEDs [79]

Parameters	
Maximum DC forward current	700 mA
Maximum LED junction temperature	120 °C
Operating board temperature at maximum DC forward current	-40 °C – 100 °C
Characteristics at 700 mA, T = 25 °C	
Peak wavelength, range	390 – 410 nm
Peak wavelength, typical	400 nm
Radiometric power	900 mW
Forward Voltage, typical	3.4 V
Viewing angle	130°

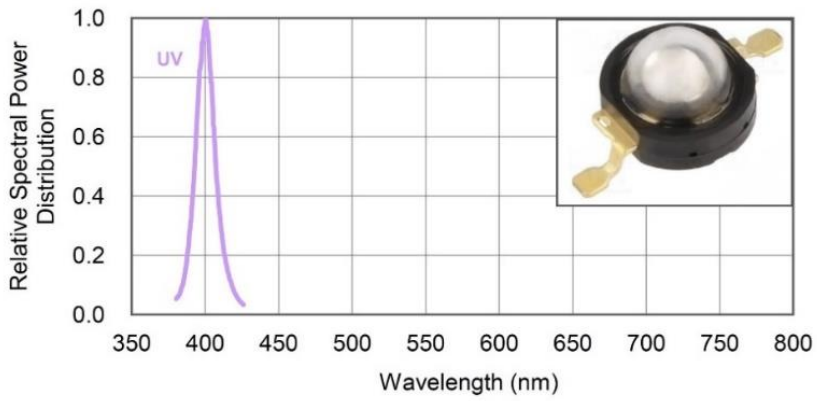

Figure 14: Color spectrum of the LEDs with peak maximum around 400 nm. The inlay at the upper right shows a picture of one LED [79, 80]

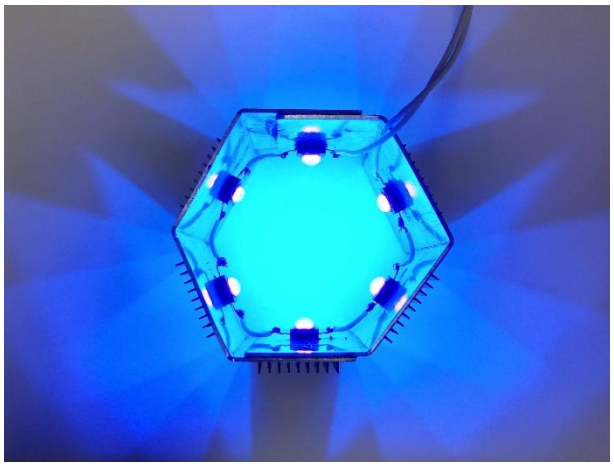

Figure 15: Lamp array with a wavelength of 400 nm working under 0.20 A and 18.9 V. The sample should be placed in the centre of the lamp to get best photopolymerization results.

3.2 Overview of Chemicals used during the experimental work

Table 4 lists all the chemicals that were used for experiments performed during the master thesis. The densities for the four solvents used in the final method can be found in Table 5.

Table 4: List of chemicals used for experiments during the master thesis

Name	CAS-Number	Formula	Purity	Producer
Benzyl benzoate	120-51-4	$C_{14}H_{12}O_2$	98 %	Merck
L-(-)-Bornyl acetate	5655-61-8	$C_{12}H_{20}O_2$	95 %	Alfa Aesar
(+)-Camphene	79-92-5	$C_{10}H_{16}$	95 %	Merck
Cyclohexane	110-82-7	C_6H_{12}	> 99 %	VWR
Cyclooctane	292-64-8	C_8H_{16}	> 99 %	Alfa Aesar
(±)-Camphorquinone (CQ)	10373-78-1	$C_{10}H_{14}O_2$	99 %	Alfa Aesar
Dimethyl carbonate	616-38-6	$C_3H_6O_3$	99 %	Lancaster
Ethyl (2,4,6-trimethylbenzoyl)phenylphosphinate (ETPP)	84434-11-7	$C_{18}H_{21}O_3P$	95 %	Lambson
Pentaerythritol tetrakis(3-mercaptopropionate) "Tetrathiol (TT)"	7575-23-7	$C_{17}H_{28}O_8S_4$	96 %	Aldrich
Polyethylene beads (GUR® X143)	-	$(C_2H_4)n$	-	Ticona
Polyvinylsilazane (PSZ) "Durazane® 1800"	-	$(C_3H_7NSi)0.2n$-$(CH_5NSi)0.8n$	-	durXtreme GmbH / Merck
Silicon carbide (α-SiC UF-25-A)	409-21-2	SiC	-	H. C. Starck
Silicon nitride (UBE SN-E10)	12033-89-5	Si_3N_4	-	UBE Industries
Silicon oxide (Aerosil® 200)	-	SiO_2	-	Degussa
p-Xylene	106-42-3	C_8H_{10}	99 %	Lancaster

Table 5: Densities of the four solvents used in the final method

Solvent	Density (g/cm³)
Camphene	0.85 at 20 °C [81]
p-Xylene	0.86 at 25 °C [82]
Dimethyl carbonate	1.06 at 25 °C [82]
Bornyl acetate	0.98 at 20 °C [83]

3.3 Initial procedure for the photopolymerization-assisted solidification templating

The following process describes the starting point of this master thesis. Prior work in the research group [4] led to the procedure as follows:

The chemicals needed for one experiment, meaning one freeze casting, are listed in the ansatz below. The mass ratio of Polyvinylsilazane (PSZ) : Tetrathiol (TT) = 2.7 : 1, which seems arbitrary, sets a molar ratio of vinyl groups in the PSZ to thiol groups in the TT of 1 : 1. The loading of PSZ + TT mounts to 25 wt% of the whole solution.

Ansatz:
1.095 g PSZ
0.405 g TT
4.5 g camphene
0.03 g camphorquinone

Preparation of the casting solution

At first, PSZ is degassed under stirring and with a reduced pressure of about 6 mbar until the solution is clear. This usually takes between 20 – 40 min. The TT is added, leading to the solution becoming cloudy, and stirred under the same reduced pressure as before. The cloudiness presumably stems from the formation of an emulsion upon addition of TT to PSZ. The stirring continues until the initially cloudy solution becomes clear. This takes between 40 – 120 min.

Camphene is mixed with the photoinitiator camphorquinone (CQ) and stirred at 55 °C until the CQ has dissolved, but for at least 10 min. This must be done with protection from ambient light. The elevated temperature is necessary because of the melting point of camphene being at around 50 °C. The PSZ/TT solution is mixed with the camphene/CQ solution and stirred at 55 °C for 15 min. The solution is now ready for freeze casting.

Freeze casting

The casting solution is put into a cylindrical PMMA (polymethylmethacrylate) mould. The mould has an inner diameter of 19 mm, a wall thickness of 3 mm and a height of 30 mm. The surface of the mould, especially the bottom, which contacts the aluminium casting plate is greased to prevent the solution from leaking out and the polymer from sticking to the mould. The mould is covered with a hood to prevent illumination from ambient light with a wavelength shorter than 500 nm during the casting.

In the next step, the freeze casting is done with a ramp of 8 K/min, starting at 55 °C. The temperature programme in detail runs as follows:

- 55 °C -> - 65 °C in 15 min, ramp 8 K/min
- -65 °C hold for 35 min, irradiation starts after 5 min holding time
- -65 °C -> -21 °C in 10 min
- -21 °C hold for 20 min
- -21 °C -> 0 °C in 10 min
- 0 °C hold for 20 min

Adding the times of the casting programme together, the total casting time amounts to 110 min. The freeze caster itself uses liquid nitrogen as cooling aid.

Photopolymerization

When the low temperature threshold is reached, after a waiting time of 5 min, the light protection hood is removed, and the 470 nm lamp attached. Illumination starts with 25 % of the maximum irradiation power of the used 470 nm lamp. It is turned to 50 % after 30 min, to 100 % after 60 min and switched off after 90 min. Looking at the temperature programme of the freeze caster, one can see that the 50 % power is used at -21 °C and the 100 %, as soon as 0 °C is the goal temperature.

Sublimation

The photocured sample must be removed from the mould. A wire is put at the interface between mould and sample and cautiously rotated once around the cylinder. Any bonds between sample and mould are severed this way. The sample can be removed by pushing it out of the mould. The top and bottom parts are cut off with a sharp knife to get evenly shaped samples.

The sample is placed onto a textile fabric, which has been mounted onto a plastic jar. The textile fabric enables ventilation from the bottom as well, since it is very permeable. This build-up is put inside a vacuum desiccator. A rotary vane pump is connected, and the sublimation started. After 24 h the process is stopped and the sample ready for thermal post-curing.

Thermal post-curing & Pyrolysis

The thermal post-curing step is done by placing the sample into an oven (wtc binder No. 940402), equipped with an inert gas retort. A constant flow of nitrogen with 0.3 l/min is applied. The heating rate is set at a constant 1 K/min, starting at room temperature and stopping at 200 °C. The 200 °C are held for 4 h. The oven is switched of afterwards and the sample unloaded once room temperature has been reached again.

Pyrolysis is done in a tube furncace which is equipped with a corundum tube, with a constant gas flow of 0.3 l/min N_2. The heating rate is set at a constant 1 K/min, starting at room temperature and stopping at 1000 °C. The 1000 °C are held for 2 h, followed by cooling to room temperature with a cooling rate of 2 K/min. During final curing and pyrolysis, potentially harmful odorous sulphur-containing compounds are set free. At temperatures well above 600 °C the smell stops. At these high temperatures the release of small gaseous molecules seems to decrease substantially. The pyrolyzed samples are always black in colour.

3.4 Preliminary experiments

Before progressing from the initially developed workflow, several preliminary experiments were conducted.

3.4.1 Solidification behaviour of PSZ & polymerization behaviour

To get an estimate of solidification behaviour and polymerization behaviour of PSZ, three experiments were performed. The weighed-out masses of the chemicals are listed in Table 6.

Table 6: Composition of solutions for solidification & polymerization behaviour; CQ = Camphorquinone, TT = Tetrathiol, ETPP = Ethyl (2,4,6-trimethylbenzoyl) phenylphosphinate

Experiment	PSZ	TT	Photoinitiator
MP_None	1.089 g	0.408 g	None
MP_ETPP	1.095 g	0.406 g	11 mg ETPP
MP_CQ	1.098 g	0.402 g	10 mg CQ

PSZ was degassed under stirring and vacuum until the formation of gas bubbles stopped. TT was added and the stirring under vacuum continued. After 90 min, the solutions had become clear and stirring was stopped. The photoinitiator was added and the solutions for experiments MP_ETPP and MP_CQ were stirred, until the initiator had fully dissolved. This took 5 min. The solution (MP_None, MP_ETPP and MP_CQ) was put into a greased PMMA-mould on top of the freeze caster, which had an inner diameter of 19 mm. Greasing was done to prevent leaking of the solution. The filling level was not more than 5 mm.

MP_None was freeze-cast with a cooling rate of 2 K/min, starting at room temperature. The solution became increasingly pasty and viscous with sinking temperature. It was difficult to measure an exact melting point for the solution. When the temperature hit -85 °C, measured at the bottom of the sample, the PSZ had become solid.

MP_ETPP was freeze-cast with a cooling rate of 5 K/min, starting at room temperature. Cooling was stopped when the bottom of the sample hit -80 °C. The heating was switched on, as was the 400 nm lamp, with a constant current of 0.25 A. After irradiation for 13 min and reaching -35 °C the sample had polymerised.

MP_CQ was freeze-cast with a cooling rate of 5 K/min, starting at room temperature. Cooling was stopped when the bottom of the sample hit -80 °C. The heating was switched on, as was the 470 nm lamp, with a constant current of 0.25 A. After 13 min, the same time as the sample with ETPP, MP_CQ was way rubberier and not polymerized to the same degree.

3.4.2 Solvent prerequisites

One of the objectives of this Master Thesis was to find a suitable solvent besides camphene for the studied freeze-casting of PSZ/TT. The following list shows the requirements a potential solvent had to fulfil for being worth further investigations and thorough testing:

◦ Sufficient solubility of PSZ, TT & photoinitiators
◦ Melting point between -5 °C – 50 °C
◦ Phase separation with PSZ when freezing
◦ Vapor pressure high enough for sublimation at room temperature
◦ No reactivity of PSZ, TT & photoinitiators with solvent
◦ Potential for yielding parallel columnar structures with freeze-casting
◦ Preferably non-toxic
◦ Not overly expensive

3.4.3 Testing solubility of solvents used for freeze casting

Prior to any freeze casting, the solvents, which were potential candidates for a use in freeze casting experiments, had to be tested in terms of solubility of Polyvinylsilazane (PSZ) and Tetrathiol (TT). The tested solvents were camphene, cyclohexane, cyclooctane, p-xylene, dimethyl carbonate, benzyl benzoate and bornyl acetate.

The first test was performed by mixing PSZ with the solvents with a mass ratio of 1 : 1. Each of the seven solvents was completely miscible with PSZ at room temperature.

The second test was performed by mixing all the solvents except for bornyl acetate and benzyl benzoate with TT with a mass ratio of solvent : TT = 2 : 1. Bornyl acetate and benzyl benzoate were tested with a ratio of 1 : 1. There was no complete solubility observed for cyclohexane, cyclooctane and camphene. p-Xylene, dimethyl carbonate, bornyl acetate and benzyl benzoate on the other hand were completely soluble.

The third test was performed by mixing PSZ, solvent and TT with a ratio of PSZ : solvent : TT = 4 : 4 : 1. Bornyl acetate, p-xylene, dimethyl carbonate and benzyl benzoate yielded homogeneous solutions whereas camphene, cyclohexane and cyclooctane showed no full miscibility.

Judging from the solubility testing cyclohexane and cyclooctane were no suitable candidates for the freeze casting process. Since camphene was used successfully in prior work of the research group, although not showing complete miscibility with TT, it was not yet dismissed as a solvent.

3.4.4 Preliminary testing with p-Xylene (Xyl)

Test 1 (001_02_Xyl): The ansatz in section 3.3 was taken as a baseline. 1.095 g PSZ were degassed, mixed with 0.405 g TT and stirred under a reduced pressure of 6 mbar, until the solution was clear. This took 165 min. 4.5 g p-Xylene was mixed with 0.03 g Camphorquinone (CQ). The two solutions were combined and stirred for 5 min. The clear casting solution was poured into a previously greased PMMA-mould with an inner diameter of 19 mm, that had been put on top of the freeze-casting

platform. The freeze-casting was done with a cooling rate of 2 K/min. The programme looked as follows:
23 °C -> -37 °C in 30 min, hold -37 °C for 30 min, -17 °C for 30 min, -2 °C for 60 min.

After being held for 10 min at -37 °C, the irradiation was started. Curing was done with 25 %, 50 % and 100 % of the maximum power. Each of the three levels was held for 30 min, totalling at 90 min irradiation time.

Test 2 (002_02_Xyl): Everything was kept constant except for a small change in the freeze-casting programme. Instead of cooling to -37 °C, the new threshold was -57 °C. Cooling rate stayed the same with 2 K/min.

Test 3 (003_02_Xyl): The only change between the second and the third attempt was the preparation of the casting solution. After degassing the PSZ, a mix of the TT + p-Xylene + CQ was added to the PSZ, stirred for 1 min and cast directly after.

Test 4 (007_08_Xyl): The procedure was done according to test 1, but with a different freeze casting programme. The cooling rate was changed to 8 K/min instead of 2 K/min. Low temperature threshold was -97 °C, held for 5 min, followed by warming up to -15 °C in 20 min. -15 °C were held till the end of illumination.

Test 5 (008_08_Xyl): Following test 4, 5 mg SiC were added as a nucleating agent to the otherwise ready casting solution and stirred for 1 min.

Test 6 (009_08_Xyl): Following test 5, another nucleating agent was tested: 5 mg of Aerosil 200. The low temperature threshold for the freeze caster was set to -105 °C.

Test 7 (014_08_Xyl): Following test 6, Si_3N_4 (3 mg) were tested as nucleating agent and the low-temperature threshold set to -121 °C.

Test 8 (016_08_Xyl): Following test 7, the SiC was removed from the ansatz and the low-temperature threshold set to -137 °C. The surface plate of the freeze caster was roughened with SiC 2000 grit sandpaper.

Test 9 (017_08_Xyl): Following test 8, 6 mg Aerosil 200 were used as a nucleating agent. Two drops of silicone oil were put onto the casting platform prior, followed by a layer of aluminium foil. The foil was rolled flat with a glass cylinder. The mould was greased and put onto the aluminium foil.

Test 10 (019_08_Xyl): Following test 9, 2 mg of fine UF25 SiC were used as a nucleating agent. This was the first try with the new DC power supply (BK Precision 1550). Irradiation was different with 30 min illumination at 0.3 A constant current, followed by 30 min at 0.6 A constant current.

Test 11 (032_08_Xyl): This was the first try with 48 mg ETPP (Ethyl (2,4,6-trimethylbenzoyl) phenylphosphinate) as a photoinitiator and UHMW-PE (GUR® X143) as a nucleating agent. The casting solution, missing only the ETPP, was put into an ultrasonic bath for 5 min. After addition of ETPP, it was stirred for 2 min, followed by the casting. Cooling rate was 8 K/min, low temperature threshold -140 °C, curing temperature -25 °C. Curing time was 60 min at a current of 0.2 A, using the 470 nm lamp.

Test 12 (033_08_Xyl): Following test 11, PSZ/TT loading was increased to 30 wt%.

Test 13 (034_08_Xyl): Following test 12, PSZ/TT loading was decreased to 20 wt%.

3.4.5 Preliminary testing with dimethyl carbonate (DMC)

Test 1 (004_02_DMC): The ansatz in section 3.3 was taken as a baseline with the same amount of every chemical, just switching the solvent. After degassing the PSZ, a mix of the TT + DMC + CQ was added to the PSZ, stirred for 1 min and cast directly after. The clear casting solution was poured into a previously greased glass-mould with an inner diameter of 18.2 mm, that had been put on top of the freeze-casting platform. The freeze-casting was done with a cooling rate of 2 K/min. The programme looked as follows:
23 °C -> -57 °C in 40 min, hold -57 °C for 20 min, -37 °C for 20 min, -17 °C for 20 min, -7 °C for 80 min.

Irradiation was done with 25 %, 50 % and 100 % of the maximum power, starting 10 min after reaching -57 °C. Each of the three levels was held for 30 min, totalling at 90 min irradiation time. The sample was put into a vacuum desiccator for sublimation.

Test 2 (005_08_DMC): For the second attempt everything was kept constant except for the ramp and low-temperature threshold. The cooling rate was set to 8 K/min and the low-temperature threshold to -97 °C, which would be reached in 15 min. After casting, the sample was left at the atmosphere to get rid of its solvent.

Test 3 (006_08_DMC): The ansatz in section 3.3 was taken as a baseline. PSZ was degassed, mixed with TT and stirred under a reduced pressure of 6 mbar, until the solution was clear. This took 150 min. DMC was mixed with Camphorquinone (CQ). The two solutions were combined and stirred for 2 min. The clear casting solution was poured into a previously greased glass-mould with an inner diameter of 18.2 mm, that had been put on top of the freeze-casting platform. The freeze-casting was done with a cooling rate of 8 K/min. The programme looked as follows:
23 °C -> -105 °C in 16 min, hold -105 °C for 5 min, -12 °C for 120 min.

Test 4 (011_08_DMC): PSZ, TT, DMC & CQ were used in the ansatz in the same amount as before. Low temperature set point during freeze casting was -113 °C, curing temperature -15 °C. 0.1 wt% Si_3N_4 were added to the casting solution to see if a fining of the structure would occur.

Test 5 (018_08_DMC): PSZ, TT, DMC & CQ were used in the ansatz in the same amount as before. Low temperature set point during freeze casting was -137 °C, curing temperature stayed at -15 °C. 0.1 wt% SiC were added to the casting solution to see if a fining of the structure would occur.

Test 6 (024_08_DMC): Following test 5, 0.1 wt% UHMW-PE was used as a nucleating agent. Curing was done with the 470 nm lamp using the new DC power supply at 0.2 A, 0.4 A and 0.8 A for 30 min each.

Test 7 (038_08_DMC): The following parameters changed compared to test 6: 48 mg ETPP were used as a photoinitiator instead of CQ, 0.25 wt% Si_3N_4 were used as a nucleating agent, low temperature setpoint was -140 °C, curing temperature set to -25 °C. The Si_3N_4 was deagglomerated by using an ultrasonic bath for 5 min. Curing time was 1 h at 0.2 A.

Test 8 (040_08_DMC): Following test 7, 0.2 wt% Si_3N_4 were used as a nucleating agent and stirring time of PSZ and TT was set to 75 min.

Test 9 (041_08_DMC): Following test 8, stirring time of PSZ and TT was set to 30 min.

Test 10 (042_08_DMC): Following test 9, PSZ/TT loading was set to 30 wt%.

Test 11 (044_08_DMC): Following test 10, PSZ/TT loading was set to 20 wt%.

3.4.6 Preliminary testing and freeze drying of bornyl acetate (BA)

Test 1 (026_08_BA): The ansatz in section 3.3 was taken as a baseline. 1.102 g PSZ was degassed, mixed with 0.414 g TT and stirred under a reduced pressure of 6 mbar, until the solution was clear (after 105 min). 4.499 g Bornyl acetate were added and the solution stirred for 5 min. 30 mg Camphorquinone were added and the solution stirred for 15 min. Freeze casting was performed with a cooling rate of 8 K/min, starting from room temperature.

Test 2 (027_08_BA): The ansatz in section 3.3 was taken as a baseline. 1.096 g PSZ was degassed, mixed with 0.405 g TT and stirred under a reduced pressure of 6 mbar, until the solution was clear (after 134 min). 4.508 g Bornyl acetate were added and the solution stirred for 5 min. 36 mg ETPP were added and the solution stirred for 2 min. Bornyl acetate itself was used as a nucleating agent by freezing 7 drops onto the casting platform and starting the freeze casting from 10 °C to prevent it from melting. Freeze casting was performed with a cooling rate of 8 K/min. Illumination was done with the 470 nm lamp (0.2 A constant current). It was started during the heating process at -78 °C. -16 °C were held constant during illumination, which lasted for a total of 65 min.

Test 3 (028_08_BA): Because the procedure in the second attempt had worked quite well, it was repeated by adding 0.2 wt% of Si_3N_4 as a nucleating agent. Illumination was done with the 470 nm lamp, 30 min at 0.2 A and 2 min at 0.6 A constant current.

Test 4 (029_08_BA): Because the addition of Si_3N_4 had worked well, 0.2 wt% SiC was used instead this time. Illumination was done with the 470 nm lamp at 0.45 A constant current for 40 min.

Test 5 (030_08_BA): Based on Tests 3 & 4, another different nucleating agent was tested, namely 0.2 wt% Ultrahigh molecular weight polyethylene (UHMW-PE, GUR® X143).

Test 6 (035_08_BA): It was tested, if a higher Si_3N_4 content than in Test 4 would lead to an even finer structure. 0.5 wt% Si_3N_4 were used, and the illumination prolonged to 60 min time at 0.25 A constant current.

Test 7 (036_08_BA): Following Test 6, the Si_3N_4 content was reduced to 0.4 %.

Test 8 (045_08_BA): Following Test 7, the Si_3N_4 content was reduced further to 0.3 %.

Test 9 (046_08_BA): Following Test 8, the Si_3N_4 content was reduced further to 0.25 %.

Test 10 (047_08_BA): Following Test 9, The Si_3N_4 content was kept at 0.25 %, but the illumination time during photopolymerization was reduced to 40 min.

Freeze drying of bornyl acetate

Bornyl acetate presented a problem the other solvents did not. Sublimation in the vacuum desiccator was very difficult because the bornyl acetate diffused into the grease locking the desiccator. This caused leaking after just a few hours of operation. To put new grease on the contact between upper and lower part of the desiccator, it had to be opened. This turned out to be fatal for the samples. After being subjected to atmospheric pressure before the solvent had been removed completely, the samples started cracking as soon as the vacuum was turned back on.

A freeze dryer (Christ Alpha 1-4 LDplus) was used for the removal of the bornyl acetate from the samples. The first sample was put into the freeze dryer at 0.1 mbar pressure. The sample tore in half, which is why the next sample was put into the freeze dryer at 0.5 mbar. The same thing happened as before with a rupture through the sample. The pressure may have been to low which is why the next sample was put in at 2 mbar. This time, pressure was too high, because the bornyl acetate did not crystallize on the cooled rods it was supposed to, but at several other locations in the freeze dryer. A lowering of the pressure to 1.5 mbar for the next sample had a similar effect. Figure 16 shows some of the samples, that were destroyed in the freeze dryer.
Finally, a pressure of 1.0 mbar was chosen and tested, showing promising results. Only very fine cracks were visible. PTFE-foil was wrapped around the samples, secured with rubber bands. During sublimation, they contracted together with the samples. Only top and bottom were now open to the surrounding vacuum, leading bornyl acetate to only sublimate there. Crack-free samples with a loading of PSZ/TT up to 30 % could be obtained using this method. With loadings as high as 35 & 40 %, only the samples with no Si_3N_4 could be obtained crack-free.

Figure 16: Samples destroyed during freeze drying, showing large cracks

3.4.7 Influence of tetrathiol (TT) concentration on polymerization behaviour

A mass ratio of PSZ : TT = 2.7 : 1 was used as standard ratio in most of the experiments. This ratio amounts to equal concentrations of vinyl groups and thiol groups in the solution and proved to work efficiently in terms of polymerisation.
The tetrathiol molecule contains oxygen, which leads to oxygen being present in the final ceramic. The presence of oxygen is not desirable because it alters the properties of the ceramic. Thus, oxygen content should be minimized as much as possible. Tests were performed to determine the least amount of tetrathiol necessary to produce a stable polymer structure after polymerisation. Starting from the initial mass ratio of 2.7 : 1 the amount of tetrathiol present in the mixture was continuously reduced.

Testing was done for two different lamps, one with a wavelength of 470 nm, the other with 400 nm. The pre-treatment of the testing solutions was the same as if they would have been freeze-cast. The degassed PSZ was mixed with TT at 6 mbar for 30 min. Bornyl acetate and Si_3N_4 were added. The mix was put in an ultrasonic bath for 5 min. After stirring for 2 min, 48 mg of ETPP were added for testing with the 470 nm lamp and 36 mg of ETPP for testing with the 400 nm lamp. The mixture was stirred for another 2 min. The loading of the monomer solution (PSZ + TT) always added up to 25 wt% and the solution was polymerised in the vials directly. The LED-lamp was run at a constant current of 0.20 A, which produced a voltage of 26 V (470 nm lamp) and a voltage of 18 V (400 nm lamp), respectively. The irradiation ended after 10 min.

3.5 First measurement series with all four solvents

After the preliminary testing, a first measurement series was performed with all four solvents and both photoinitiators. The ansatz consisted of 1.095 g PSZ, 0.405 g TT, 4.5 g solvent, 30 mg camphorquinone (CQ) / 36 mg ETPP and, if added, 15 mg Si_3N_4. shows a quick overview over the series, marking which combinations failed / succeeded.

Table 7: First measurement series with all four solvents; NO: the experiment failed, YES: the experiment succeeded, and a sample was attained, that could be thermally post-cured and pyrolyzed for further characterization

Photoinitiator	Nucleating agent	Bornyl acetate	Dimethyl carbonate	Camphene	p-Xylene
ETPP	Si_3N_4	NO	NO	NO	YES
ETPP	-	YES	YES	YES	YES
Camphorquinone	Si_3N_4	NO	NO	NO	YES
Camphorquinone	-	YES	NO	NO	YES

Preparation of the casting solution

PSZ was degassed, followed by mixing it with TT and stirring under a reduced pressure of 6 mbar for 30 min.

p-Xylene, Dimethyl carbonate, Bornyl acetate: The solvent was added, followed by Si_3N_4, if part of the experiment. After rotating the sample 10 times for a rough mixing, it was put into an ultrasonic bath for 5 min. The solution was stirred for 2 min, followed by the addition of ETPP / camphorquinone. From now on protection from ambient light was necessary. The solution was stirred for another 2 min. After this step, it was ready for freeze casting.

Camphene: Camphene and ETPP / camphorquinone were put together at 55 °C and rotated 10 times for a rough mixing. Then they were stirred at 55 °C for 5 min. If Si_3N_4 was part of the experiment, the Si_3N_4 was added prior to the photoinitiator and the camphene/Si_3N_4 mixture put into an ultrasonic bath for 5 min. The resulting solution was then added to the PSZ/TT solution and stirred for another 2 min at 55 °C. After this step, it was ready for freeze casting.

Freeze casting

A cylindrical PMMA mould (p-xylene / bornyl acetate / camphene) or a cylindrical glass mould (dimethyl carbonate) were prepared by greasing the bottom, and putting in a plastic display foil for easier demoulding after the curing. The mould had an inner diameter of 19 mm and a height of 30 mm. It was covered with a hood in the next step to prevent illumination from ambient light with a wavelength shorter than 500 nm during the casting. Camphene casting started at 55 °C because of its higher melting point. For bornyl acetate only, the temperature was set to 10 °C and 7 drops of the solvent were added into the mould to cover the bottom. A small bornyl acetate crystal, stored in the fridge at 4 °C, was added to get a thin layer of frozen bornyl acetate as nucleating agent. The casting solution was poured into the mould.

In the next step, the freeze casting was done with a ramp of 8 K/min. The temperature programmes in detail run as follows (Table 8):

Table 8: Temperature programmes for the freeze casting process

p-Xylene / Dimethyl carbonate	Camphene	Bornyl acetate
23 °C -> -145 °C in 21 min	55 °C -> -105 °C in 20 min	10 °C -> -142 °C in 19 min
-145 °C hold for 2 min	-105 °C hold for 2 min	-142 °C hold for 2 min
-145 °C -> -30 °C in 10 min	-105 °C -> -30 °C in 10 min	-142 °C -> -30 °C in 10 min
-30 °C hold till end of irradiation	-30 °C hold till end of irradiation	-30 °C hold till end of irradiation

Freezing front velocity

Freezing front velocity was determined by taking photos every 30 s during casting of the p-xylene, dimethyl carbonate and bornyl acetate samples, when they had no nucleating agent added. Camphene had already been measured in previous work of the research group [4]. The velocity could be calculated by graphical evaluation of the growth of the freezing front.

Photopolymerization

After reaching the low temperature threshold and a waiting time of 2 min, the heating was turned on and stopped again after reaching -45 °C. The heating of the last 15 °C to reach -30 °C was done slowly by letting the ambient air warm the freeze caster. The light protection hood was removed, and the 400 nm (with ETPP) / 470 nm (with CQ) LED lamp attached. After a waiting time of 5 min at -30 °C, the illumination started with a constant current of 0.2 A, provided by a DC power supply (BK Precision 1550), leading to a voltage around 19 V for the 400 nm lamp and 26 V for the 470 nm lamp. The illumination stopped after 5 min for the 400 nm lamp and after 60 min for the 470 nm lamp, leaving the sample ready for demoulding and sublimation.

Sublimation

The photocured sample was extracted from the mould and the plastic display foil removed by carefully barking it from the sample. The top and bottom parts were cut off with a sharp knife to get an evenly shaped sample. It was then placed onto a speaker grille which had been mounted onto a plastic jar. The speaker grille enabled ventilation from the bottom as well, since it was very permeable.

p-Xylene, Dimethyl carbonate, Camphene: The just mentioned build-up was put inside a vacuum desiccator. A rotary vane pump was connected, and the sublimation started. After 24 h the process was stopped and the sample ready for thermal post-curing.

Bornyl acetate: Bornyl acetate was treated differently because it dissolved into the grease, which sealed the vacuum desiccator. This led to leakage after a few hours. Thus, it had to be sublimated in a freeze dryer (Christ Alpha 1-4 LDplus) at 1.0 mbar for 48 h. To prevent cracking during sublimation, the

sample needed to be surrounded by a sheet of PTFE-foil on its side. The foil was secured with a rubber band, which contracted together with the sample during the sublimation.

Final curing & pyrolysis was done following the procedure in section 3.3.

Samples fabricated using this method, which will be presented in results and discussion later: 071_Cam_25, 075_Xyl_25, 076_Xyl_25, 078_DMC_25, 082_DMC_25, 084_BA_25, 086_BA_25

3.6 Final method for the photopolymerization-assisted solidification templating

After all the preliminary testing and switching from 470 nm to 400 nm LEDs and from camphorquinone to ETPP, the following section describes the method, which was used in the end. The samples for the compressive strength determination, SEM micrographs, permeability as well as mercury intrusion measurements were also produced this way. A flow chart of the final process is presented in Figure 17.

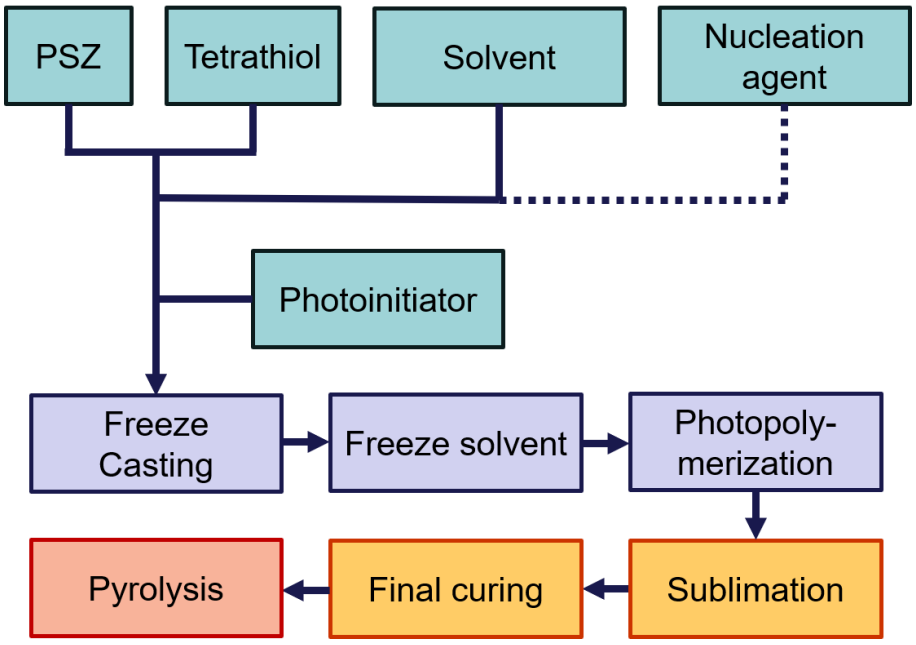

Figure 17: Flowchart of the final method for the photopolymerization-assisted solidification templating

The chemicals needed for one experiment are listed in the ansatz below (Table 9). The mass ratio of PSZ : TT = 2.7 : 1. The loading of PSZ + TT mounts to 25 wt% of the whole solution.

Table 9: Ansatz for the final method

Ansatz	
1.095 g	PSZ
0.405 g	TT
4.5 g	Solvent (p-Xylene/dimethyl carbonate/camphene/bornyl acetate)
0.048 g	ETPP
0.006 - 0.012 mg	Si_3N_4 (none for camphene)

Preparation of the casting solution

At first, PSZ is degassed under stirring and with a reduced pressure of about 6 mbar until gas bubble formation stops. This usually takes between 20 – 40 min. The TT is added, leading to the solution becoming cloudy, and stirred for 40 min under the same reduced pressure as before.

p-Xylene, Dimethyl carbonate, Bornyl acetate: The solvent is added, followed by Si_3N_4. After rotating the sample 10 times for a rough mixing, it is put into an ultrasonic bath for 5 min. The solution is stirred for 2 min, followed by the addition of ETPP. From now on protection from ambient light is necessary. The solution is stirred for another 2 min. After this step, it is ready for freeze casting.

Camphene: Camphene and ETPP are mixed and stirred at 55 °C for 2 min. The Camphene/ETPP solution is then added to the PSZ/TT solution and stirred for another 5 min. After this step, it is ready for freeze casting.

Freeze casting

A cylindrical PMMA mould (p-xylene / bornyl acetate / camphene) or a cylindrical glass mould (dimethyl carbonate) is prepared by greasing it, especially at the bottom, and putting in a plastic display foil for easier demoulding after the curing. The mould has an inner diameter of 19 mm and a height of 30 mm. It is covered with a hood in the next step to prevent illumination from ambient light with a wavelength shorter than 500 nm during the casting. Camphene casting starts with 55 °C because of its higher melting point. For bornyl acetate only, the temperature is set to 10 °C and 7 drops of the solvent are added into the mould to cover the bottom. A small bornyl acetate crystal, stored in the fridge at 4 °C, is added to get a thin layer of frozen bornyl acetate as nucleation agent. The casting solution is poured into the mould.

In the next step, the freeze casting is done with a ramp of 8 K/min. The temperature programme in detail runs as follows (Table 10):

Table 10: Temperature programmes for the freeze casting process

p-Xylene / Dimethyl carbonate	Camphene	Bornyl acetate
23 °C -> -145 °C in 21 min	55 °C -> -105 °C in 20 min	10 °C -> -142 °C in 19 min
-145 °C hold for 2 min	-105 °C hold for 2 min	-142 °C hold for 2 min
-145 °C -> -25 °C in 10 min	-105 °C -> -25 °C in 10 min	-142 °C -> -25 °C in 10 min
-25 °C hold till end of irradiation	-25 °C hold till end of irradiation	-25 °C hold till end of irradiation

Photopolymerization

After reaching the low temperature threshold and a waiting time of 2 min, the heating is turned on and stopped again after reaching -40 °C. The heating of the last 15 °C to reach -25 °C is done slowly by letting the ambient air warm the freeze caster. The light protection hood is removed, and the 400 nm LED lamp attached. After a waiting time of 5 min at -25 °C, the illumination starts with a constant current of 0.2 A, provided by a DC power supply (BK Precision 1550), leading to a voltage between 18.6 – 18.9 V. The illumination stops after 15 min, leaving the sample ready for demoulding and sublimation.

Sublimation

The photocured sample is extracted from the mould and the plastic display foil removed by carefully barking it from the sample. The top and bottom parts are cut off with a sharp knife to get an evenly shaped sample. It is then placed onto a textile fabric which has been mounted onto a plastic jar. The textile fabric enables ventilation from the bottom as well, since it is very permeable.

p-Xylene, Dimethyl carbonate, Camphene: The just mentioned build-up is put inside a vacuum desiccator. A rotary vane pump is connected, and the sublimation started. After 24 h the process is stopped and the sample ready for thermal post-curing.

Bornyl acetate: Bornyl acetate is treated differently because it dissolves into the grease, which seals the vacuum desiccator. This leads to leakage after a few hours. It must therefore be sublimated in a freeze dryer (Christ Alpha 1-4 LDplus) at 1.0 mbar for 48 h. To prevent cracking during sublimation, the sample needs to be surrounded by a sheet of PTFE-foil on its side. The foil is secured with a rubber band, which contracts together with the sample during the sublimation.

Thermal post-curing & Pyrolysis

The thermal post-curing is done by placing the sample into an oven equipped with an inert gas retort (wtc binder No. 940402). A constant flow of nitrogen with 0.3 l/min is applied. The heating rate is set at a constant 1 K/min, starting at room temperature and stopping at 200 °C. The 200 °C are held for 4 h. The oven is switched off afterwards and the sample unloaded once room temperature has been reached again.

Pyrolysis is done in a tube furnace with a constant flow of 0.3 l/min N_2. The heating rate is set at a constant 1 K/min, starting at room temperature and stopping at 1000 °C. The 1000 °C are held for 2 h, followed by cooling to room temperature with a cooling rate of 2 K/min. The pyrolyzed samples are always black in colour.

Sample numbers

Samples fabricated using this method, which will be presented in results & discussion later (Table 11):

Table 11: Samples fabricated using the method described in section 3.6

093_BA_30	099_BA_25	105_BA_20	111_Xyl_25	119_Xyl_25
094_BA_30	100_BA_25	106_BA_20	113_DMC_25	123_Cam_25
095_BA_35	101_BA_25	107_BA_15	114_DMC_25	124_Cam_25
096_BA_35	102_BA_25	108_BA_15	116_DMC_25	125_Cam_25
097_BA_40	103_BA_25	109_DMC_25	117_Xyl_25	126_Cam_25
098_BA_40	104_BA_25	110_BA_25	118_Xyl_25	

3.7 Variation of PSZ/TT loading and Si_3N_4 content with bornyl acetate as a solvent

Samples with different PSZ/TT loading and Si_3N_4 content were prepared using bornyl acetate as a solvent. The goal was to study occurring changes in microstructure, apparent porosity and bulk density. The following Table 12 shows the masses of the reactants used for the castings. For each sample, 0.048 g ETPP were used for curing. Preparation of the samples was done after the final method for the photopolymerization-assisted solidification templating, described in section 3.6.

Table 12: Masses of the reactants used for the castings; colour intensifies with PSZ/TT loading

Sample name	PSZ/TT loading (%)	PSZ (g)	TT (g)	Bornyl acetate (g)	Si_3N_4 (g)
107_BA_15	15	0.658	0.244	5.110	0.012
108_BA_15	15	0.653	0.239	5.103	
105_BA_20	20	0.876	0.328	4.811	0.012
106_BA_20	20	0.879	0.325	4.811	
102_BA_25	25	1.096	0.406	4.504	0.012
084_BA_25	25	1.096	0.400	4.499	
093_BA_30	30	1.318	0.488	4.200	0.012
094_BA_30	30	1.312	0.486	4.208	
095_BA_35	35	1.533	0.572	3.902	0.012
096_BA_35	35	1.523	0.571	3.904	
097_BA_40	40	1.753	0.652	3.600	0.012
098_BA_40	40	1.749	0.649	3.606	

3.8 Characterization

3.8.1 Mass loss

The mass of the samples was measured three times. The first measurement took place after sublimation of the solvent from the cured sample, the second one after thermal post-curing, and the third one after pyrolysis. Based on these values, different losses of mass can be calculated. The formula used is listed in equation (12):

$$\text{Loss of mass } = \left(1 - \frac{m_e}{m_0}\right) \cdot 100\ \% \tag{12}$$

m_0 is the mass at the beginning and m_e the mass at the end of the treatment.

3.8.2 Linear shrinkage

The linear shrinkage was determined by measuring diameter and height of the samples after curing, after thermal post-curing as well as after pyrolysis. The formula used for calculations was equation (13):

$$\text{Linear shrinkage } = \left(1 - \frac{x_e}{x_0}\right) \cdot 100\ \% \tag{13}$$

x_0 is the length (diameter or height) at the beginning and x_e the length (diameter or height) at the end of the treatment.

3.8.3 Density and porosity, measured by the immersion test method

The immersion test method (after European standard EN 623-2 [84]) was used to determine the values for bulk density, apparent solid density, and apparent porosity of the samples. For each sample, three different masses had to be recorded to be able to calculate the values.

The first measurement was the mass of the dry sample. The sample was dried in a drying oven at 110 °C until constant mass had been reached. To test for constant mass, the supposedly dry sample was weighed, put in the oven, and weighed again after 2 h. When the mass had not changed for more than 0.03 %, the sample was considered dry.

The next step was to put the dry and cool sample into an air tight vacuum chamber. After closing the vessel, it was evacuated to a pressure of < 2500 Pa. The low pressure was kept up for at least 15 min. The connection to the vacuum pump was shut and the immersion medium, being distilled water, was added slowly. The liquid level had to reach a point 20 mm higher than the sample height after 3 min. This was to ensure complete submersion. The connection to the vacuum pump was reopened and the low pressure was upheld for another 30 min. The pump was switched off, the vacuum chamber aerated, and the sample kept submerged for 30 min.

The second measurement was the apparent mass of the submerged sample. The analytical balance (Sartorius A 120 S) was equipped with a bridge, where a beaker with the immersion medium could

stand on. The sample was put into a small basket hanging from a thin wire, which was attached to an arc. The arc was connected to the balance. Sample mass as well as water temperature were recorded.

The third measurement was the mass of the sample, saturated with water. The sample was taken out of the water, quickly wiped with a wet, lint-free cloth, and weighed immediately. Sucking liquid out of the pores was avoided as good as possible. Immersion, drying and weighing were repeated to check for measurement uncertainties. The *bulk density* ρ_b is the ratio of the dry mass of a porous body to its bulk volume. It was calculated by the following equation (14):

$$\rho_b = \frac{m_1}{m_3 - m_2} \cdot \rho_L \tag{14}$$

m_1 is the mass of the dry sample, m_2 the apparent mass of the submerged sample, m_3 the mass of the sample, saturated with water, and ρ_L the density of distilled water at the measured temperature. The *apparent solid density* ρ_s is the ratio of the dry mass of the material to its apparent solid volume. It was calculated by using equation (15):

$$\rho_s = \frac{m_1}{m_1 - m_2} \cdot \rho_L \tag{15}$$

The *apparent porosity* Π_a is the ratio of the total volume of the open porosity of a porous body to its bulk volume. It was calculated by the following equation (16):

$$\Pi_a = \frac{m_3 - m_1}{m_3 - m_2} \cdot 100 \tag{16}$$

3.8.4 Permeability

Gas permeability measurements were performed using filtered compressed air as the permeating fluid. Thickness and diameter of the samples had to be determined for future calculations. The samples were put into shrinking tubes. On each end of the shrinking tubes, flexible tubes were placed. A small burner was used to heat the shrinking tube and cause it to cling to the samples and flexible tubes. Parts of a silicone tubing were put around the location of the sample in the shrinking tube, and around the places, were the shrinking tube ended. Screw clamps fixed the whole setup to prevent it from leaking upon pressure build-up. A soapy solution was used to test for leaks during pressure application. The setup can be seen in Figure 18.

Pressure was regulated via a differential pressure gauge. Manometers were located upstream as well as downstream of the sample. Air flow was detected two ways depending on flow rate. Very small flows (< 1 – 3 l/min) resulting from dense samples were detected via a bubble flowmeter. The time it took for a soap film to travel a definite volume in a glass tube was recorded. The stationary gas flow Q was then calculated by dividing the volume by the passed time. For larger flows (1 – 50 l/min), an electronic flowmeter (Digital Flow Switch PFM7, SMC) was used, which calculated the stationary gas flow by itself and showed it live on a display.

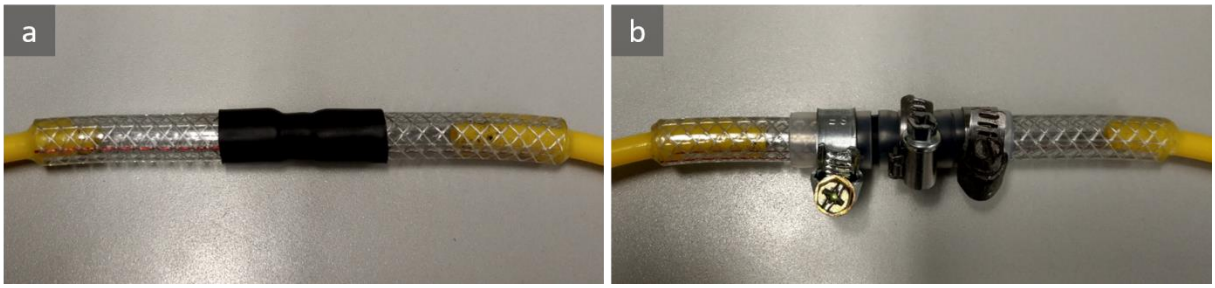

Figure 18: Setup for the permeability measurements: (a) shrinking tube surrounding the sample, (b) shrinking tube fixed with screw clamps and silicon bands to prevent leaking upon pressure build-up

Various differential pressures were applied, starting from 0.2 bar to maximal 2.0 bar, depending on the sample. If the flow was higher than 50 l/min (limit for the flow meter), the pressure was not increased further, and the measurement stopped.
The area-specific *permeating flow* v_p was calculated by the following equation (17):

$$v_p = \frac{Q}{A} \tag{17}$$

Q is the stationary gas flow, A the radial cross-section of the sample. Forchheimer´s equation (18) for compressible fluids was used to determine permeability coefficients (Darcian, k_1, and Non-Darcian, k_2), employing a quadratic fit to $(p_i^2-p_0^2)/(2p_0 \cdot l)$ using the least-squares method [85].

$$\frac{p_i^2 - p_0^2}{2p_0 \cdot l} = \frac{\eta}{k_1}\frac{Q}{A} + \frac{\rho}{k_2}(\frac{Q}{A})^2 \tag{18}$$

Q is the stationary gas flow through the sample, p_i the upstream differential pressure, p_0 the downstream differential pressure, and l the thickness of the sample. An air viscosity η of $1.84 \cdot 10^{-5}$ Pa·s and an air density ρ of 1.15 kg·m^{-3} are assumed.

3.8.5 Compressive strength

The samples, fabricated after the final method (section 3.6), were ground to get a plane parallel top and bottom. Difficulties arose during grinding, when smaller chunks of the samples broke off. Very careful grinding by hand was performed to avoid damage, that would negatively influence the outcome of the measurements. Compressive strength was measured on the Zwick 1474 using a forward speed of 0.5 mm/min. After a displacement of 2 mm, corresponding to a passed time of 4 min, the measurement was stopped.

The *compressive strength σ* was calculated by the following formula:

$$\sigma = \frac{F \cdot 4}{d^2 \cdot \pi} \tag{19}$$

F is the maximal force recorded during the measurement and d the diameter of the sample. The Zwick compression testing machine is pictured in Figure 19. On each side of the testing cylinders (top and bottom), PTFE-foil was attached to compensate for slight deviations from plane parallelism. Three samples were measured for dimethyl carbonate and p-xylene, four for camphene, and five for bornyl acetate.

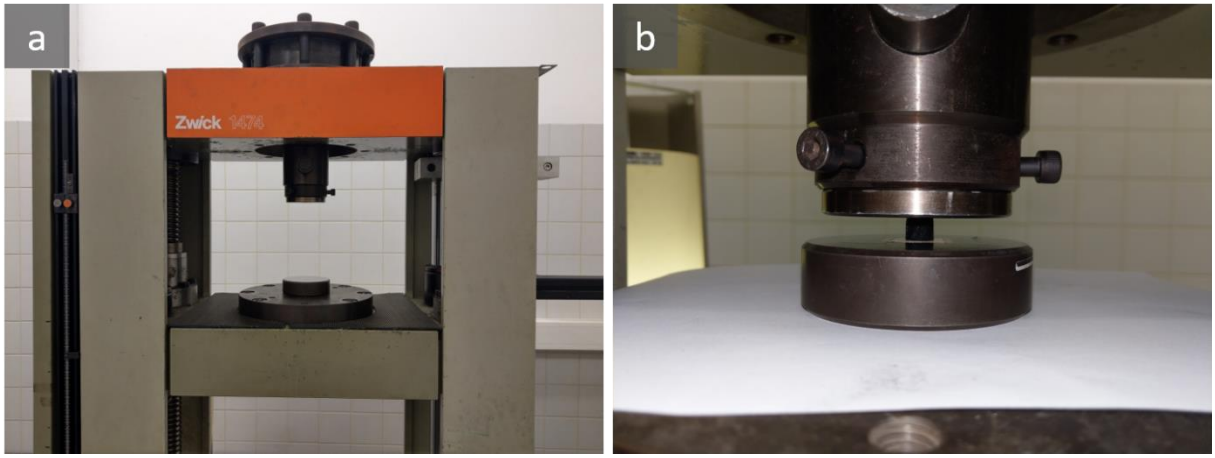

Figure 19: (a) Zwick 1474 compression testing machine; (b) clamped sample, ready for testing

3.8.6 Microstructural analysis by SEM and mercury intrusion porosimetry

3.8.6.1 Scanning electron microscopy

Transversal cuts (perpendicular to the freezing direction) and longitudinal cuts (parallel to the freezing direction) of the samples were prepared. The cut pieces were stuck onto a graphite strap with the planes of interest looking upwards and arranged parallel to the surface of the sample holder. A scanning electron microscope (FEI Quanta 200) was used in low-vacuum mode to record micrographs of the surfaces in several different magnifications (from 50x to 1000x).

3.8.6.2 Mercury intrusion porosimetry

Samples with a pore volume of 250 – 350 mm³, calculated from the values obtained by the immersion test method, were measured in a mercury intrusion porosimeter (Thermo Scientific Pascal 140/440). Measurements were performed with a standard method up to a pressure of 400 MPa.

The Hg-Porosimetry was performed for the following samples:

◦ 071_Cam_25, 109_DMC_25, 110_BA_25, 111_Xyl_25 for comparison of solvent influence
◦ 084_BA_25, 107_BA_15, 102_BA_25, 095_BA_35 for comparison of loading influence

3.8.7 Differential Photocalorimetry measurements

3.8.7.1 Sample preparation

Polyvinylsilazane (PSZ) was degassed and weighed in. The degassing was done by stirring the PSZ under a reduced pressure of approximately 6 mbar. It was stopped after the formation of gas bubbles had stopped. This took at least 20 min. The pentaerythritol tetrakis(3-mercaptopropionate), also known as tetrathiol (TT), was added and the solution was stirred under the same reduced pressure for another 30 min. The solvent was added and, for Dimethyl carbonate, p-Xylene and Bornyl acetate, directly after that, the Si_3N_4. When camphene was used as a solvent, it was heated to 55 °C prior to adding it to the solution. This step is necessary as camphene is a solid at room temperature.

After addition of solvent and Si_3N_4 the samples were put in an ultrasonic bath for 5 min to further degas the solution and deagglomerate the Si_3N_4. In the next step the solution was stirred for 2 min, followed by the addition of the photoinitiator ETPP. The solution was stirred for another 2 min under protection from ambient light. Measurement could now be started, as the preparation was finished. The weighed-in amounts of the chemicals can be found in Table 13. The PSZ/TT mass ratio was always kept constant at 2.7. With this ratio the number of vinyl groups equals the number of thiol groups. The PSZ/TT loading was kept at 25 % for every measurement to ensure better comparability. PSZ/TT loading is the mass of PSZ/TT divided by the mass of the whole reaction solution.

Table 13: Preparation of solutions for DPC-measurements. PSZ/TT loading is the mass ratio of PSZ/TT divided by the whole reaction solution

		Camphene	Dimethyl carbonate	p-Xylene	Bornyl acetate
Reaction solution	PSZ	1.097 g	1.098 g	1.094 g	1.094 g
	TT	0.400 g	0.402 g	0.406 g	0.402 g
	Solvent	4.500 g	4.496 g	4.495 g	4.511 g
	Si3N4	-	15 mg	15 mg	15 mg
	ETPP	36 mg	36 mg	36 mg	36 mg
PSZ/TT mass ratio		2.7	2.7	2.7	2.7
PSZ/TT loading (%)		25	25	25	25

3.8.7.2 Measurements

The DPC measurements were performed on a Netzsch DSC 204 F1. A picture of the used device can be found in Figure 20. The difference to conventional DSC devices is the possibility to illuminate the sample with an LED. The used LED lamp emitted a wavelength of 400 nm. The irradiation power was about 10 mW/cm^2.

In the first step, the prepared solutions were weighed into aluminium crucibles. The weighed amount had to be 8 – 12 mg. As the vapor pressure of dimethyl carbonate and p-xylene is too high to leave the crucibles open during the measurement and aluminium lids are not transparent, glass lids were put on top of the crucibles after balancing. The samples were cooled to -10 °C with a ramp of 2 K/min, taking 15 min. After reaching -10°C the temperature was kept constant for 4 min. Two irradiation steps with

an irradiation time of 5 min each followed. The second irradiation was always performed to ensure that the curing process had finished. If not, a deflection of the base line would be witnessed. After an additional 2 min of keeping the temperature constant the measurement was finished.

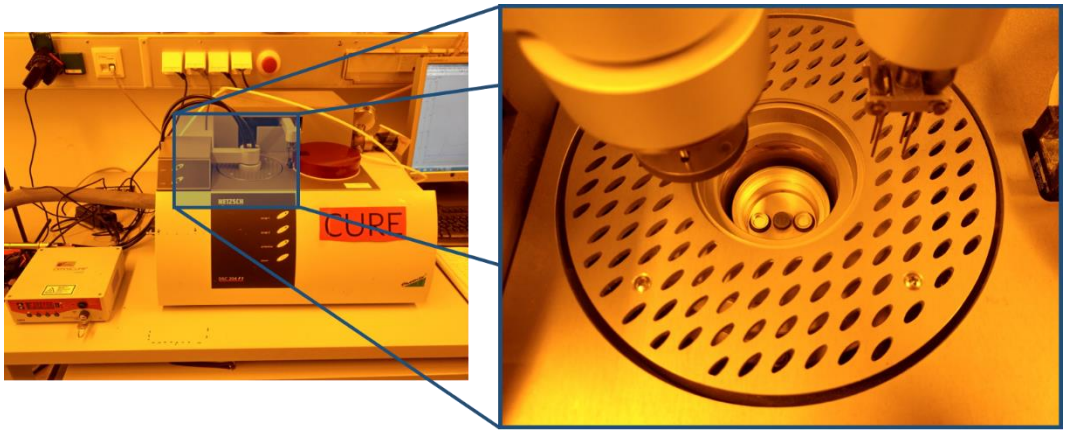

Figure 20: Netzsch DSC 204 F1. The zoom at the right shows the open measuring cell with crucibles at sample & reference position. The right arm with four needles belongs to the autosampler. The left arm is about to shut the vent.

3.8.8 Measurements of enthalpy of fusion & melting point of the solvents

The measurements of melting point and enthalpy of fusion were performed on a Mettler Toledo DSC823^{e} differential scanning calorimeter for the substances camphene, p-xylene, dimethyl carbonate and bornyl acetate. The samples were weighed with a precise mass between 2 – 10 mg and put into an aluminium crucible. After record of the mass, the crucible was sealed with a lid to prevent sublimation and evaporation. This was necessary, because the used substances have quite high vapor pressures. Leaving the crucibles open would result in a mass change and false results, as they depend on the mass. An empty aluminium crucible was crimped with a lid of the same type and used as a reference.

The reference crucible was put on its pedestal in the measuring cell. The crucible containing the sample was placed into the auto sampler. After reaching room temperature the crucible containing the sample was moved on its pedestal in the measuring cell followed by closing of the vent. Purging gas for the measuring cell was nitrogen gas of high purity (99.999 %). The measurement was now ready to start.

Two different ramps were used for the measurements. Both ramps started at the low temperature set point with a heating rate of 2 K/min until the high temperature set point was reached. The first ramp ranged from -16 °C to 125 °C and was used for all four solvents (camphene, dimethyl carbonate, p-xylene, bornyl acetate). Bornyl acetate showed significant supercooling and it was not possible to solidify the solvent at -16 °C.

To ensure, that the DSC measurement started with a frozen bornyl acetate, the temperature range was changed, and a second ramp used. The second ramp ranged from -80 °C to 80 °C. As the other three solvents could be properly measured with the first ramp, only the bornyl acetate measurement was repeated.

4 Results

4.1 Morphology of the samples

The morphology of bornyl acetate samples can be seen in Figure 21. They have been taken as an example to show the transformation process each sample undergoes. The sample is elastic, soft to touch, and white after curing and sublimation. Thermal post-curing causes a slight shrinkage and yellowing of the sample. It loses almost all its elasticity. Pyrolysis leads to a significant linear shrinkage, mass loss, hardening and blackening of the sample. The morphology of samples fabricated with different structuring agents can also be seen in Figure 24 and Figure 28 in section 4.5.

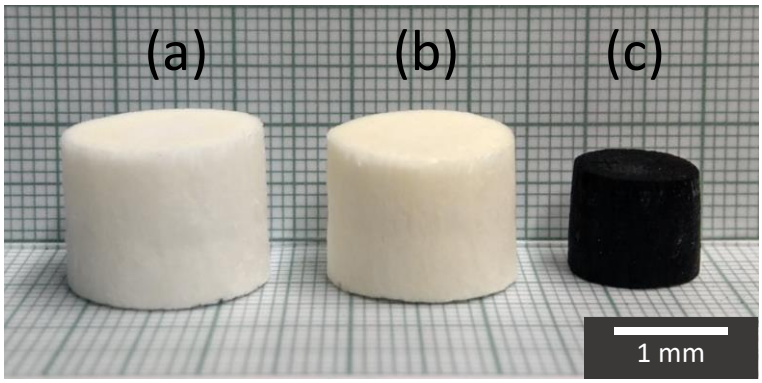

Figure 21: Morphology of a bornyl acetate sample (a) after curing and sublimation of the solvent, (b) after thermal post-curing, (c) after pyrolysis

4.2 Preliminary experiments

p-Xylene

The freezing of the first sample (001_02_Xyl) started at about -5 °C, which is way below the nominal melting point for the used p-Xylene (13.5 °C). Because the solution was supercooled, the bottom 5 mm froze almost instantly. The freezing front grew stable from that point on, with some small gas bubbles forming from time to time and rising to the surface. After being held for 10 min at -37 °C, at the start of the curing, the top of the sample still seemed moist. It was unclear if the PSZ or the p-Xylene were causing this. The finished sample had a very coarse and uneven surface. For the second sample (002_02_Xyl), the new low-temperature threshold of -57 °C didn´t get it to solidify completely. Between the crystals as thick as 1 mm on a very uneven surface, small moist nests were visible. The pure p-Xylene should have been frozen at this point, which leaves the PSZ/TT mixture to be the liquid between the solvent crystals.

With the third test (003_02_Xyl) the aim was to look for differences in crystallization behaviour by leaving out the step of long stirring time of PSZ + TT under reduced pressure. Supercooling happened, as it did in the attempts before, and the crystals seemed to be equally large. Bubble formation had increased a bit. In test four (007_08_Xyl) a higher cooling rate of 8 K/min instead of 2 K/min was applied. The freezing temperature moved to -9 °C with the bottom 4 mm freezing almost instantly. The structure seemed finer with the higher cooling rate, which is why all the following experiments were

done with 8 K/min. In test 5 (008_08_Xyl) the addition of SiC as a nucleating agent did not have a visible effect and the top 2 mm of the sample did not freeze. The higher cooling rate made a lower low-temperature threshold necessary to give the solution enough time to freeze to the top. Therefore -105 °C was the new set temperature for test 6 (009_08_Xyl). Aerosil 200 was added as a nucleating agent, but it seemed as if it was forming gel-like coagulates in the solution. The growing crystals were as coarse as ever before and the freezing front did not get to the top of the sample with this try.

In the following test 7 (014_08_Xyl), the addition of Si_3N_4 did not show visible results in terms of preventing supercooling or fining the structure by providing nucleation seeds. The set minimal temperature of -121 °C for this try was almost enough, because the surface still seemed slightly wet. Setting the minimal temperature to -137 °C was enough to freeze the whole sample in test 8 (016_08_Xyl). Grinding the casting plate on top of the freeze caster with SiC 2000 sandpaper to prevent supercooling by providing a rougher surface had no visible effect. 2 mm of the sample froze almost instantly after having been supercooled. Removing the sample undamaged from the freeze caster after freezing and curing had proven to be quite difficult. The insertion of an aluminium layer between sample and caster, which was done first with test 9 (017_08_Xyl), was very effective and therefore used for every sample afterwards. This statement is valid for samples cast with any solvent and a sample number higher than 017.

Test 10 (019_08_Xyl) was using a finer SiC (UF25) as a nucleating agent. While the addition of SiC seemed to have no effect except for darkening the sample and therefore making it more difficult to cure to the core of the sample, the use of a new power supply, introduced with this test, made curing more reproducible. This is because a constant current could be precisely predefined instead of regulating the current manually, as was done before with a slide control. The introduction of a new photoinitiator, ETPP, with test 11 (032_08_Xyl) and UHMW-PE as a nucleating agent worked quite well. Although the UHMW-PE did not seem to act efficiently as a nucleating agent, ETPP could successfully cure the PSZ/TT mixture with p-Xylene as a solvent. The following tests 12 &13 (033_08_Xyl & 034_08_Xyl) showed that a sample can be successfully fabricated with 30 wt% or 20 wt% PSZ/TT loading as well.

Dimethyl carbonate

When the low-temperature setpoint (-57 °C) during freeze casting was reached in the first test (004_02_DMC), the surface of the sample was still wet. When the suction started during sublimation, and the pressure dropped, the sample was bloating and boiling vigorously. This led to a complete destruction of the sample. The lower temperature setpoint for the second test (005_08_DMC) of -97 °C was necessary, not only because the low-temperature threshold in the first test was too high, but also because the cooling rate had been increased to 8 K/min. After curing, the sample was left at the atmosphere for evaporation of the solvent. This caused the complete destruction of the sample. The third test (006_08_DMC) with a low temperature set point of -105 °C resulted in a very deformed, whitish sample after sublimation.

The Si_3N_4, added as a nucleating agent in test 4 (011_08_DMC), was supposed to lead to fining of the structure. No visible difference could be seen after sublimation of the solvent. During photopolymerization, some liquification on top of the sample, presumably due to the heat input of the lamp, was witnessed. 0.1 wt% SiC, which were added in test 5 (018_08_DMC), did not only fail in causing a fining of the structure, but also seemed to prevent effective photopolymerization. The use of 0.1 wt% UHMW-PE as a nucleating agent in test 6 (024_08_DMC) showed no visible influence on

the structure of the growing DMC crystals. At the surface of the sample, cracks started to form near the low end-temperature during cooling.

Test 7 (038_08_DMC), where ETPP was introduced as a photoinitiator, also contained 0.25 wt% Si_3N_4. While the nucleating agent had no mayor visible effect on the growing crystal structure, the photoinitiator proved to work with dimethyl carbonate as a solvent, resulting in successful curing of the sample. Aside from lowering the Si_3N_4 content to 0.2 wt% in test 8 (040_08_DMC), the reduced stirring time of PSZ and TT of 75 min did not seem to affect the sample fabrication in a negative way. Because of this observation, the following test 9 (041_08_DMC) had only 30 min stirring time. A sample could be obtained, looking alike to the ones produced with higher stirring times. Tests 10 & 11 (042_08_DMC & 044_08_DMC) showed that a PSZ/TT loading of either 20 wt% or 30 wt% also could be used successfully.

Bornyl acetate

When Test 1 (026_08_BA) was performed, no freezing had occurred when the low-temperature set point of -137 °C was reached. When heating up, the whole solution froze at -45 °C in a matter of a few seconds. The sample could not be used further. Because of this extreme supercooling, bornyl acetate itself was used as a nucleating agent in test 2 (027_08_BA) by covering the bottom of the casting platform and freezing a small layer prior to the actual casting. This proved to work excellently by having provided nucleating agents of the solvent itself. Addition of 0.2 wt% Si_3N_4 as a nucleating agent during test 3 (028_08_BA) led to a sample, finer in structure than 027_08_BA, without cracks or other visible defects and inhomogeneities.

To see if other nucleating agents would work as well as Si_3N_4, 0.2 wt% SiC was used for test 4 (029_08_BA). The SiC seemed to absorb too much of the light and thus the polymerization did not work to the core of the sample. Only the outer 3 mm could be cured, which was obvious when the inside of the sample leaked out after removing the “cured” sample from the freeze caster. Test 5 (030_08_BA) was using UHMW-PE as a nucleating agent. The desired effect of fining the structure by providing nucleation seeds could hardly be observed at all. Due to its colour (transparent), absorption was not an issue and curing to the core of the sample possible.

Test 6 (035_08_BA) was performed to observe the effects of a higher Si_3N_4 content, being 0.5 wt% this time. Sublimation of the solvent was causing problems, because it led to formation of small cracks in the sample. With a reduced Si_3N_4 content of 0.4 wt% in test 7 (036_08_BA), cracks were forming during sublimation, like with 035_08_BA. Tests 8 & 9 (045_08_BA & 046_08_BA) had even lower Si_3N_4 contents of 0.3 wt% and 0.25 wt% respectively. Crack formation during sublimation still occurred. As 0.2 wt% nucleating agent seemed to be the limit, a test (047_08_BA) was done to see if irradiation time could be lowered. 40 min curing time instead of 60 min were enough to successfully fabricate a sample.

4.3 Freezing front velocity

The freezing front velocity v_f at a cooling rate of 8 K/min, measured for the solvents p-xylene, dimethyl carbonate and bornyl acetate, is displayed in Table 14. Dimethyl carbonate with a v_f of 0.94 & 0.98 mm/min shows slightly higher values than p-xylene and bornyl acetate, which range from 0.84 – 0.91 mm/min. Values for camphene had been measured in prior work of the research group by Richard Obmann and amount to 1.38 ± 0.12 mm/min [4].

Table 14: Freezing front velocity for samples cast with a cooling rate of 8 K/min; for sample fabrication method see section 3.5

Sample	Solvent	Photoinitiator	Freezing front velocity v_f (mm/min)
075_Xyl_25	p-Xylene	ETPP	0.84
076_Xyl_25	p-Xylene	CQ	0.91
078_DMC_25	Dimethyl carbonate	ETPP	0.98
082_DMC_25	Dimethyl carbonate	CQ	0.94
084_BA_25	Bornyl acetate	ETPP	0.87
086_BA_25	Bornyl acetate	CQ	0.86

4.4 Influence of tetrathiol (TT) concentration on polymerization behaviour

The following section deals with the influence of TT concentration on polymerization behaviour. The experimental part can be found in section 3.4.7.

4.4.1 Testing with 470 nm lamp

Table 15 shows that, as expected, an increasing vinyl group / thiol group ratio results in slower viscosity increase and solidification. Viscosity was not measured instrumentally but observed visually by periodically tilting the test vial after every 30 s. From a molar ratio of 2.5 on, no significant viscosity increase can be noticed, let alone any solidification. Viscosity in the vial with a molar ratio of 5.1 stayed so low during and after irradiation that after one day the Si_3N_4 had settled to the ground. Testing was always stopped after 10 min of irradiation because the freeze-cast mixture is typically polymerized at much lower temperatures which will result in even longer needed irradiation times. Knowing that temperature plays a very important role in reaction kinetics one can imagine what a temperature drop of 40 K will mean for the polymerisation rate. Photos showing the test vials are depicted in Figure 22.

Table 15: Influence of tetrathiol concentration on polymerisation behaviour, testing with 470 nm lamp

PSZ/TT mass ratio	Vinyl/thiol molar ratio	Start of viscosity increase (min)	Solidification (min)
2.7	1.0	2.5	4
3.3	1.2	2.5	4
4.0	1.5	3	5
4.9	1.9	4	6
6.5	2.5	-	-
9.1	3.5	-	-
13.5	5.1	-	-

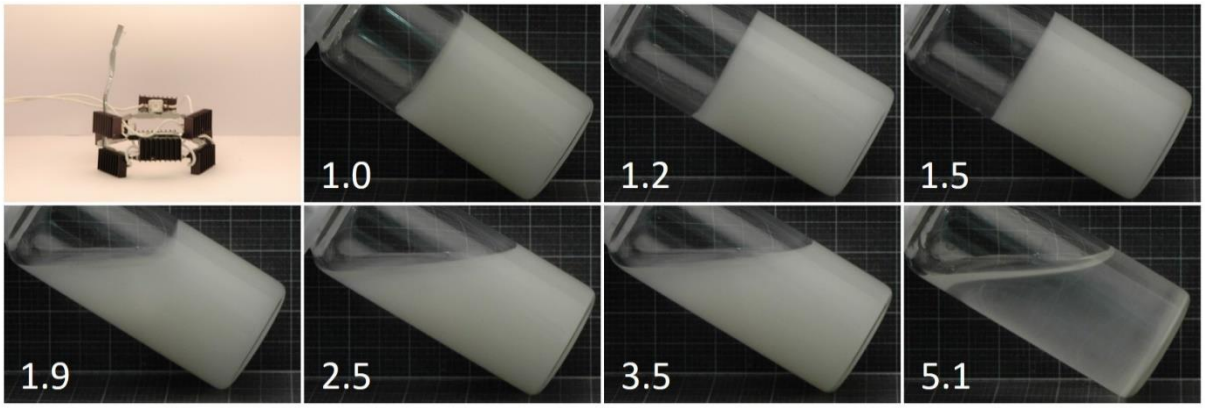

Figure 22: Curing was performed with 470 nm (The array is shown in the leftmost picture of the first row). The other pictures are the test vials after 10 min of irradiation at room temperature; the numbers show the molar ratios of vinyl groups / thiol groups in the solution

4.4.2 Testing with 400 nm lamp

Table 16 shows that, as expected, an increasing vinyl group / thiol group ratio results in slower viscosity increase and solidification. Viscosity was not measured instrumentally but observed visually by periodically tilting the test vial after every 10 s. From a molar ratio of 3.4 on, no significant viscosity increase can be noticed, let alone any solidification. Testing was stopped after 2 min of irradiation for molar ratios of 1.0, 1.3, 1.5 and 1.9 because the polymerisation rate was so high that after less than 30 s the whole mixture had been solidified. Molar ratios of 2.5, 3.4 and 5.4 were irradiated for 10 min. This is because after 2 min the reaction was not finished, or no visual change could be seen yet. Photos showing the test vials are depicted in Figure 23.

Table 16: Influence of tetrathiol concentration on polymerisation behaviour, testing with 400 nm lamp

PSZ/TT mass ratio	Vinyl/thiol molar ratio	Start of viscosity increase (min)	Solidification (min)
2.7	1.0	< 0.5	< 0.5
3.3	1.3	< 0.5	< 0.5
3.9	1.5	< 0.5	< 0.5
5.0	1.9	< 0.5	< 0.5
6.5	2.5	1	3
8.9	3.4	-	-
14.1	5.4	-	-

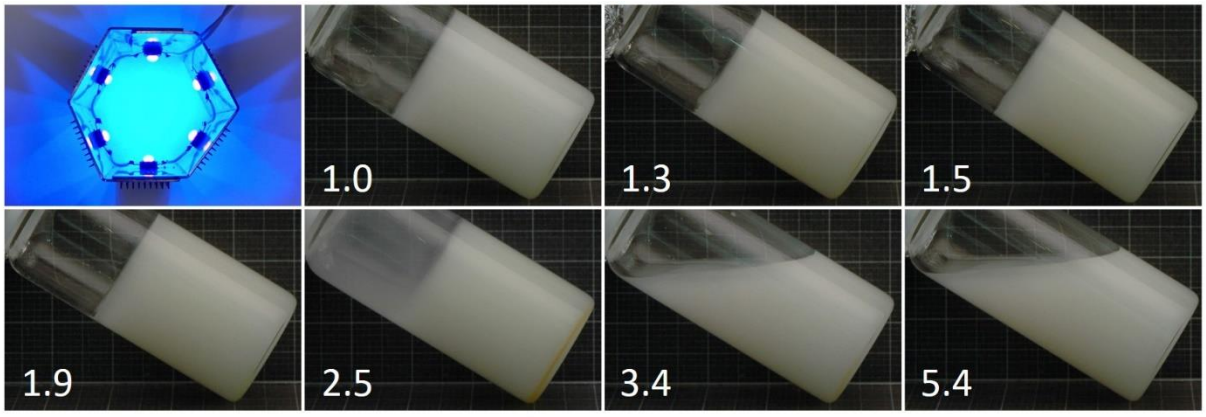

Figure 23: Curing was performed with 400 nm (The array is shown in the leftmost picture of the first row). The other pictures are the test vials after 2 min (1.0, 1.3, 1.5, 1.9) and after 10 min (2.5, 3.4, 5.4) of irradiation at room temperature; the numbers show the molar ratios of vinyl groups / thiol groups in the solution

4.5 Influence of solvent & nucleating agent on pore morphology

The choice of solvent is one of the most influential parameters on microstructure and pore morphology. Figure 24 shows the morphology of samples fabricated without the addition of any nucleating agent. Figure 25 & Figure 26 depict transversal cuts of the microstructures of camphene, p-xylene, dimethyl carbonate and bornyl acetate. These samples were created without the addition of any nucleating agent.

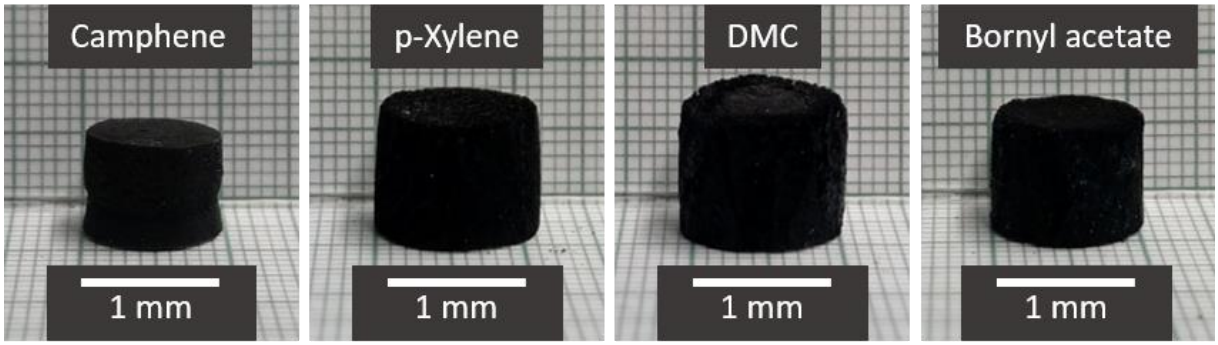

Figure 24: Morphology of samples fabricated without nucleating agent and a PSZ/TT loading of 25 wt%; Samples 071_Cam_25, 075_Xyl_25, 078_DMC_25, 084_BA_25

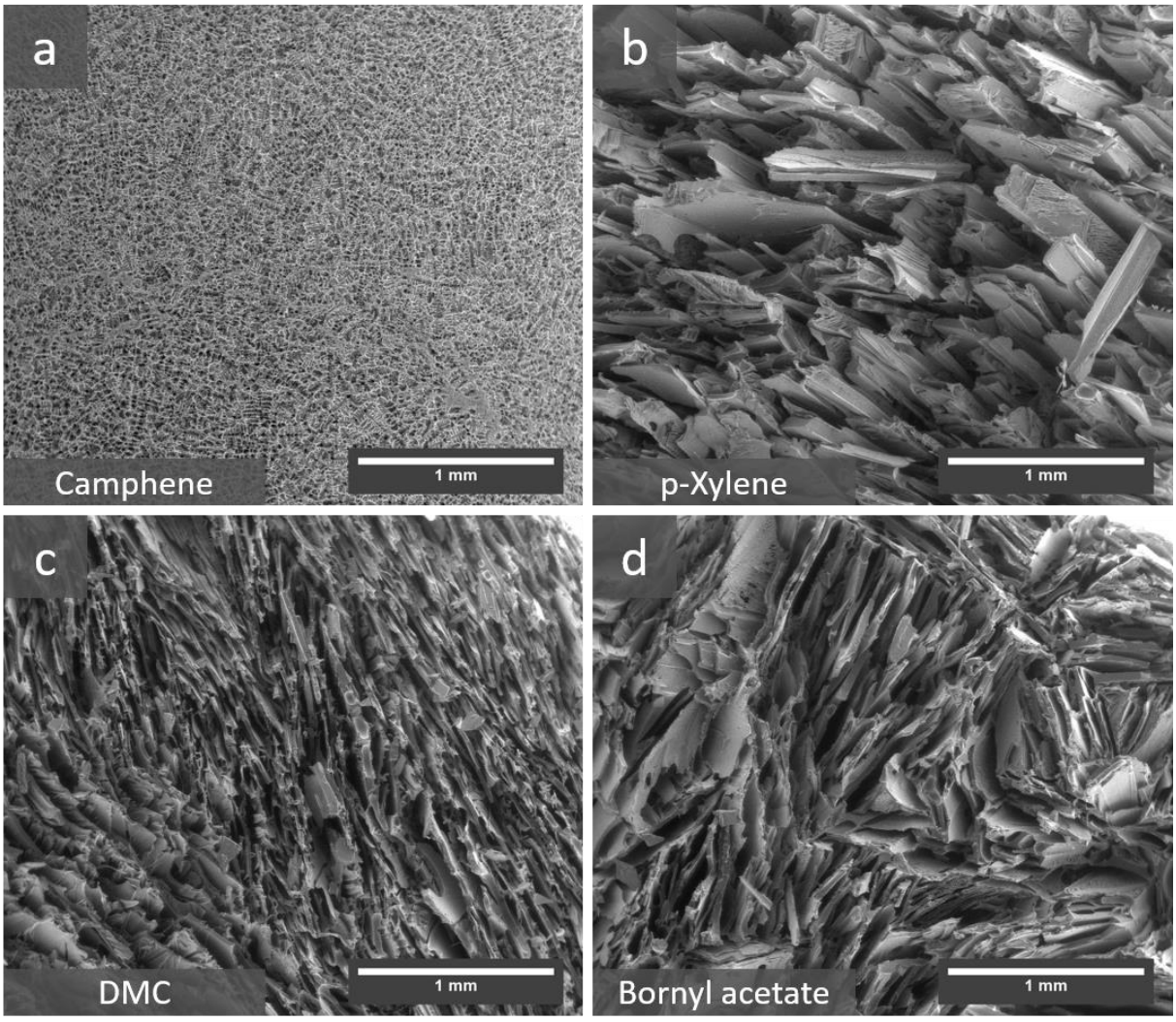

Figure 25: Transversal cut (perpendicular to the freezing direction) through the samples, cast without nucleating agent; PSZ/TT loading was 25 wt%; fabrication after method in section 3.5; (a) camphene, 071_Cam_25 (b) p-xylene, 075_Xyl_25 (c) dimethyl carbonate, 078_DMC_25 (d) bornyl acetate, 084_BA_25; low magnification

Camphene (Figure 26 (a)) shows the finest pore morphology of the four solvents. The pore size and visible features are well below 50 µm. Branching, which is typical for camphene, can be seen in the picture. There seem to be lateral connections between the pores. p-Xylene (Figure 26 (b)) presents a very coarse structure with large spacings between the platelets. Connecting bridges are hardly visible, but some smaller lamellar features are covering the larger platelets. Unidirectionality of the pores is clearly existent. Dimethyl carbonate (Figure 26 (c)) shows a lamellar structure with a decent amount of connecting bridges. The structure in this form is the second finest of the four solvents shown, with pronounced unidirectional channel-like open pores. Bornyl acetate (Figure 26 (d)) presents a structure, which resembles dimethyl carbonate. Lamellas are visible, but the spacing between them is much larger than for dimethyl carbonate.

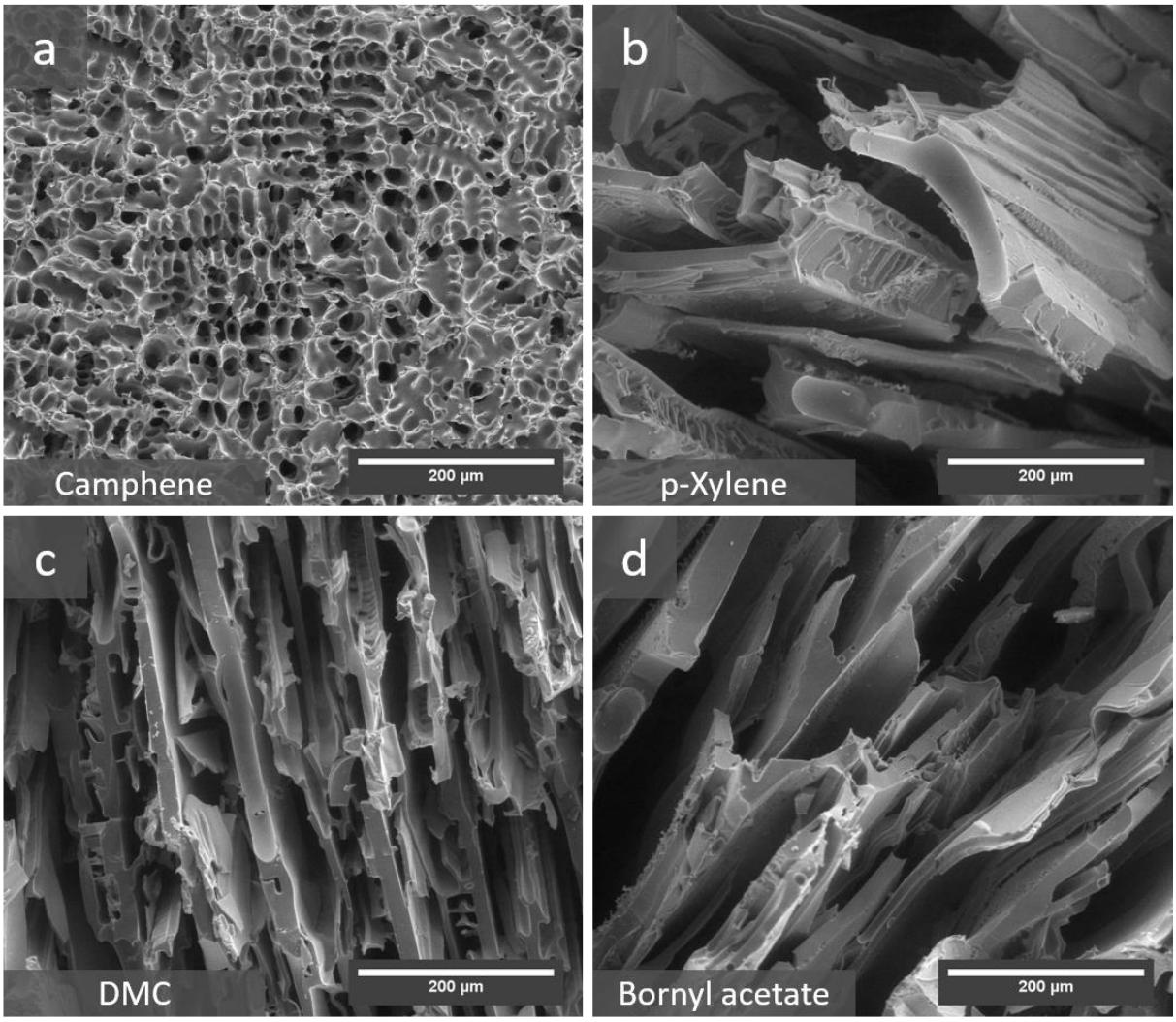

Figure 26: Transversal cut (perpendicular to the freezing direction) through the samples, cast without nucleating agent; PSZ/TT loading was 25 wt%; fabrication after method in section 3.5; (a) camphene, 071_Cam_25 (b) p-xylene, 075_Xyl_25 (c) dimethyl carbonate, 078_DMC_25 (d) bornyl acetate, 084_BA_25; high magnification

Figure 27 depicts a longitudinal cut of the microstructures of camphene, p-xylene, dimethyl carbonate and bornyl acetate. The dendritic pore morphology of camphene (Figure 27 (a)) is clearly visible. p-Xylene (Figure 27 (b)) shows interesting lamellar and dot-like features at the surface of the large platelets, which have a size of several hundred micrometres. Growth of the platelets does not occur vertically but tilted to some degree. The lamellas seem to be too small to act as effective structure-strengthening connecting bridges. The lamellar structure of dimethyl carbonate (Figure 27 (c)) shows the unidirectionality of the pores in this longitudinal view. The lamellas of bornyl acetate (Figure 27 (d)) are partially covered with small holes.
The morphology of the samples fabricated with nucleating agent (except for camphene) and a PSZ/TT loading of 25 wt% can be seen in Figure 28.

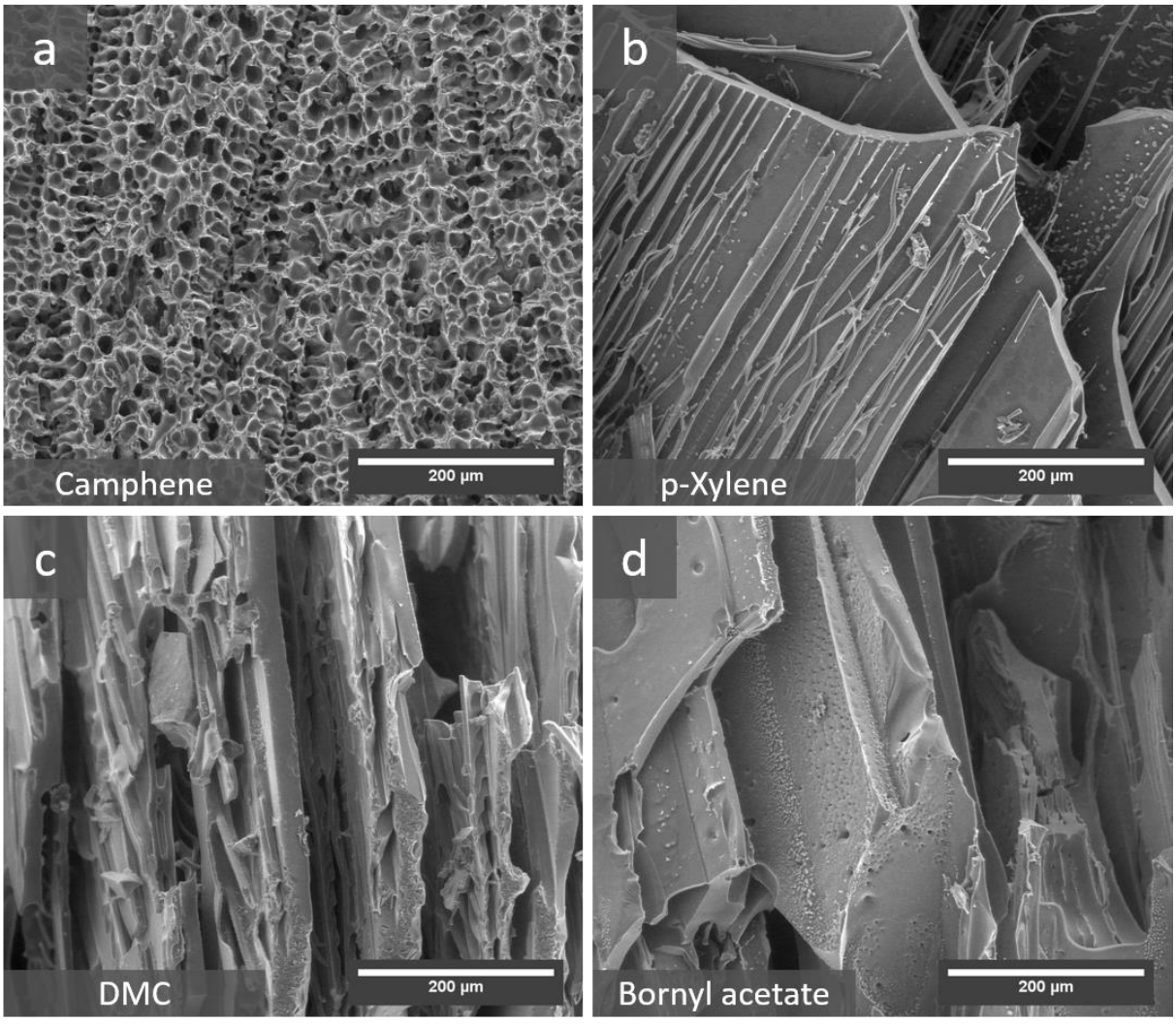

Figure 27: Longitudinal cut (parallel to the freezing direction) through the samples, cast without nucleating agent; PSZ/TT loading was 25 wt%; fabrication after method in section 3.5; (a) camphene, 071_Cam_25 (b) p-xylene, 075_Xyl_25 (c) dimethyl carbonate, 078_DMC_25 (d) bornyl acetate, 084_BA_25; high magnification

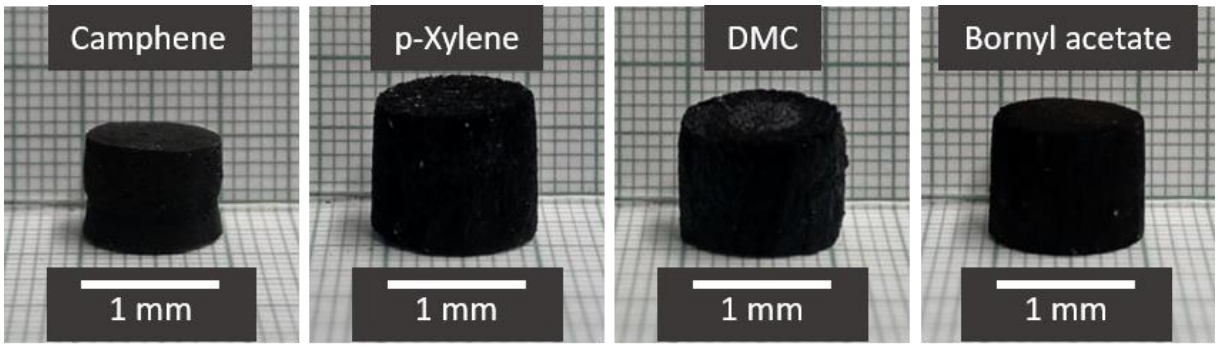

Figure 28: Morphology of samples fabricated with nucleating agent (except for camphene) and a PSZ/TT loading of 25 wt%; Samples 071_Cam_25, 111_Xyl_25, 109_DMC_25, 110_BA_25

Figure 29 & Figure 30 show the transversal cuts of the microstructure of camphene, p-xylene, dimethyl carbonate and bornyl acetate. The last three had Si_3N_4 added to the casting solution as a nucleating agent. Sample fabrication including Si_3N_4 was not possible for camphene. For comparison purposes, a camphene picture with its dendritic pores (Figure 30 (a)) was added to the figure. p-Xylene (Figure 30 b)) generated a very coarse structure. Directionality is still existent though. Small groove-like features cover the big platelets and are oriented perpendicular to the freezing direction.
The dimethyl carbonate sample (Figure 30 (c)) shows a lamellar structure with some other interesting features. These are rectangular channels as well as some spirals. The structure obtained with bornyl acetate (Figure 30 (d)) consists of spiral-like channels with some circular-shaped pores as well.

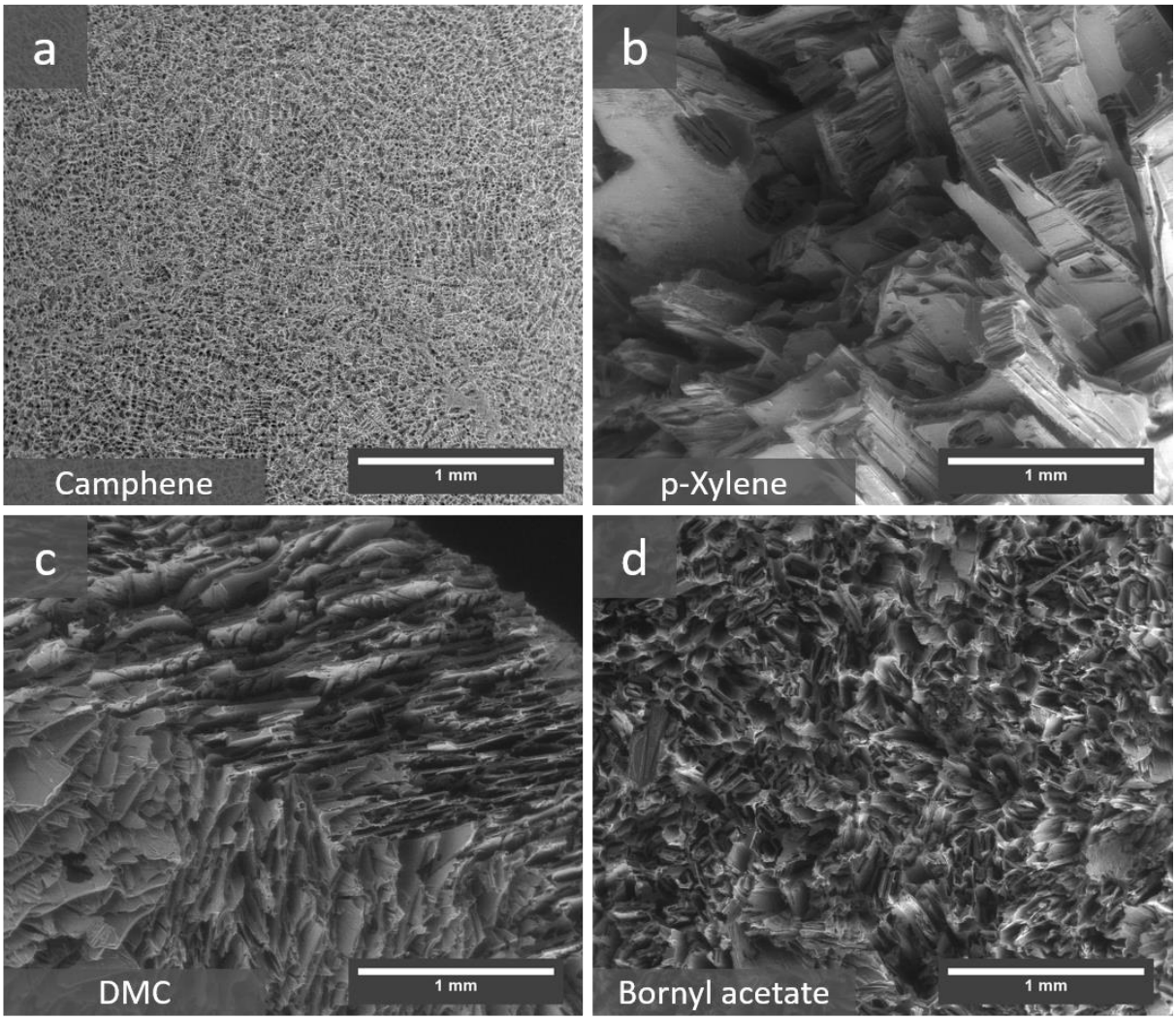

Figure 29: Transversal cut (perpendicular to the freezing direction) through the samples, cast with nucleating agent; PSZ/TT loading was 25 wt%; fabrication after method in section 3.6, camphene after section 3.5; (a) camphene, 071_Cam_25 (b) p-xylene, 111_Xyl_25 (c) dimethyl carbonate, 109_DMC_25 (d) bornyl acetate, 110_BA_25; low magnification

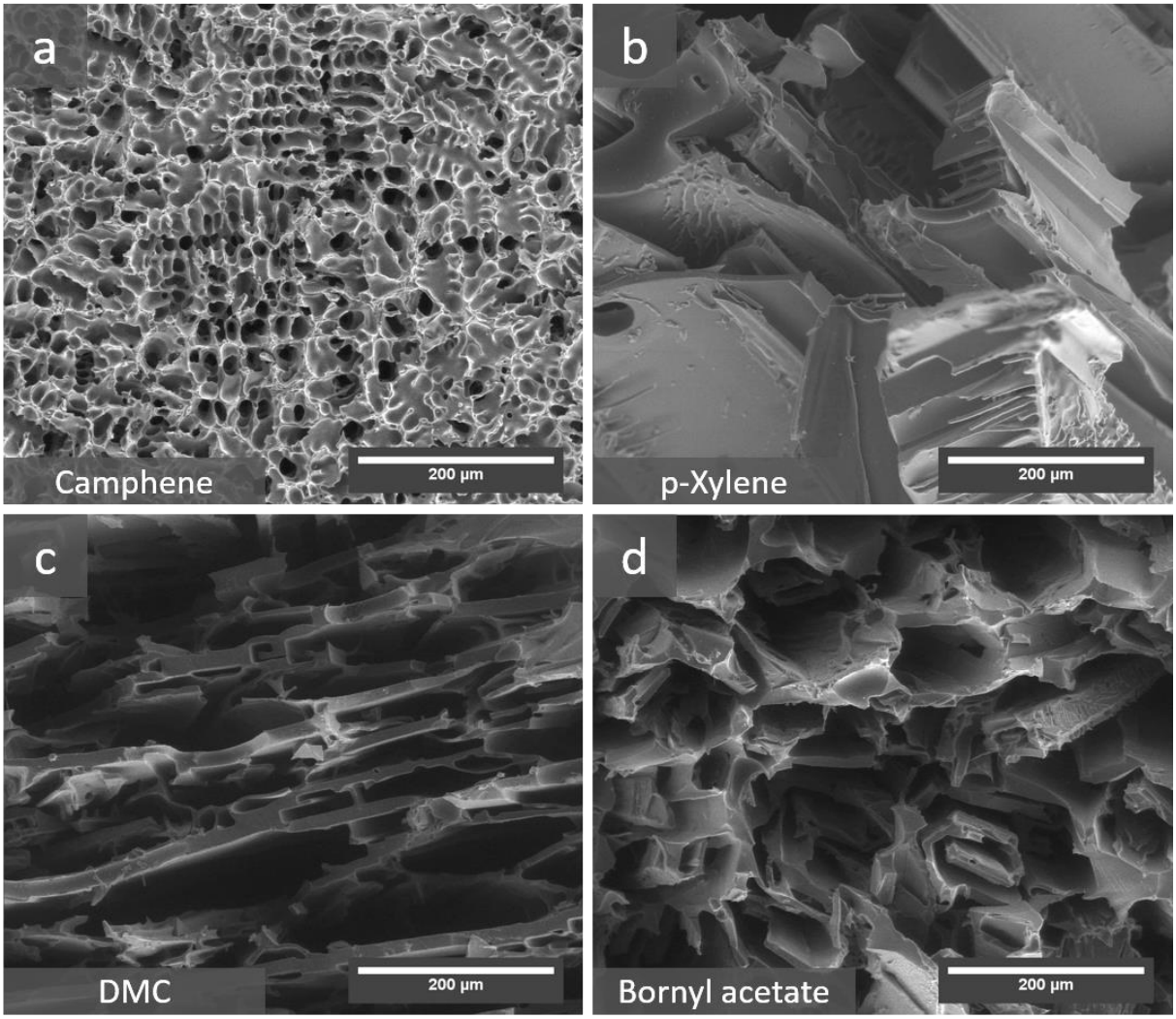

Figure 30: Transversal cut (perpendicular to the freezing direction) through the samples, cast with nucleating agent; PSZ/TT loading was 25 wt%; fabrication after method in section 3.6, camphene after section 3.5; (a) camphene, 071_Cam_25 (b) p-xylene, 111_Xyl_25 (c) dimethyl carbonate, 109_DMC_25 (d) bornyl acetate, 110_BA_25; high magnification

The microstructures depicted in Figure 31 show the longitudinal cuts through the samples fabricated with the addition of Si_3N_4 as a nucleating agent, apart from the camphene sample (Figure 31 (a)). The coarse structure of the p-xylene sample, which is interspersed with small groove-like features, can be seen in Figure 31 (b). The dimethyl carbonate sample (Figure 31 (c)) shows lamellas and small areas that look like some melting occurred during curing. The use of bornyl acetate, in combination with a nucleating agent, resulted in Figure 31 (d). A lamellar structure with high directionality is visible here.

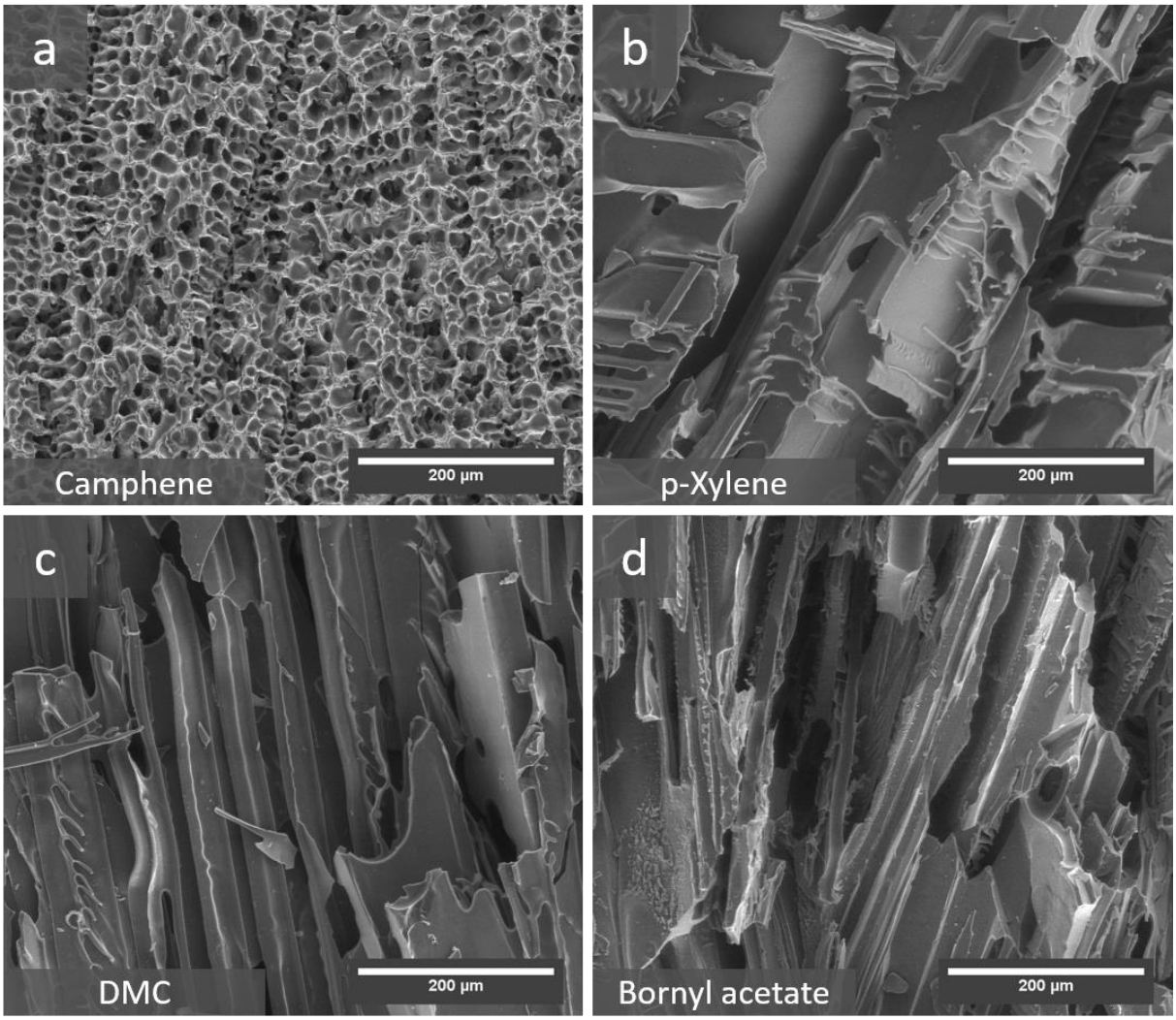

Figure 31: Longitudinal cut (parallel to the freezing direction) through the samples, cast with nucleating agent; PSZ/TT loading was 25 wt%; fabrication after method in section 3.6, camphene after section 3.5; (a) camphene, 071_Cam_25 (b) p-xylene, 11_Xyl_25 (c) dimethyl carbonate, 109_DMC_25 (d) bornyl acetate, 110_BA_25; high magnification

4.6 Influence of PSZ/TT loading and Si_3N_4 on the pore morphology of bornyl acetate samples

Figure 32 – Figure 39 show the microstructure obtained by freeze casting with bornyl acetate as a solvent in different magnifications. PSZ/TT loading was varied and at each level one sample was cast with, and one without Si_3N_4. Transversal cuts, perpendicular to the freezing direction, as well as longitudinal cuts, parallel to the freezing direction, are displayed.

When looking at the transversal cuts, a visible trend shows the microstructure getting denser with increasing loading, which is barely noticeable for smaller loadings up to 25 wt%, but really makes a difference with the higher ones (30 wt%, 35 wt% and 40 wt%). A striking difference is made by addition of Si_3N_4 to the sample. The structure gets refined with the nucleating agent and changes drastically. The previously lamellar-type structure changes to a structure showing spirals, as well as columns. This is especially noticeable for the loadings 15 – 25 wt%. From 30 wt% upwards, the structure type starts to look increasingly lamellar again. Without any nucleating agent, the pore morphology stays lamellar through the whole observed loading range. Disorder, due to different crystal growing orientations, can also be witnessed. The samples with 40 wt% loading show immense crack formation, seen in Figure 36 (e) & Figure 37 (e).

When looking at the longitudinal cuts, the densification of the structure with increasing loading is clearly visible. The addition of the nucleating agent makes a significant difference by fining the structure to a significant extent. It also seems to improve directionality of the structure. Smaller groove-like features perpendicular to the freezing direction evolve for loadings from 15 – 30 wt%, when Si_3N_4 is present. Circular holes are noticeable, especially in some of the samples, that did not include the Si_3N_4. A good example is shown in Figure 35 (d). The crack formation with 40 wt% loading, that could be seen in the transversal cut, is also clearly visible in the longitudinal cut, depicted in Figure 38 (e). The samples without the nucleating agent show some disorder, stemming from different crystal growth orientations.

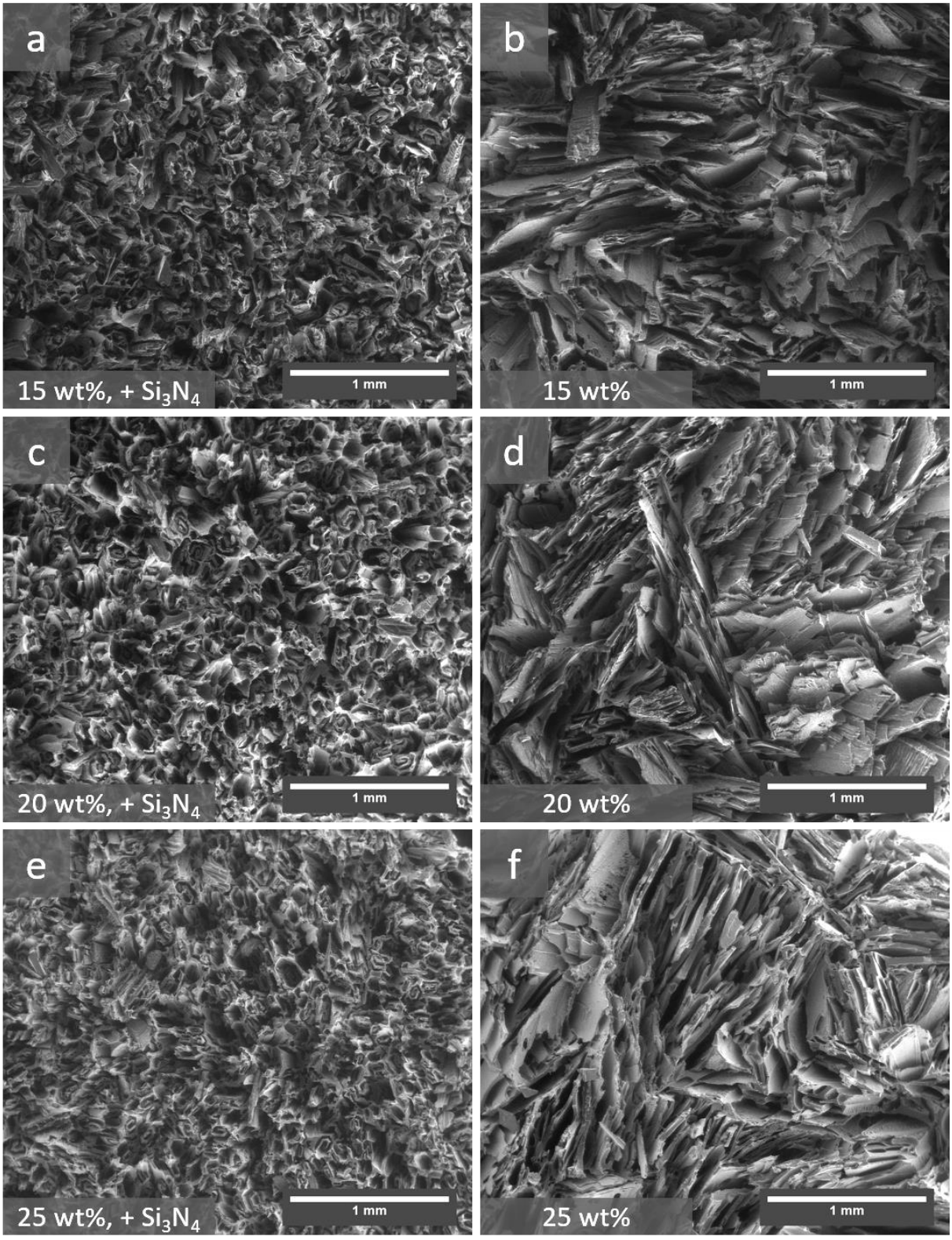

Figure 32: Transversal cut (perpendicular to the freezing direction) through the bornyl acetate samples, fabricated after final method in section 3.6; the corner at the bottom left of each picture states the PSZ/TT loading in wt%, and if 0.2 wt% Si_3N_4 had been added or not; sample (a) 107_BA_15, (b) 108_BA_15, (c) 105_BA_20, (d) 106_BA_20, (e) 102_BA_25, (f) 084_BA_25; low magnification

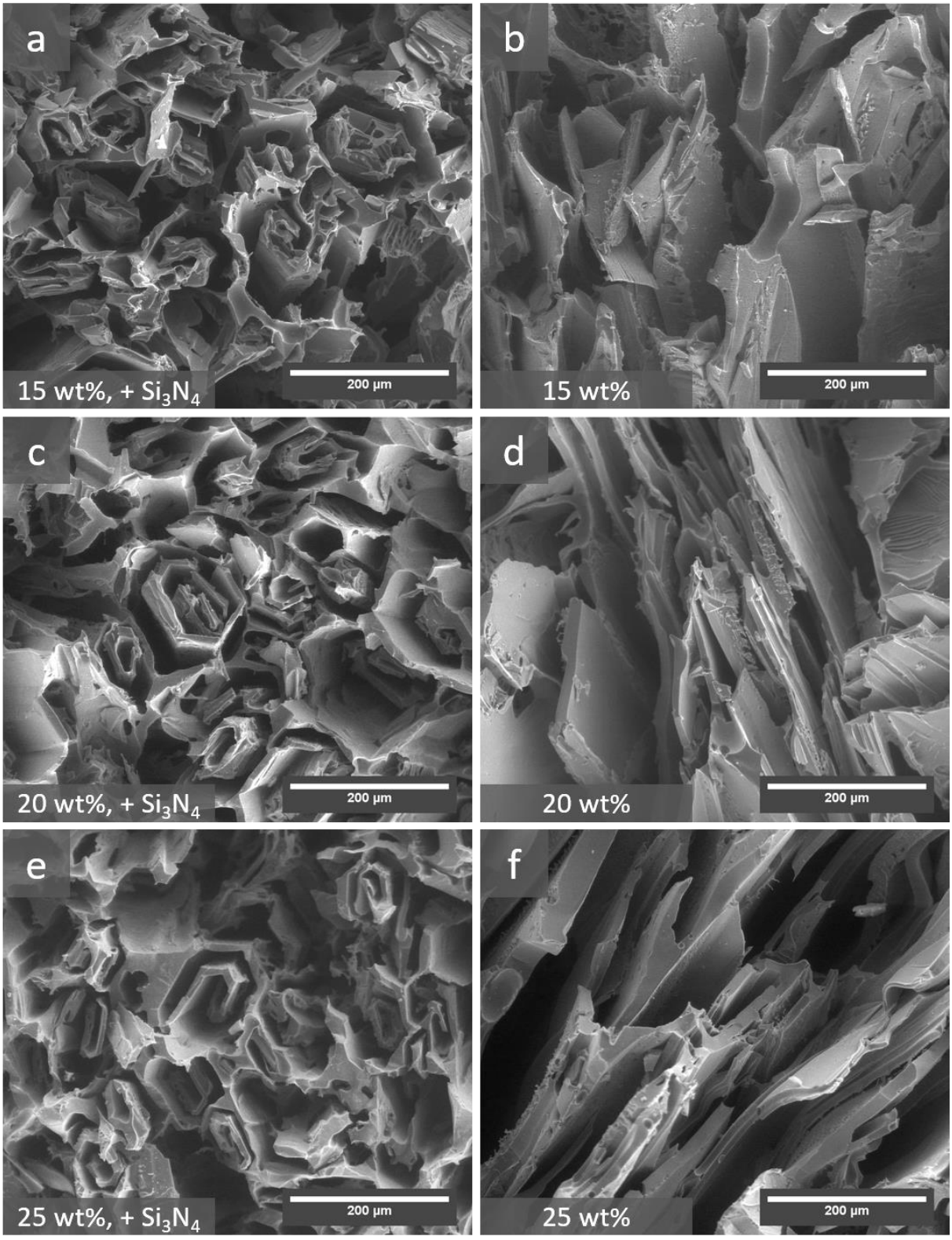

Figure 33: Transversal cut (perpendicular to the freezing direction) through the bornyl acetate samples, fabricated after final method in section 3.6; the corner at the bottom left of each picture states the PSZ/TT loading in wt%, and if 0.2 wt% Si_3N_4 had been added or not; sample (a) 107_BA_15, (b) 108_BA_15, (c) 105_BA_20, (d) 106_BA_20, (e) 102_BA_25, (f) 084_BA_25; high magnification

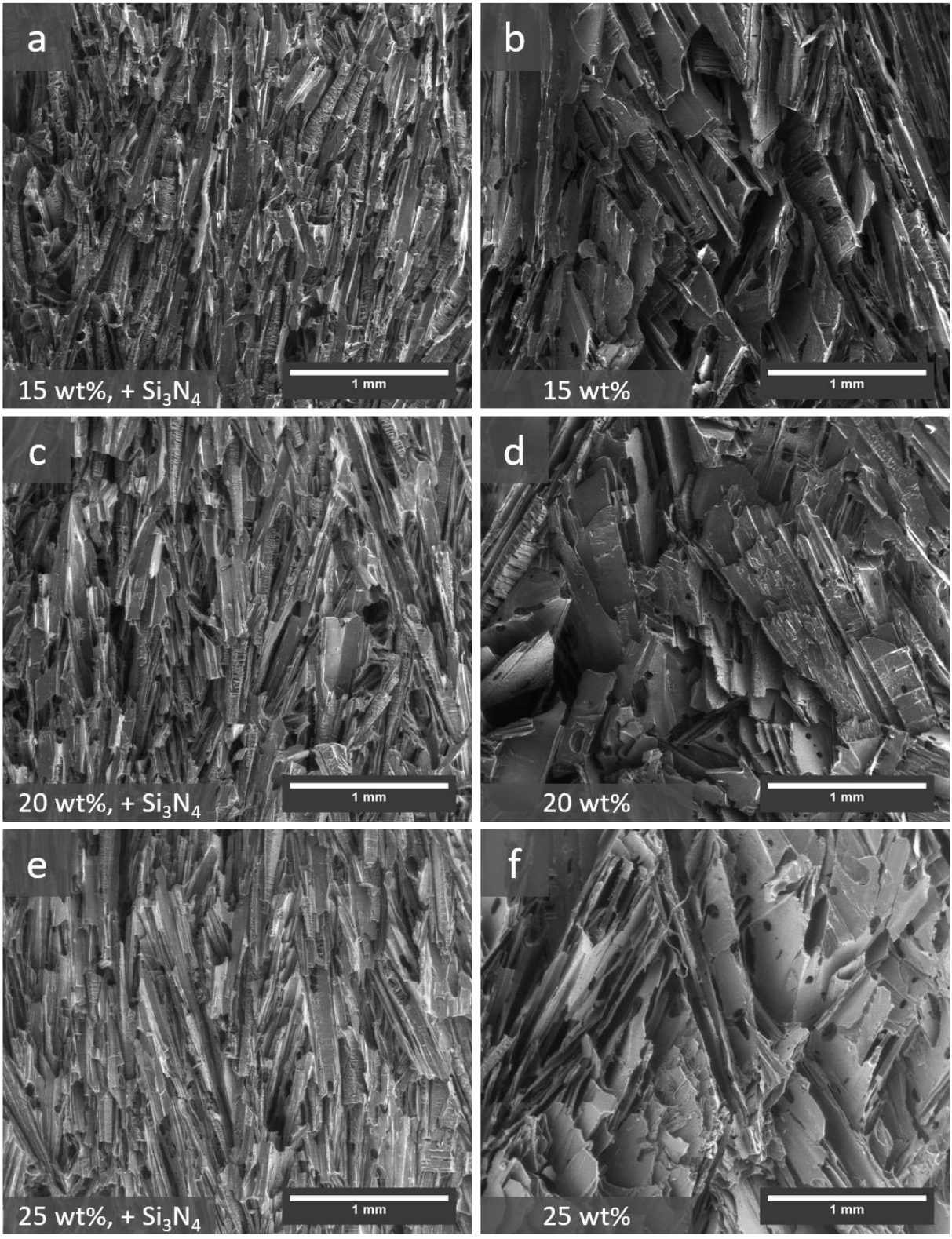

Figure 34: Longitudinal cut (parallel to the freezing direction) through the bornyl acetate samples, fabricated after final method in section 3.6; the corner at the bottom left of each picture states the PSZ/TT loading in wt%, and if 0.2 wt% Si_3N_4 had been added or not; sample (a) 107_BA_15, (b) 108_BA_15, (c) 105_BA_20, (d) 106_BA_20, (e) 102_BA_25, (f) 084_BA_25; low magnification

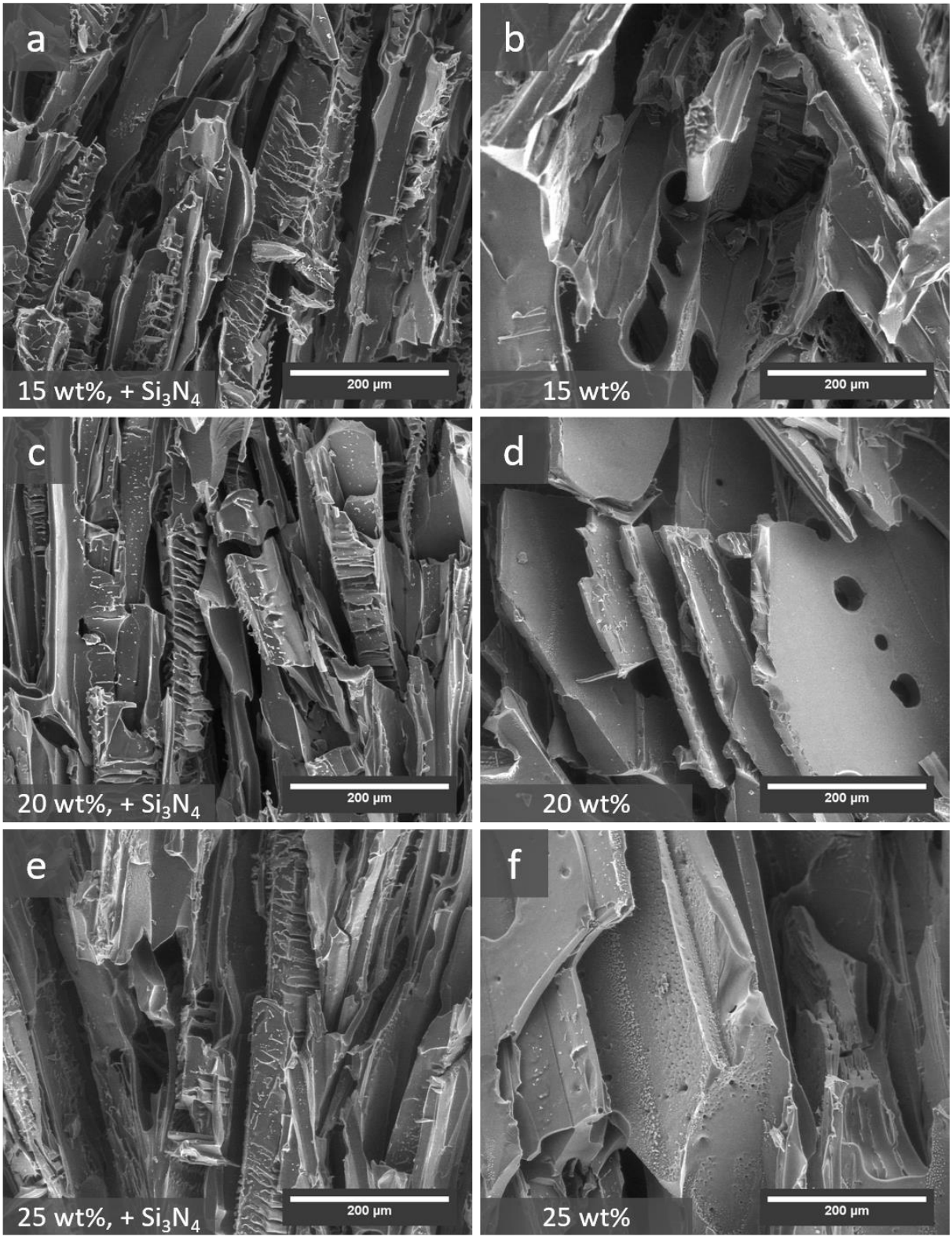

Figure 35: Longitudinal cut (parallel to the freezing direction) through the bornyl acetate samples, fabricated after final method in section 3.6; the corner at the bottom left of each picture states the PSZ/TT loading in wt%, and if 0.2 wt% Si_3N_4 had been added or not; sample (a) 107_BA_15, (b) 108_BA_15, (c) 105_BA_20, (d) 106_BA_20, (e) 102_BA_25, (f) 084_BA_25; high magnification

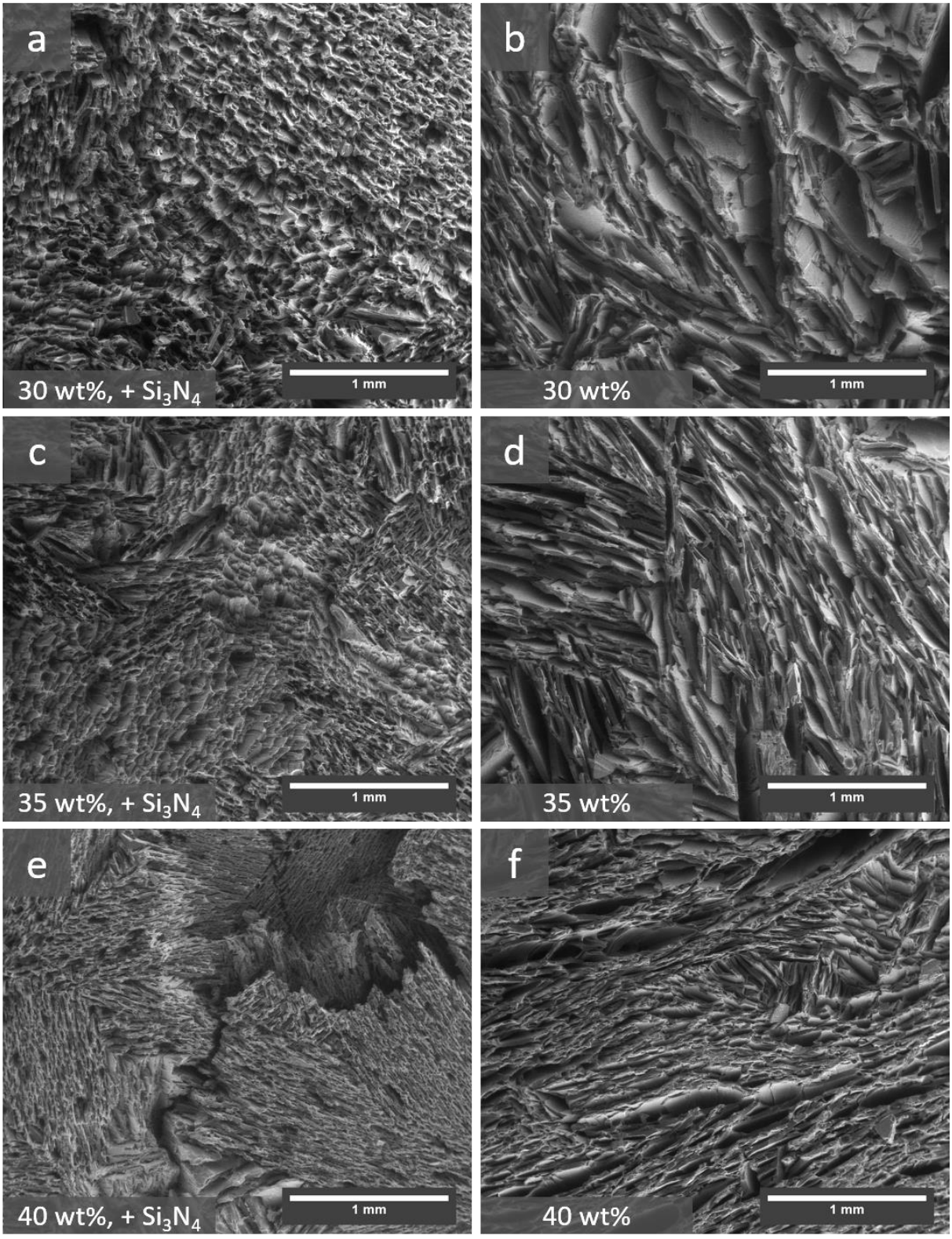

Figure 36: Transversal cut (perpendicular to the freezing direction) through the bornyl acetate samples, fabricated after final method in section 3.6; the corner at the bottom left of each picture states the PSZ/TT loading in wt%, and if 0.2 wt% Si_3N_4 had been added or not; sample (a) 093_BA_30, (b) 094_BA_30, (c) 095_BA_35, (d) 096_BA_35, (e) 097_BA_40, (f) 098_BA_40; low magnification

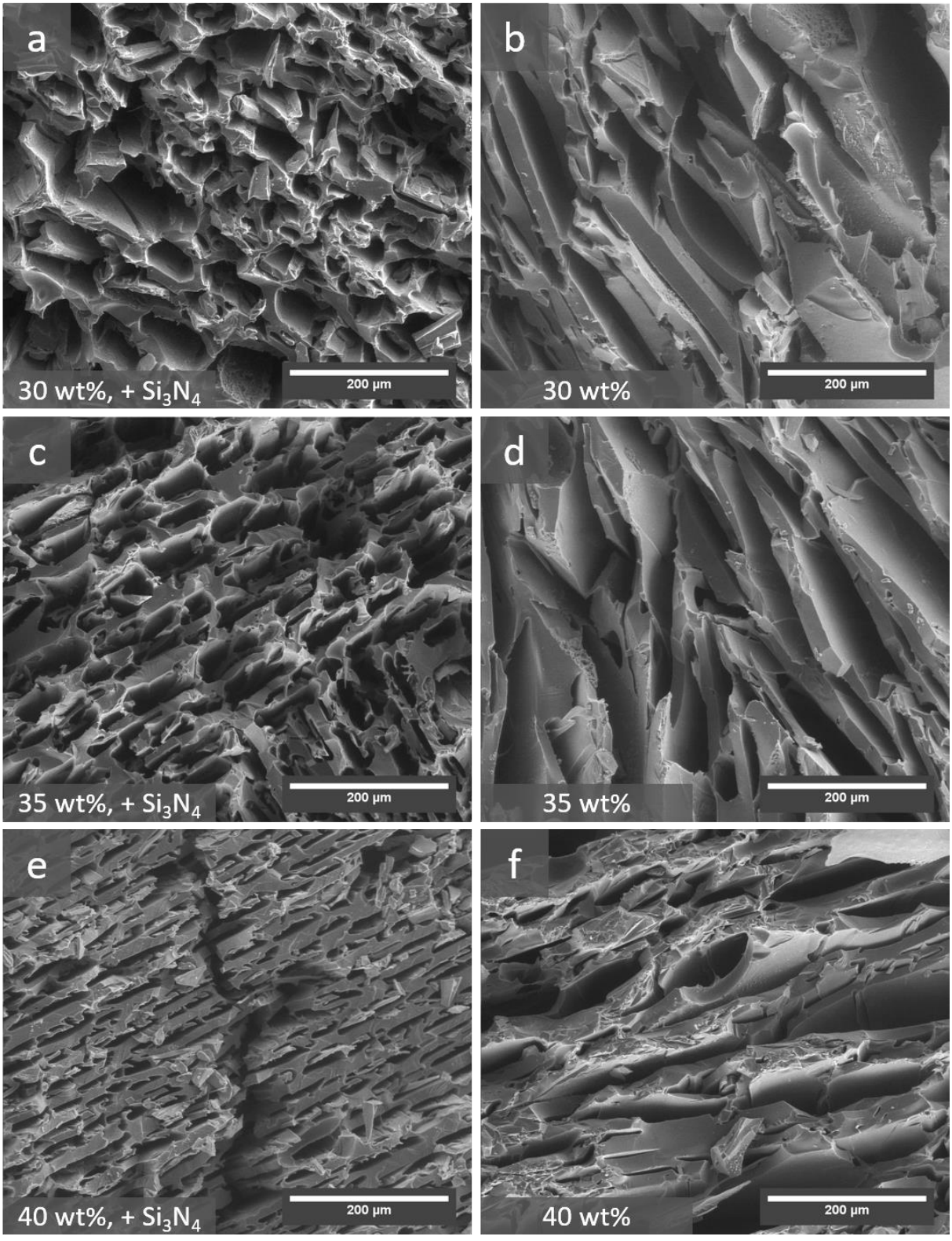

Figure 37: Transversal cut (perpendicular to the freezing direction) through the bornyl acetate samples, fabricated after final method in section 3.6; the corner at the bottom left of each picture states the PSZ/TT loading in wt%, and if 0.2 wt% Si_3N_4 had been added or not; sample (a) 093_BA_30, (b) 094_BA_30, (c) 095_BA_35, (d) 096_BA_35, (e) 097_BA_40, (f) 098_BA_40; high magnification

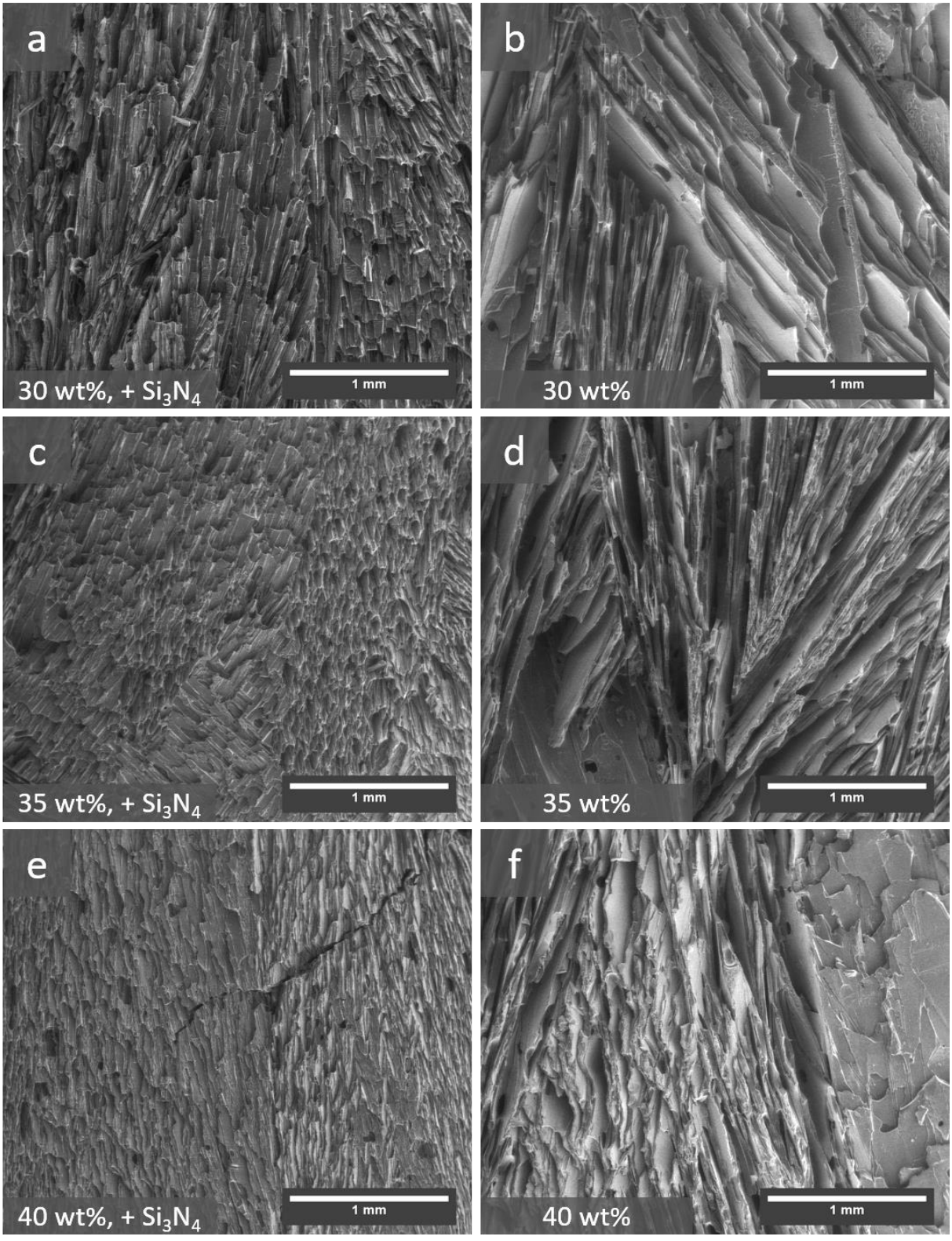

Figure 38: Longitudinal cut (parallel to the freezing direction) through the bornyl acetate samples, fabricated after final method in section 3.6; the corner at the bottom left of each picture states the PSZ/TT loading in wt%, and if 0.2 wt% Si_3N_4 had been added or not; sample (a) 093_BA_30, (b) 094_BA_30, (c) 095_BA_35, (d) 096_BA_35, (e) 097_BA_40, (f) 098_BA_40; low magnification

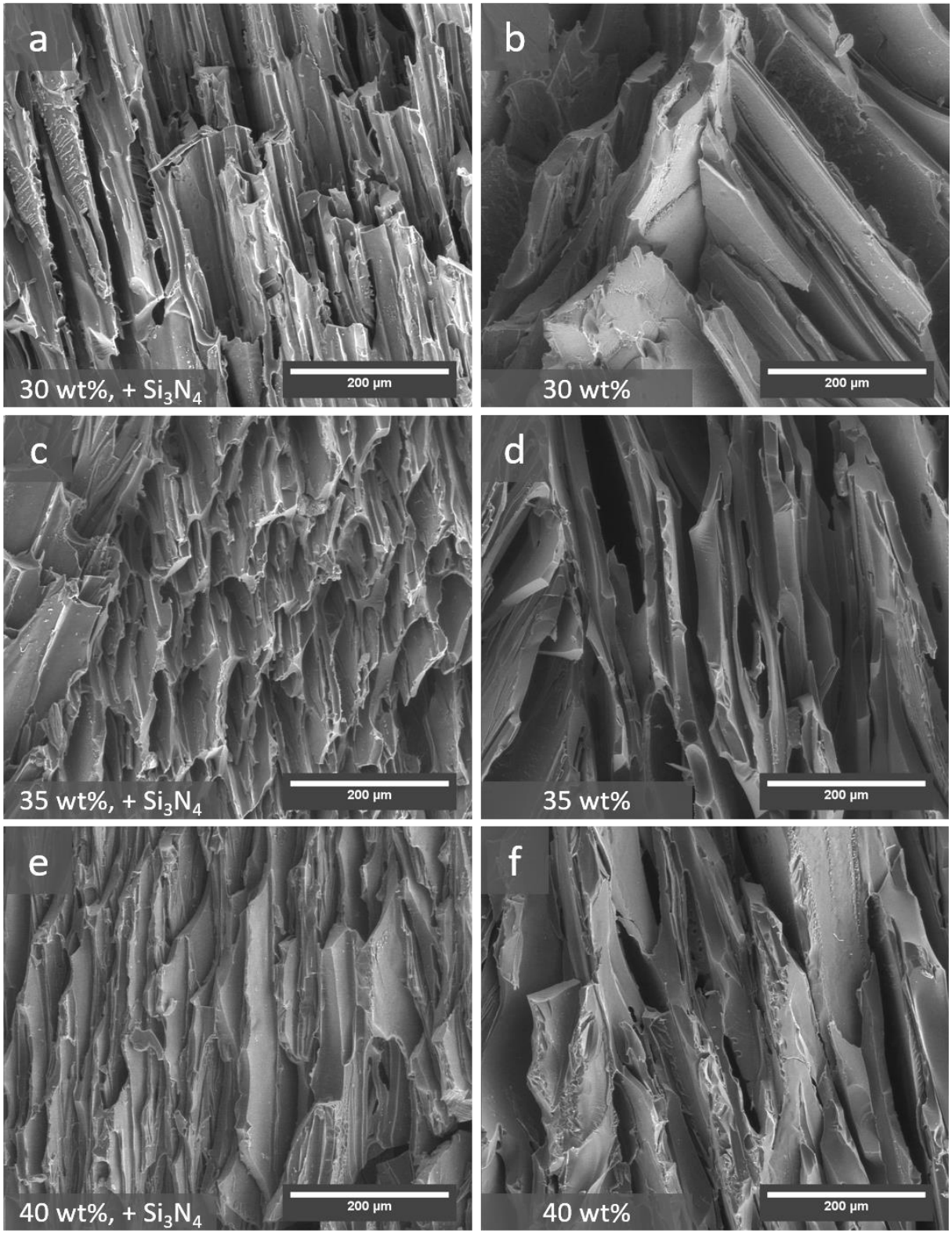

Figure 39: Longitudinal cut (parallel to the freezing direction) through the bornyl acetate samples, fabricated after final method in section 3.6; the corner at the bottom left of each picture states the PSZ/TT loading in wt%, and if 0.2 wt% Si_3N_4 had been added or not; sample (a) 093_BA_30, (b) 094_BA_30, (c) 095_BA_35, (d) 096_BA_35, (e) 097_BA_40, (f) 098_BA_40; high magnification

4.7 Mass loss

The mass loss for bornyl acetate samples with different loading and Si_3N_4 content, which had been produced according to the procedure in section 3.6, is presented in Table 17. No specific trend can be identified with increasing PSZ/TT loading or varying Si_3N_4 content. The mass loss from cured to thermally post-cured sample encompasses 4.6 – 7.7 %, with a mean value of 6.4 ± 1.0 %. The mass loss from thermally post-cured to pyrolyzed sample encompasses 34.8 – 37.1 %, with a mean value of 36.0 ± 0.8 %. The total mass loss from cured to pyrolyzed samples ranges from 41.4 % to 43.4 % with a mean value of 42.4 ± 0.7 %.

Table 18 shows the mass loss for samples produced with different solvents. No camphene sample using Si_3N_4 could be successfully prepared, which is why it is omitted in this table. Comparing the samples obtained from using Si_3N_4 in the fabrication with the ones produced without the nucleating agent, a slight difference can be seen. The mass loss tends to be slightly higher for the samples containing Si_3N_4. The step from cured to thermally post-cured sample shows some noticeable differences with bornyl acetate experiencing 7.2 % loss of mass, whereas dimethyl carbonate loses up to 10.4 % of its mass. The step from thermally post-cured to pyrolyzed sample shows some differences as well with dimethyl carbonate experiencing as little as 30.7 % loss of mass, whereas camphene reaches 35.7 %. Total mass loss from cured to pyrolyzed samples encompasses 41.1 – 44.5 %.
Table 19 shows the mass loss for samples, that had been fabricated for compressive strength testing. The values obtained between curing and thermal post-curing range from 4.3 % to 9.4 %. The values obtained between thermal post-curing and pyrolysis range from 35.1 % to 37.5 %. Total mass loss from cured to pyrolyzed samples ranges from 40.6 ± 1.0 % for dimethyl carbonate, followed by bornyl acetate with 43.5 ± 0.2 %, and p-Xylene with 44.5 ± 0.2 %, to 44.9 ± 1.0 % for camphene.

Table 17: Mass loss for bornyl acetate samples with different loading and Si_3N_4 content; yellow marked samples had 0.012 g Si_3N_4 included in the ansatz, the others did not; Cur = Cured, Therm = Thermally post-cured, Pyr = Pyrolyzed

Sample name	PSZ/TT loading (wt%)	Si_3N_4	Mass (g)			Mass loss (%)		
			Cur	Therm	Pyr	Cur->Therm	Therm->Pyr	Total
107_BA_15	15	YES	0.514	0.479	0.300	6.8	34.8	41.6
108_BA_15	15	NO	0.508	0.471	0.293	7.3	35.0	42.3
105_BA_20	20	YES	0.768	0.723	0.450	5.9	35.5	41.4
106_BA_20	20	NO	0.727	0.672	0.412	7.6	35.8	43.3
102_BA_25	25	YES	0.902	0.844	0.512	6.4	36.8	43.2
084_BA_25	25	NO	1.057	0.981	0.611	7.2	35.0	42.2
093_BA_30	30	YES	1.071	1.02	0.626	4.8	36.8	41.5
094_BA_30	30	NO	1.142	1.089	0.665	4.6	37.1	41.8
095_BA_35	35	YES	1.405	1.322	0.810	5.9	36.4	42.3
096_BA_35	35	NO	1.412	1.329	0.811	5.9	36.7	42.6
097_BA_40	40	YES	1.619	1.495	0.917	7.7	35.7	43.4
098_BA_40	40	NO	1.767	1.655	1.005	6.3	36.8	43.1

Table 18: Mass loss for samples produced with different solvents (Cam = Camphene, Xyl = p-Xylene, DMC = Dimethyl carbonate, BA = Bornyl acetate); samples 071, 075, 078, 084 were produced in the first measurement series described in section 3.5; yellow marked samples 111, 109, 110 were produced using the final method (section 3.6) with 6 mg Si_3N_4 as nucleating agent; Cur = Cured, Therm = Thermally post-cured, Pyr = Pyrolyzed

Sample	Solvent	Mass (g)			Mass loss (%)		
		Cur	Therm	Pyr	Cur->Therm	Therm->Pyr	Total
071_Cam_25	Cam	0.928	0.846	0.515	8.8	35.7	44.5
075_Xyl_25	Xyl	0.863	0.795	0.507	7.9	33.4	41.3
111_Xyl_25	Xyl	0.803	0.721	0.448	10.2	34.0	44.2
078_DMC_25	DMC	0.890	0.797	0.524	10.4	30.7	41.1
109_DMC_25	DMC	1.025	0.932	0.598	9.1	32.6	41.7
084_BA_25	BA	1.057	0.981	0.611	7.2	35.0	42.2
110_BA_25	BA	0.911	0.845	0.521	7.2	35.6	42.8

Table 19: Mass loss for samples fabricated (after final method, section 3.6) for compressive strength testing; BA = Bornyl acetate, DMC = Dimethyl carbonate, Xyl = p-Xylene, Cam = Camphene, Cur = Cured, Therm = Thermally post-cured, Pyr = Pyrolyzed

Sample	Solvent	Mass (g)			Mass loss (%)			
		Cur	Therm	Pyr	Cur-> Therm	Therm ->Pyr	Total	Total mean
099_BA_25	BA	0.907	0.852	0.512	6.1	37.5	43.6	43.5 ± 0.2
100_BA_25	BA	0.974	0.913	0.552	6.3	37.1	43.3	
101_BA_25	BA	0.906	0.845	0.513	6.7	36.6	43.4	
103_BA_25	BA	0.934	0.867	0.524	7.2	36.7	43.9	
104_BA_25	BA	0.923	0.859	0.521	6.9	36.6	43.6	
113_DMC_25	DMC	0.903	0.849	0.529	6.0	35.4	41.4	40.6 ± 1.0
114_DMC_25	DMC	0.965	0.911	0.569	5.6	35.4	41.0	
116_DMC_25	DMC	0.818	0.783	0.495	4.3	35.2	39.5	
117_Xyl_25	Xyl	0.851	0.776	0.473	8.8	35.6	44.4	44.5 ± 0.2
118_Xyl_25	Xyl	0.898	0.814	0.497	9.4	35.3	44.7	
119_Xyl_25	Xyl	0.900	0.817	0.501	9.2	35.1	44.3	
123_Cam_25	Cam	0.927	0.850	0.503	8.3	37.4	45.7	44.9 ± 1.0
124_Cam_25	Cam	0.949	0.869	0.513	8.4	37.5	45.9	
125_Cam_25	Cam	0.901	0.826	0.503	8.3	35.8	44.2	
126_Cam_25	Cam	0.938	0.863	0.526	8.0	35.9	43.9	

4.8 Linear shrinkage

Table 20 shows the linear shrinkage for bornyl acetate samples with different loading and Si_3N_4 content. No relevant differences or trend can be seen, which is why the mean values also have been calculated. The mean values of linear shrinkage for the diameter of the samples shown in Table 20 are 2.6 ± 1.7 % from curing to thermal post-curing, 27.3 ± 1.6 % from thermal post-curing to pyrolysis and 30.0 ± 1.1 % in total. The mean values of linear shrinkage for the height of the samples shown in Table 20 are 3.0 ± 1.8 % from curing to thermal post-curing, 27.8 ± 1.2 % from thermal post-curing to pyrolysis and 30.8 ± 1.3 % in total.

Table 21 shows the linear shrinkage for samples produced with different solvents and methods. The linear shrinkage tends to be higher for the samples, which were produced with the final method (section 3.6), containing Si_3N_4. It is unclear though, if this result is statistically relevant, because only one sample was produced under the same conditions.
Table 22 shows the linear shrinkage for samples fabricated for compressive strength testing. Values vary quite a bit, depending on the observed step. To get a clearer image, an extra table (Table 23) lists the mean values for the samples fabricated with the same solvent and under the same conditions. Linear shrinkage is almost the same for diameter and height, varying most with bornyl acetate with 1.4 % difference in total value.

Table 20: Linear shrinkage for bornyl acetate samples with different loading and Si_3N_4 content; yellow marked samples had 0.012 g Si_3N_4 included in the ansatz, the others did not; c = Cured, t = Thermally post-cured, p = Pyrolyzed

Sample name	PSZ/TT loading (%)	Si_3N_4	Diameter (mm)			Linear shrinkage (%)			Height (mm)			Linear shrinkage (%)		
			c	t	p	c->t	t->p	Total	c	t	p	c->t	t->p	Total
107_BA_15	15	YES	14.8	14.6	10.4	1.4	28.4	29.7	11.6	11.0	7.9	5.2	26.7	31.9
108_BA_15	15	NO	14.9	14.2	10.5	4.7	24.8	29.5	11.5	11.2	8.1	2.6	27.0	29.6
105_BA_20	20	YES	15.0	15.0	10.6	0.0	29.3	29.3	12.3	12.3	8.9	0.0	27.6	27.6
106_BA_20	20	NO	15.5	14.8	10.6	4.5	27.1	31.6	11.6	11.0	7.9	5.2	26.7	31.9
102_BA_25	25	YES	15.7	15.2	10.8	3.2	28.0	31.2	12.4	12.2	8.6	1.6	29.0	30.6
084_BA_25	25	NO	14.9	14.8	10.7	0.7	27.5	28.2	14.3	13.6	9.8	4.9	26.6	31.5
093_BA_30	30	YES	15.5	15.0	10.7	3.2	27.7	31.0	11.9	11.5	8.1	3.4	28.6	31.9
094_BA_30	30	NO	15.5	15.4	10.7	0.6	30.3	31.0	12.7	12.5	8.8	1.6	29.1	30.7
095_BA_35	35	YES	15.7	15.0	11.0	4.5	25.5	29.9	13.0	12.3	8.9	5.4	26.2	31.5
096_BA_35	35	NO	15.3	15.0	11.0	2.0	26.1	28.1	13.3	13.0	9.1	2.3	29.3	31.6
097_BA_40	40	YES	15.7	15.0	11.0	4.5	25.5	29.9	12.9	12.5	9.0	3.1	27.1	30.2
098_BA_40	40	NO	15.5	15.1	10.8	2.6	27.7	30.3	14.1	13.9	9.8	1.4	29.1	30.5

Table 21: Linear shrinkage for samples produced with different solvents (Cam = Camphene, Xyl = p-Xylene, DMC = Dimethyl carbonate, BA = Bornyl acetate); samples 071, 075, 078, 084 were produced in the first measurement series described in section 3.5; yellow marked samples 111, 109, 110 were produced using the final method (section 3.6) with 6 mg Si_3N_4 as nucleating agent; c = Cured, t = Thermally post-cured, p = Pyrolyzed

Sample	Solvent	Diameter (mm)			Linear shrinkage (%)			Height (mm)			Linear shrinkage (%)		
		c	t	p	c->t	t->p	Total	c	t	p	c->t	t->p	Total
071_Cam_25	Cam	14.5	14.4	10.1	0.7	29.7	30.3	11.8	11.3	7.9	4.2	28.8	33.1
075_Xyl_25	Xyl	15.9	15.9	11.6	0.0	27.0	27.0	14.0	13.4	9.8	4.3	25.7	30.0
111_Xyl_25	Xyl	16.7	16.0	11.5	4.2	26.9	31.1	12.9	12.2	8.7	5.4	27.1	32.6
078_DMC_25	DMC	15.5	15.5	11.4	0.0	26.5	26.5	11.8	11.7	9.1	0.8	22.0	22.9
109_DMC_25	DMC	16.2	15.8	11.5	2.5	26.5	29.0	13.4	13.0	9.6	3.0	25.4	28.4
084_BA_25	BA	14.9	14.8	10.7	0.7	27.5	28.2	14.3	13.6	9.8	4.9	26.6	31.5
110_BA_25	BA	15.4	15.1	10.8	1.9	27.9	29.9	12.0	11.6	8.3	3.3	27.5	30.8

Table 22: Linear shrinkage for samples fabricated (after final method, section 3.6) for compressive strength testing; BA = Bornyl acetate, DMC = Dimethyl carbonate, Xyl = p-Xylene, Cam = Camphene, c = Cured, t = Thermally post-cured, p = Pyrolyzed

Sample	Solvent	Diameter (mm)			Linear shrinkage (%)			Height (mm)			Linear shrinkage (%)		
		c	t	p	c->t	t->p	Total	c	t	p	c->t	t->p	Total
099_BA_25	BA	15.4	15.1	10.7	1.9	28.6	30.5	12.4	12.2	8.4	1.6	30.6	32.3
100_BA_25	BA	15.4	15.1	10.7	1.9	28.6	30.5	13	12.5	9	3.8	26.9	30.8
101_BA_25	BA	15.4	15.1	10.8	1.9	27.9	29.9	12.2	11.7	8.2	4.1	28.7	32.8
103_BA_25	BA	15.3	15.2	10.8	0.7	28.8	29.4	12.6	12.1	8.6	4.0	27.8	31.7
104_BA_25	BA	15.6	15.2	10.7	2.6	28.8	31.4	12.2	12	8.4	1.6	29.5	31.1
113_DMC_25	DMC	16.3	15.7	11.4	3.7	26.4	30.1	13.1	12.7	9.2	3.1	26.7	29.8
114_DMC_25	DMC	16.2	15.8	11.5	2.5	26.5	29.0	13.3	12.9	9.4	3.0	26.3	29.3
116_DMC_25	DMC	16.2	15.8	11.6	2.5	25.9	28.4	11.6	11.4	8.4	1.7	25.9	27.6
117_Xyl_25	Xyl	16.3	15.9	11.4	2.5	27.6	30.1	13.5	13.2	9.4	2.2	28.1	30.4
118_Xyl_25	Xyl	16.9	15.9	11.3	5.9	27.2	33.1	14.4	13.8	9.7	4.2	28.5	32.6
119_Xyl_25	Xyl	16.8	16.2	11.6	3.6	27.4	31.0	14.2	13.6	9.8	4.2	26.8	31.0
123_Cam_25	Cam	14.4	13.8	9.6	4.2	29.2	33.3	11	10.8	7.5	1.8	30.0	31.8
124_Cam_25	Cam	15.1	14.5	10.1	4.0	29.1	33.1	12	11.7	8.1	2.5	30.0	32.5
125_Cam_25	Cam	14.2	14.1	9.5	0.7	32.4	33.1	9.8	9.6	6.7	2.0	29.6	31.6
126_Cam_25	Cam	14.3	14.1	9.9	1.4	29.4	30.8	10.4	10.3	7.2	1.0	29.8	30.8

Table 23: Mean values for the linear shrinkage of samples fabricated (after final method, section 3.6) for compressive strength testing; BA = Bornyl acetate, DMC = Dimethyl carbonate, Xyl = p-Xylene, Cam = Camphene, c = Cured, t = Thermally post-cured, p = Pyrolyzed

Solvent	Number of samples	Linear shrinkage (%)					
		Diameter			Height		
		c->t	t->p	Total	c->t	t->p	Total
Bornyl acetate	4	1.8 ± 0.7	28.5 ± 0.4	30.3 ± 0.8	3.0 ± 1.3	28.7 ± 1.5	31.7 ± 0.8
Dimethyl carbonate	3	2.9 ± 0.7	26.3 ± 0.3	29.2 ± 0.8	2.6 ± 0.8	26.3 ± 0.4	28.9 ± 1.2
p-Xylene	3	4.0 ± 1.8	27.4 ± 0.2	31.4 ± 1.6	3.5 ± 1.1	27.8 ± 0.9	31.3 ± 1.2
Camphene	5	2.6 ± 1.8	30.0 ± 1.6	32.6 ± 1.2	1.8 ± 0.6	29.8 ± 0.2	31.7 ± 0.7

4.9 Density and porosity

Bulk density, apparent solid density and apparent porosity, as determined by the immersion method, are shown in Table 24 for samples produced with different solvents and methods. The PSZ/TT loading was always 25 %, nevertheless the values are quite different. Comparing the apparent porosity for the samples produced without Si_3N_4, it is highest for p-Xylene with 73.4 %. Dimethyl carbonate follows with 68.9 %, then bornyl acetate with 64.1 % and lastly camphene with 53.7 %. When nucleating agent was added, the trend stays the same.
Table 25 shows bulk density, apparent solid density and apparent porosity for bornyl acetate samples with different loading and Si_3N_4 content. Apparent solid density should stay constant for all the samples, which is why a mean value of 2.072 ± 0.018 g/cm³ was calculated. Relative standard deviation was 0.9 %.

Figure 40 displays the data for the bulk density and apparent porosity plotted against the PSZ/TT loading. An almost linear decrease of apparent porosity can be seen with increasing loading. An almost linear increase of bulk density with loading is on view, acting the opposite way. The Si_3N_4 makes only a small difference. There is no statement on statistical significance possible since only one sample was fabricated for each loading.

Despite having the same PSZ/TT loading of 25 wt%, the results of bulk density and apparent porosity are quite different, as seen in Table 26 , depending on the solvent used for the sample fabrication. p-Xylene show the highest and lowest values for apparent porosity and bulk density, respectively. Dimethyl carbonate comes second, followed by bornyl acetate and camphene. The high standard deviations for the porosity and density values for camphene are quite striking. They stem from difficulties during sample fabrication of camphene with the final method (section 3.6). Insufficient polymerization caused varying deformation of the samples during sublimation.

Table 24: Bulk density, apparent solid density and apparent porosity for samples produced with different solvents (Cam = Camphene, Xyl = p-Xylene, DMC = Dimethyl carbonate, BA = Bornyl acetate); samples 071, 075, 078, 084 were produced in the first measurement series described in section 3.5; yellow marked samples 111, 109, 110 were produced using the final method (section 3.6) with 0.1 wt% Si_3N_4 as nucleating agent

Sample	Solvent	Si_3N_4 as nucleating agent	Bulk density (g/cm³)	Apparent solid density (g/cm³)	Apparent porosity (%)
071_Cam_25	Camphene	NO	0.930	2.009	53.7
075_Xyl_25	p-Xylene	NO	0.545	2.046	73.4
111_Xyl_25	p-Xylene	YES	0.558	2.065	73.0
078_DMC_25	Dimethyl carbonate	NO	0.662	2.127	68.9
109_DMC_25	Dimethyl carbonate	YES	0.687	2.080	67.0
084_BA_25	Bornyl acetate	NO	0.753	2.099	64.1
110_BA_25	Bornyl acetate	YES	0.740	2.084	64.5

Table 25: Bulk density, apparent solid density and apparent porosity for bornyl acetate samples with different loading and Si_3N_4 content; yellow marked samples had 0.012 g Si_3N_4 included in the ansatz, the others did not

Sample name	PSZ/TT loading (wt%)	Si_3N_4 as nucleating agent	Bulk density (g/cm³)	Apparent solid density (g/cm³)	Apparent porosity (%)
107_BA_15	15	YES	0.459	2.073	77.8
108_BA_15	15	NO	0.466	2.043	77.2
105_BA_20	20	YES	0.608	2.034	70.1
106_BA_20	20	NO	0.630	2.061	69.4
102_BA_25	25	YES	0.716	2.077	65.5
084_BA_25	25	NO	0.753	2.099	64.1
093_BA_30	30	YES	0.917	2.077	55.8
094_BA_30	30	NO	0.931	2.079	55.2
095_BA_35	35	YES	1.027	2.073	50.4
096_BA_35	35	NO	1.090	2.076	47.5
097_BA_40	40	YES	1.204	2.089	42.4
098_BA_40	40	NO	1.261	2.085	39.5

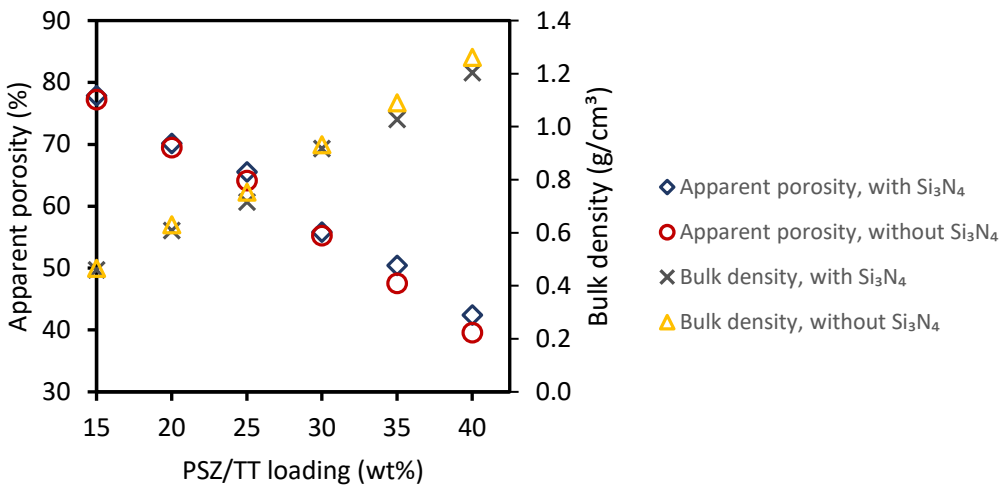

Figure 40: Influence of PSZ/TT loading of bornyl acetate samples on apparent porosity & bulk density

Table 26: Bulk density, apparent solid density and apparent porosity for samples fabricated (after final method, section 3.6) for compressive strength testing

Solvent	Sample	Bulk density (g/cm³)		Apparent solid density (g/cm³)		Apparent porosity (%)	
Bornyl atetate	099_BA_25	0.739	0.744 ± 0.007	2.053	2.075 ± 0.015	64.0	64.1 ± 0.4
	100_BA_25	0.747		2.067		63.9	
	101_BA_25	0.749		2.080		64.0	
	103_BA_25	0.735		2.088		64.8	
	104_BA_25	0.752		2.087		64.0	
Dimethyl carbo-nate	113_DMC_25	0.665	0.666 ± 0.003	2.062	2.067 ± 0.012	67.7	67.8 ± 0.2
	114_DMC_25	0.666		2.081		68.0	
	116_DMC_25	0.666		2.058		67.7	
p-Xylene	117_Xyl_25	0.568	0.566 ± 0.004	2.070	2.065 ± 0.005	72.6	72.6 ± 0.1
	118_Xyl_25	0.568		2.064		72.5	
	119_Xyl_25	0.562		2.061		72.7	
Camphene	123_Cam_25	1.051	1.118 ± 0.188	1.945	1.953 ± 0.054	46.0	42.5 ± 10.9
	124_Cam_25	0.884		2.028		56.4	
	125_Cam_25	1.288		1.939		33.6	
	126_Cam_25	1.251		1.900		34.2	

4.10 Permeability

Depending on the type of solvent, the PSZ/TT loading, and the addition of Si_3N_4 as nucleating agent, the permeabilities differ to an extent of several orders of magnitude. The following Figure 41 shows the permeating flow rising almost linearly with increasing pressure drop. The pictured bornyl acetate sample 110_BA_25 has been taken as an example. The diagrams for all measured samples can be found in the Appendix.

The difference in permeabilities using varying solvents is shown in Table 27. Camphene has by far the lowest permeability values with the Darcian k_1 being $2.56 \cdot 10^{-13}$ m² and the Non-Darcian k_2 being $2.21 \cdot 10^{-08}$ m. The addition of Si_3N_4 changes the values to some extent, comparing the same solvent with and without it. Differences stay below one order of magnitude though. Differences even stay at or below one order of magnitude, when different solvents are compared. Camphene, in this case, must be left out of the comparison.

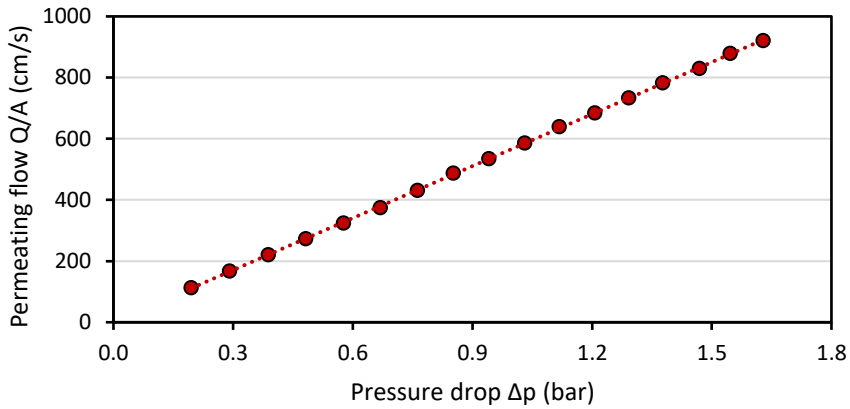

Figure 41: Permeating flow plotted against the pressure drop for the sample 110_BA_25 with bornyl acetate as a solvent and 0.1 wt% Si_3N_4 as a nucleating agent

Table 27: Permeability for samples produced with different solvents; samples 075, 078, 084 were produced in the first measurement series described in section 3.5; yellow marked samples 124, 111, 109, 110 were produced using the final method (section 3.6) with 0.1 wt% Si_3N_4 as nucleating agent, no Si_3N_4 was used for 124_Cam_25

Sample	Solvent	Si_3N_4 as nucleating agent	Permeability	
			Darcian k_1 (m²)	Non-Darcian k_2 (m)
124_Cam_25	Camphene	NO	$2.56 \cdot 10^{-13}$	$2.21 \cdot 10^{-08}$
075_Xyl_25	p-Xylene	NO	$1.17 \cdot 10^{-10}$	$1.11 \cdot 10^{-05}$
111_Xyl_25	p-Xylene	YES	$5.44 \cdot 10^{-11}$	$1.52 \cdot 10^{-05}$
078_DMC_25	Dimethyl carbonate	NO	$2.47 \cdot 10^{-11}$	$8.35 \cdot 10^{-06}$
109_DMC_25	Dimethyl carbonate	YES	$1.52 \cdot 10^{-11}$	$3.62 \cdot 10^{-05}$
084_BA_25	Bornyl acetate	NO	$1.00 \cdot 10^{-11}$	$1.63 \cdot 10^{-05}$
110_BA_25	Bornyl acetate	YES	$8.22 \cdot 10^{-12}$	$8.00 \cdot 10^{-06}$

The highest Darcian permeability is reached by p-Xylene, without any nucleating agent, and a value of $k_1 = 1.17 \cdot 10^{-10}$ m². The highest Non-Darcian permeability is reached by Dimethyl carbonate, with nucleating agent, and a value of $k_2 = 3.62 \cdot 10^{-05}$ m.

Table 28 shows the Darcian (k_1) and Non-Darcian (k_2) permeabilities for bornyl acetate samples with different loading and Si_3N_4 content. Every sample, that was freeze-cast with Si_3N_4, has lower Darcian and Non-Darcian permeabilities than its counterpart of the same loading without the nucleating agent inside. A trend towards lower permeabilities with increasing loading can be seen.

Table 28: Darcian (k_1) and Non-Darcian (k_2) permeabilities for bornyl acetate samples with different loading and Si_3N_4 content; yellow marked samples had 0.012 g Si_3N_4 included in the ansatz, the others did not

Sample	PSZ/TT loading (wt%)	Si_3N_4 as nucleating agent	Permeability	
			Darcian k_1 (m²)	Non-Darcian k_2 (m)
107_BA_15	15	YES	$2.20 \cdot 10^{-11}$	$1.17 \cdot 10^{-5}$
108_BA_15	15	NO	$2.91 \cdot 10^{-11}$	$2.82 \cdot 10^{-5}$
105_BA_20	20	YES	$1.16 \cdot 10^{-11}$	$1.01 \cdot 10^{-5}$
106_BA_20	20	NO	$2.85 \cdot 10^{-11}$	$1.08 \cdot 10^{-5}$
102_BA_25	25	YES	$8.64 \cdot 10^{-12}$	$1.08 \cdot 10^{-5}$
084_BA_25	25	NO	$1.00 \cdot 10^{-11}$	$1.63 \cdot 10^{-5}$
093_BA_30	30	YES	$2.83 \cdot 10^{-12}$	$4.65 \cdot 10^{-6}$
094_BA_30	30	NO	$6.79 \cdot 10^{-12}$	$4.42 \cdot 10^{-6}$
095_BA_35	35	YES	$1.65 \cdot 10^{-12}$	$9.55 \cdot 10^{-7}$
096_BA_35	35	NO	$3.95 \cdot 10^{-12}$	$2.37 \cdot 10^{-6}$
097_BA_40	40	YES	$9.16 \cdot 10^{-13}$	$1.10 \cdot 10^{-6}$
098_BA_40	40	NO	$1.86 \cdot 10^{-12}$	$7.38 \cdot 10^{-7}$

4.11 Compressive strength

The results for the compressive strength of the samples, which were destroyed during measurement, are listed in Table 29. Mean values, as well as standard deviations, were calculated for the solvents. Results are listed in Table 30. p-Xylene shows the lowest value for compressive strength with 0.69 MPa. During the measurement it seemed like the crystals were slipping against each other. They were not orientated parallel to the axis of applied pressure, which has to do with how the p-xylene crystallizes during freeze casting. The crystals partly slid along the crystal growth direction. Dimethyl carbonate is on third place in terms of compressive strength with 3.21 MPa. The relative standard deviation is quite high with 20 % of the total value. Bornyl acetate has a compressive strength of 8.23 MPa, which makes it second highest of the four, and a relative standard deviation of 7.8 %. Camphene shows the highest value for the compressive strength (50.76 MPa), but also the highest relative standard deviation with 34.5 %.
For the purpose of better visualization, the compressive strength samples, fabricated with the four different solvents is pictured in Figure 42. Though having the lowest compressive strength, the relative standard deviation for p-Xylene is also lowest with 1.8 %.

Table 29: Compressive strength test results

Sample	Diameter (mm)	Height (mm)	Force F (N)	Compressive strength σ (MPa)
099_BA_25	10.65	7.73	799	8.97
100_BA_25	10.65	8.16	751	8.43
101_BA_25	10.63	7.79	762	8.59
103_BA_25	10.52	8.12	642	7.39
104_BA_25	10.53	7.90	676	7.76
117_Xyl_25	11.19	8.80	67	0.68
118_Xyl_25	11.14	9.57	68	0.70
119_Xyl_25	11.37	9.58	69	0.68
113_DMC_25	11.30	8.31	373	3.72
114_DMC_25	11.46	8.71	355	3.44
116_DMC_25	11.44	7.84	254	2.47
123_Cam_25	9.66	7.12	2365	32.27
124_Cam_25	10.01	7.6	4447	56.51
125_Cam_25	8.93	6.34	4534	72.39
126_Cam_25	8.81	6.91	2552	41.86

Table 30: Mean values for the compressive strength

Solvent	Compressive strength σ (MPa)	Relative standard deviation (%)
p-Xylene	0.69 ± 0.01	1.8
Dimethyl carbonate	3.21 ± 0.66	20.5
Bornyl acetate	8.23 ± 0.64	7.8
Camphene	50.76 ± 17.53	34.5

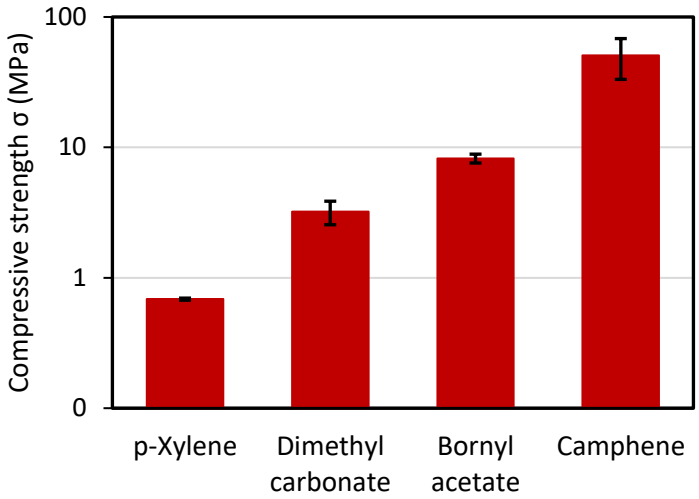

Figure 42: Compressive strength for the samples generated with p-Xylene, dimethyl carbonate, bornyl acetate and camphene

4.12 Hg-Porosimetry

The results for the Hg-Porosimetry measurements are shown in Table 31 & Table 32. The porosity by skeleton density and inaccessible porosity value are affected by the skeleton density, which was set to be 2.4 g/cm³ [86]. The inaccessible porosity shows a negative value with -0.76 % for the sample 107_BA_15, which is theoretically impossible. This leads to the question, how reliable the other values for inaccessible porosity and porosity by skeleton density are, since they depend on a correct value for the skeleton density.

Figure 43 & Figure 44 show two exemplary pore opening size distributions of bornyl acetate samples, freeze cast with a PSZ/TT loading of 25 wt%, one with 0.2 wt% Si_3N_4 and one without nucleating agent. The pore opening size distributions for the other samples can be found in the Appendix. The presence of a nucleating agent shrinks the pore size and therefore shifts the distribution to lower values.

Table 31: Different porosity values obtained by Hg-Porosimetry measurements

Sample	PSZ/TT loading (wt%)	Si_3N_4 (wt%)	Porosity by skeleton density (%)	Porosity by Hg intrusion (%)	Inaccessible porosity (%)
071_Cam_25	25	0	62.3	53.3	9.0
084_BA_25	25	0	66.0	65.2	0.8
109_DMC_25	25	0.1	71.9	65.7	6.2
110_BA_25	25	0.1	68.4	67.0	1.4
111_Xyl_25	25	0.1	74.4	65.8	8.6
107_BA_15	15	0.2	79.7	80.5	-0.8
102_BA_25	25	0.2	70.3	65.0	5.3
095_BA_35	35	0.2	57.6	50.4	7.2

Table 32: Different pore opening diameter values obtained by Hg-Porosimetry measurements

Sample	PSZ/TT loading (wt%)	Si_3N_4 (wt%)	Average pore opening diameter (µm)	Median pore opening diameter (µm)	Modal pore opening diameter (µm)
071_Cam_25	25	0	0.4	6.9	9.2
084_BA_25	25	0	9.6	43.8	68.9
109_DMC_25	25	0.1	2.5	40.6	48.8
110_BA_25	25	0.1	9.5	25.8	35.3
111_Xyl_25	25	0.1	1.1	72.1	84.8
107_BA_15	15	0.2	12.5	39.1	47.8
102_BA_25	25	0.2	2.0	26.6	33.1
095_BA_35	35	0.2	2.2	13.0	14.6

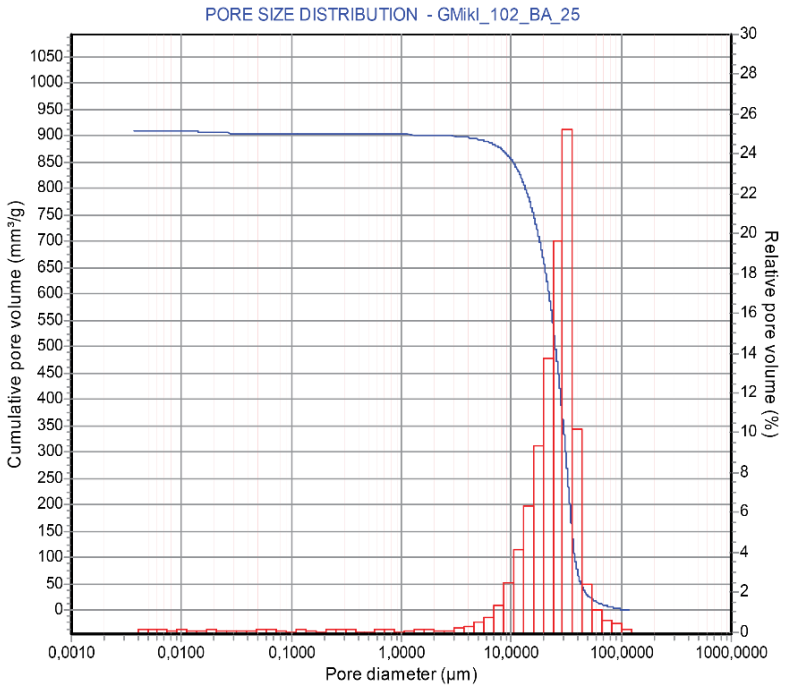

Figure 43: Pore opening size distribution of 102_BA_25, a bornyl acetate sample with a PSZ/TT loading of 25 wt% and 0.2 wt% Si_3N_4

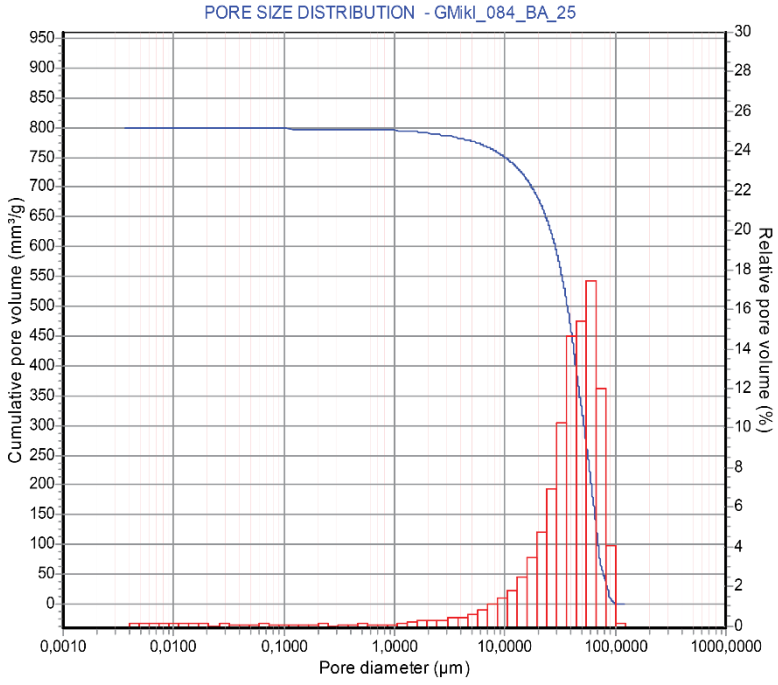

Figure 44: Pore opening size distribution of 084_BA_25, a bornyl acetate sample with a PSZ/TT loading of 25 wt% and no nucleating agent

4.13 Differential photocalorimetry measurements

Figure 45 shows the DSC curves which were recorded during the measurements. Each mixture was measured three times for reproducibility purposes. There is some variation between each run but not to an extent which would be problematic for the actual curing process. The energy released during the photopolymerization corresponds to the integral of the DSC curves. When looking at the curves, one can easily see that more than 50 % of the photopolymerization reaction is finished after no longer than 20 s. This is despite the low temperature of -10 °C and valid for all four solvents. As the actual curing temperature during the experiments was primarily in the range of -30 °C to -15 °C, an investigation of the polymerization behaviour at temperatures below room temperature was necessary for better comparison.

Table 33 shows several parameters, which can be calculated from the recorded DSC curves. t_{95} represents the time where 95 % of the reaction is finished. To get this value, one must calculate after which time the integral amounts to 95 % of the total integral. t_{max} represents the time where the reaction rate is at its peak. It can easily be read off the chart by taking the time at the maximum of the curve. Peak height is equal to the maximum of the curve, corresponding to the value of the maximum specific heat flow. Peak area is equivalent to the integral of the DSC curve and represents the energy which is released during the photopolymerization.

Table 33: Different parameters calculated from the measured DSC-curves, obtained from mixtures containing one of the listed solvents

	Experiment number	Camphene	Dimethyl carbonate	p-Xylene	Bornyl acetate
t_{95} (s)	Run 1	117.2	50.1	45.8	23.3
	Run 2	129.6	48.5	48.5	32.0
	Run 3	73.8	63.5	47.9	9.1
	Mean	106.9 ± 29.3	54.0 ± 8.2	47.4 ± 1.4	21.5 ± 11.6
t_{max} (s)	Run 1	1.4	1.8	2.2	1.6
	Run 2	1.8	2.0	2.2	2.0
	Run 3	1.6	1.7	1.6	1.6
	Mean	1.6 ± 0.2	1.8 ± 0.2	2.0 ± 0.3	1.7 ± 0.2
Peak height (mW/mg)	Run 1	2.93	4.99	5.43	7.30
	Run 2	2.78	4.70	4.87	5.30
	Run 3	3.29	5.73	7.28	6.90
	Mean	3.00 ± 0.26	5.14 ± 0.53	5.86 ± 1.26	6.50 ± 1.06
Peak area (J/g)	Run 1	22.15	56.74	53.22	40.88
	Run 2	24.34	59.71	56.28	41.09
	Run 3	21.18	46.90	57.93	37.50
	Mean	22.56 ± 1.62	54.45 ± 6.71	55.81 ± 2.39	39.82 ± 2.01

t_{max} is comparable for all four solvents with values ranging from 1.6 s to 2.0 s. The reaction starts quite fast, considering the temperature of -10 °C. t_{95} states that camphene takes the longest for reaching the 95 % level with 106.9 s. It is followed by dimethyl carbonate (54.0 s), p-Xylene (47.4 s) and Bornyl

acetate (21.5 s). Bornyl acetate reacts fastest and shows the largest value for peak height as well with 6.50 mW/mg. Peak height decreases in reverse order with 5.86 mW/mg for p-Xylene, 5.14 mW/mg for dimethyl carbonate and 3.00 mW/mg for camphene.

Peak area, representing the released energy, shows a different picture with p-Xylene having the largest value of 55.81 mW/mg, followed by dimethyl carbonate with 54.45 mW/mg, bornyl acetate with 39.82 mW/mg and camphene with 22.56 mW/mg. Judging by these values, camphene performs worst in every category except for t_{max}, where it is best.

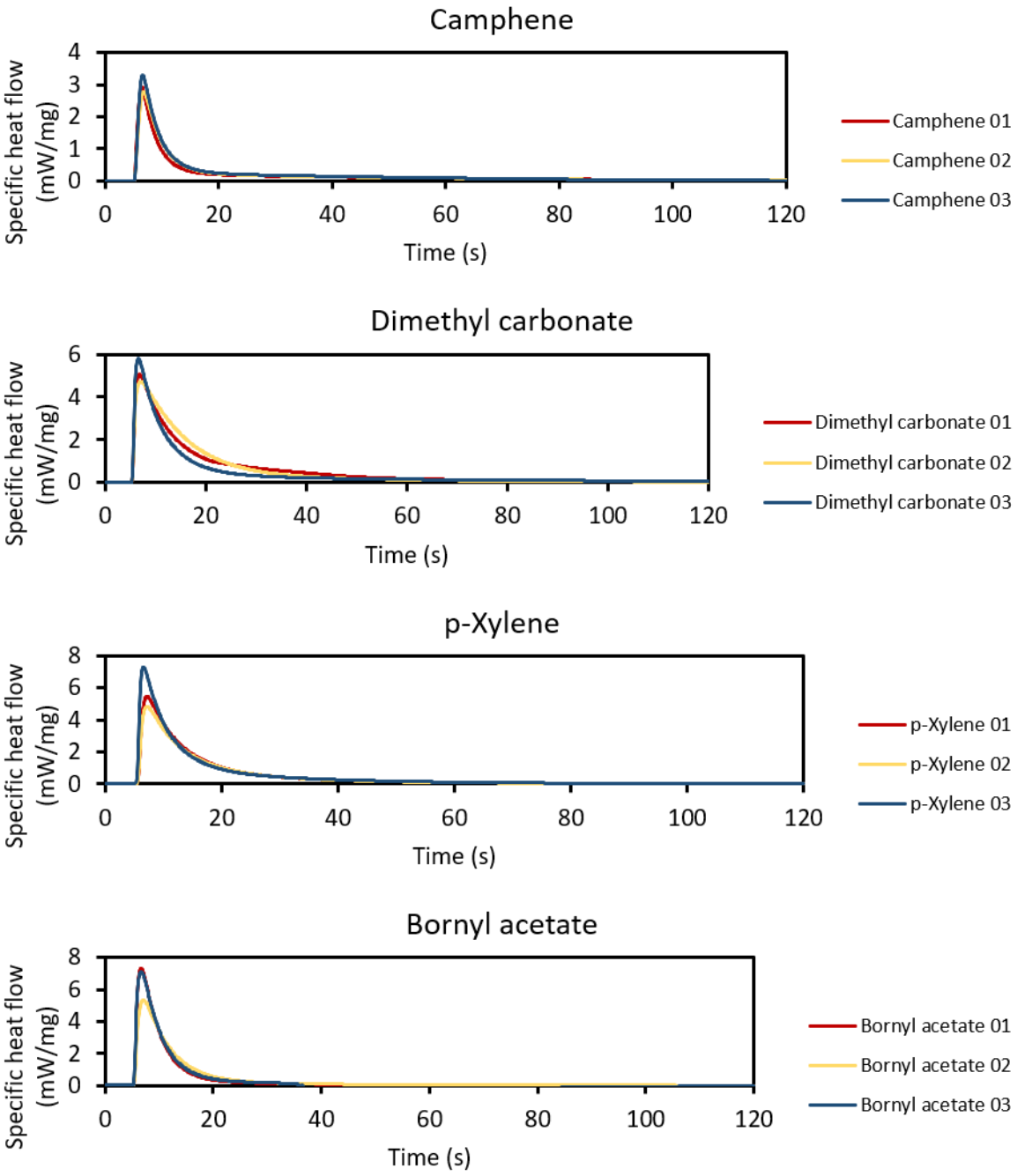

Figure 45: Photo-DSC-curves for the four examined mixtures. Measurements were performed at a wavelength of 400 nm and -10 °C. Irradiation started after 5 s. Each mixture had a PSZ/TT loading of 25 wt% and was measured three times with respect to reproducibility.

4.14 Solvent enthalpies of fusion & melting points

Figure 46 shows the resulting DSC curve for bornyl acetate with the first ramp. There are no relevant peaks visible and only small deflections from the base line, presumably from impurities or other inhomogeneities during measurement, can be seen. There is no obvious melting peak visible.

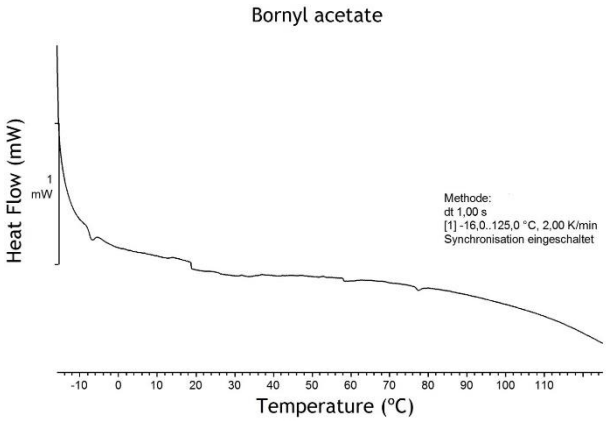

Figure 46: DSC-measurement for bornyl acetate with a ramp from -16 °C to 125 °C, starting at the low temperature, and a heating rate of 2 K/min. No relevant peaks from endothermic or exothermic events are visible.

Figure 47 shows the results for the DSC-measurement of the solvents camphene, p-xylene, dimethyl carbonate and bornyl acetate. In each of the four measurements a melting peak could be identified. The negative heat flow for camphene from -16 °C to approximately 0 °C is possibly related to the instrument and the heat capacity of the sample. This part provides no information. The peak at about 80 °C could be related to some endothermic decomposition. When looking at dimethyl carbonate, one can identify a small shoulder on the melting peak. This is most likely related to some sort of impurity in the sample and moves the onset point slightly. The peak at about 80 °C could be related to an endothermic decomposition. It could also be caused by the instrument, because the similarity to camphene is quite noticeable. p-Xylene shows a very sharp melting peak, which is due to the high purity of the sample.

The bornyl acetate curve, measured with the second ramp, contains a few features. A small endothermic peak is visible at the onset point of -77.7 °C. A small impurity could have caused this deflection. An exothermic peak can be seen between -70 °C and -60 °C. It is most possibly caused by the energy released from crystallization of the bornyl acetate. This proves that starting with a ramp at considerably lower temperatures (-80 °C instead of -16 °C) than in the first run solved the problem of supercooling. The big melting peak ranging from around 0 – 20 °C also contains a smaller peak at 6.85 °C. A metastable modification could be melting here. Since the purity of the bornyl acetate was 95 %, it is no surprise that the melting peak is broader and has been moved to 18.6 °C instead of 27 °C, which is reported in the literature [82].

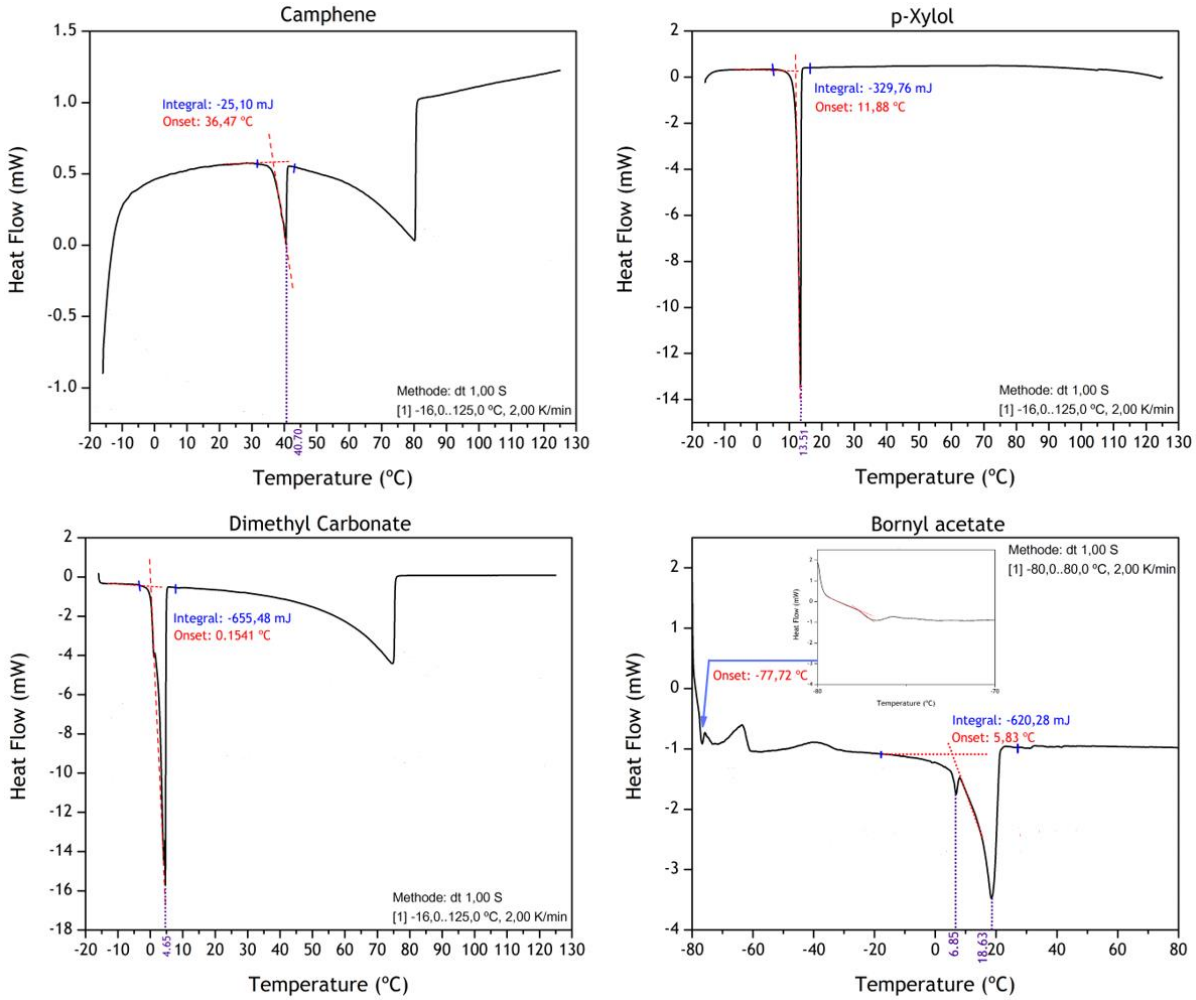

Figure 47: DSC-measurement for the solvents camphene, p-xylene, dimethyl carbonate and bornyl acetate. Heating rate was always 2 K/min. The onset marks the start of the melting peak, Integral shows the necessary enthalpy to melt the sample.

The following Table 34 shows the weighed-out mass, the melting point, the integral under the melting peak as well as the resulting enthalpy of fusion. The very low value for the enthalpy of fusion of camphene seems suspicious. It is possible, that a preparation error, a measurement error or impurities led to the value of 0.44 kJ/mol. The melting points for dimethyl carbonate and p-xylene show good accordance with literature, because they differ less than 0.5 °C. The measured melting point for camphene with 40.7 °C is 10 °C lower than the literature value, which is quite a difference. Bornyl acetate shows a difference of 8.4 °C between measured and literature value.
The enthalpies of fusion show large deviations from literature. Camphene is the most extreme example with a measured value of 0.44 kJ/mol and a literature value of 9.44 kJ/mol. Bornyl acetate is the solvent, for which the values coincide at least to some degree with 15.22 kJ/mol measured and 13.34 kJ/mol literature values.

Table 35 shows the entropic terms of the Jackson α-factor for measured and literature values. The difference between measurement and literature is quite striking, especially for camphene. It has the lowest entropic term of all solvents in the measurements, like it does in the literature. Bornyl acetate shows the least deviation from literature with 6.27 against 5.35.

Table 34: Weighed-out mass, integral, melting point & enthalpy of fusion of the solvents for the DSC measurement (experimental procedure in section 3.8.8); Meas.: measured value, Lit.: literature value

Substance	Sample mass	Integral	Melting point T_m		Enthalpy of fusion L	
			Meas.	Lit.	Meas.	Lit.
Camphene	7.7 mg	-25.1 mJ	40.7 °C	51 °C [87]	0.44 kJ/mol	9.44 kJ/mol [88]
Dimethyl carbonate	8.7 mg	-655.5 mJ	4.7 °C	5.1 °C [89]	6.79 kJ/mol	11.58 kJ/mol [89]
p-xylene	4.0 mg	-329.8 mJ	13.5 °C	13.2 °C [90]	8.75 kJ/mol	17.11 kJ/mol [90]
Bornyl acetate	8.0 mg	-620.3 mJ	18.6 °C	27 °C [82]	15.22 kJ/mol	13.34 kJ/mol [91]

Table 35: Entropic terms (L/RT_m) of the Jackson α-factor for measured (Meas.) and literature (Lit.) values

Solvent	L/RT_m	
	Meas.	Lit.
Camphene	0.17	3.50
Dimethyl carbonate	2.94	5.01
p-Xylene	3.67	7.19
Bornyl acetate	6.27	5.35

5 Discussion

5.1 Supercooling

Supercooling was an issue for p-xylene, which has also been reported in the literature [2], dimethyl carbonate and bornyl acetate. Casting solutions with camphene seemed to form a microemulsion. This provided an enormous amount of intrinsic nucleation seeds and therefore supercooling was not visible for camphene. Elimination of supercooling and structural refining were tackled with the help of nucleating agents. SiC, Si_3N_4, UHMW-PE and a roughened aluminium surface acted as such. For p-xylene and dimethyl carbonate, no relevant effect of the nucleating agents could be seen. It was easy to elude this problem by just cutting off the bottom part of the sample, which had been frozen almost instantly. The supercooling in bornyl acetate was catastrophic with solutions sometimes reaching -60 °C without any freezing. The only way to prevent this effect was to freeze a little bornyl acetate layer onto the casting plate prior to pouring in the casting solution. The solvent itself provided an excellent nucleation help.

5.2 Solvent influence on microstructure and properties

The influence of the solvent as a structuring agent on pore morphology, microstructure and other properties seems to be one of the most influential parameters besides the presence of nucleating agents, judging by the results of the performed experiments. As camphene had already been investigated by Richard Obmann in the research group [4], the focus was kept on three new solvents of interest. Preliminary testing led to the exclusion of several potential other candidates because of insufficient solubility of the PSZ and TT. Camphene, p-Xylene, dimethyl carbonate and bornyl acetate shall be compared in the following section.

The microstructures obtained by freeze casting with different solvents (Figure 25 – Figure 27, Figure 29 – Figure 31) clearly show that the goal of having directional porosity was reached for every solvent. Camphene showed the finest structure, which was probably caused by the fact that tetrathiol is not fully miscible with it. During preparation of the casting solution, it became cloudy from the moment tetrathiol was added. A microemulsion seemed to form, providing lots of finely dispersed nucleation seeds for the solidifying camphene during the freeze casting procedure. The other three solvents p-xylene, dimethyl carbonate and bornyl acetate had much larger pores, and the samples were also more delicate to handle once pyrolyzed. Due to the missing dendrites, which gave the camphene samples strength in both longitudinal and transversal direction, the structure was weaker for the other samples. The transversal plane, perpendicular to the freezing direction, was equipped with only small and fewer ceramic bridges, connecting the larger crystals.

p-Xylene, dimethyl carbonate and bornyl acetate form lamellar structures when no nucleating agent is present. p-Xylene crystallizes in a quite uncontrollable manner. While directionality can still be achieved, it is deviating quite substantially from a vertical growth of the crystal. The orientation of dimethyl carbonate and bornyl acetate seems to be more in line with the direction of the freezing front during freeze casting. Upon addition of a nucleating agent, the structural changes for p-xylene and dimethyl carbonate are barely recognizable (Figure 48 (a)->(b) and (c)->(d)). The small features at the surface of the large platelets in the p-xylene samples partially change their orientation. The previously parallel direction, in relation to the growth direction, switches to mostly perpendicular.

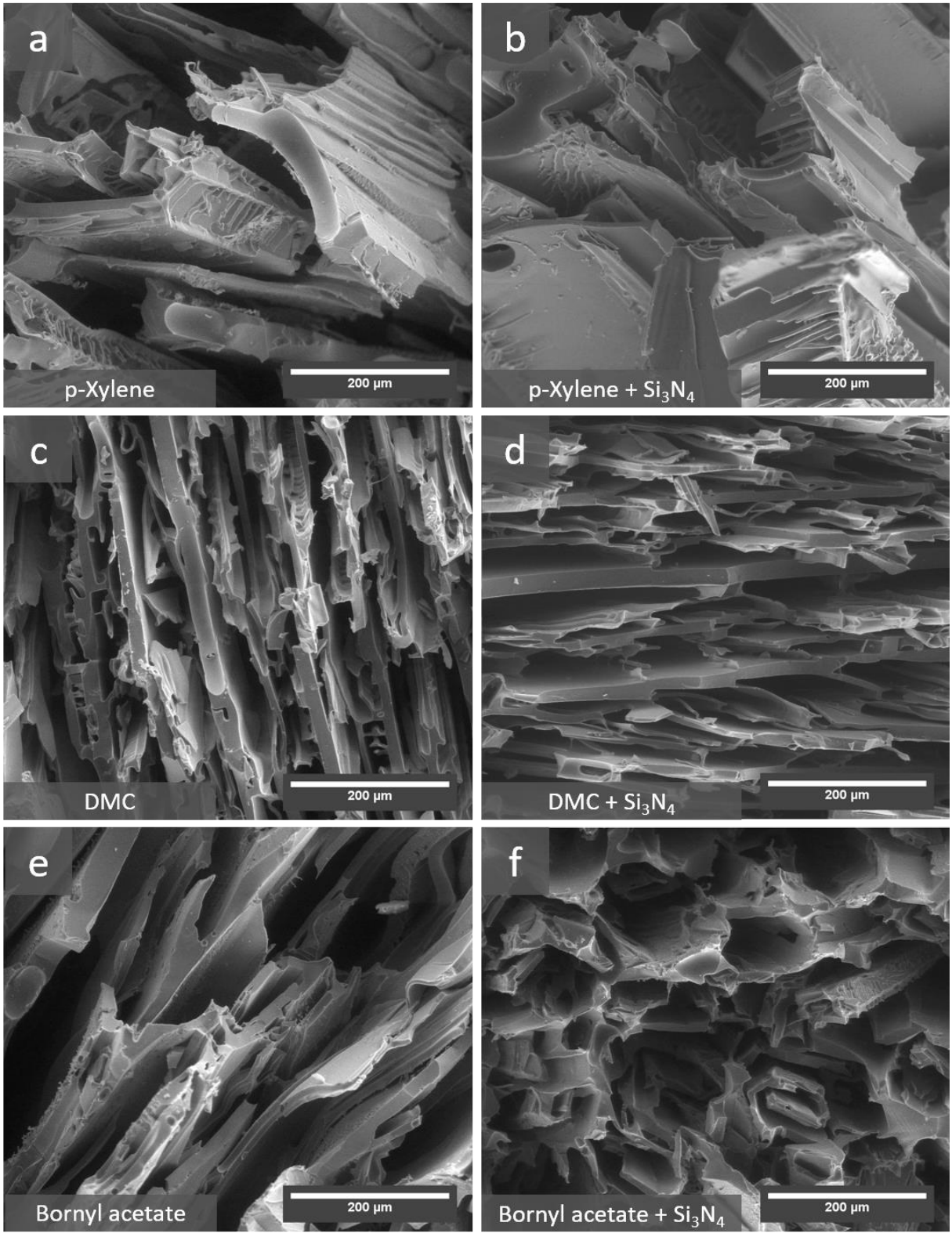

Figure 48: Summary of microstructures obtained by using different solvents, transversal cut (perpendicular to the freezing direction) through the samples, cast with/without nucleating agent, PSZ/TT loading was 25 wt%, left bottom corner states solvent and if nucleating agent was added; (a) 075_Xyl_25 (b) 111_Xyl_25 (c) 078_DMC_25 (d) 109_DMC_25 (e) 084_BA_25 (f) 110_BA_25

Dimethyl carbonate shows some rectangular and spiral-like porosity in some parts of the sample, with most of the pore structure not changing much. In contrast, bornyl acetate alters its pore morphology substantially when Si_3N_4 comes into play. The lamellar structure vanishes and makes way for spiral like pores, some even being almost circular tubes. The microstructure also becomes finer which can not only be seen in the transversal cut, but also in the longitudinal cut. For comparison see Figure 27 (d) and Figure 31 (d).

The total mass loss for the samples produced with different solvents (Table 18 & Table 19) fluctuates between 40.6 – 44.5 %. Samples produced with Si_3N_4 tend to have slightly bigger mass loss than the ones without it. The changing microstructure could be affecting the evaporation of breakdown products during thermal post-curing and pyrolysis. Thermal post-curing produced mass losses from 4.3 % up to 10.4 %. Leftover solvent from the sublimation, eventually trapped in closed pores, may have caused these fluctuations. Pyrolysis resulted in mass loss from 30.7 % up to 37.5 %. The large overall differences could be the result of measurement or experimental errors. Another issue, which cannot be denied, is the solvent itself. Side reactions, especially at higher temperatures, could be explaining the variations.

Linear shrinkage was quite difficult to measure. This was due to the fragility of the samples. Smaller pieces would easily break off during measurement, which may be one of the reasons for the large deviations in total linear shrinkage from 25.9 – 33.3 %. At least, shrinkage for diameter and height of the same samples seemed to coincide to a large extent. The solvent as a cause for the occurring fluctuations cannot be denied. Small remains of structuring agent leaving only at thermal post-curing or pyrolysis could have affected the shrinking process.

Figure 49 shows the porosity obtained by Hg intrusion and the median pore opening diameter of samples, that had been freeze-cast with different solvents but the same PSZ/TT loading of 25 wt%. Apart from camphene, the porosity is remarkably similar, at around 65 % for the other solvents. The lower value of 53.34 % for camphene could have been caused by camphene reacting with the rest of the solution and being partly built into the structure of the final ceramic. Another explanation could be the different crystal growth, which is lamellar-like for p-xylene, bornyl acetate and dimethyl carbonate, whereas camphene grows dendritically. The median pore opening diameter varies much more than the porosity. Camphene possesses the lowest value with 6.9 µm and p-xylene the highest with 72.1 µm. The order in between is dependent on the addition of nucleating agent to the bornyl acetate. Without Si_3N_4, it has the second highest median pore opening diameter of 43.8 µm, with Si_3N_4 it ranks third with a value of 25.8 µm. Dimethyl carbonate possesses a value of 40.6 µm.

Looking at Figure 48 (e + f) again and keeping in mind the just mentioned behaviour for bornyl acetate, the shrinking of the median pore opening diameter upon addition of nucleating agent, measured by Hg-Porosimetry, is in accordance with the observations from the SEM (scanning electron microscope) micrographs. The same conformity of results goes for p-Xylene, which has by far the largest median pore opening diameter. Looking at Figure 48, the microstructure is coarsest for p-xylene.

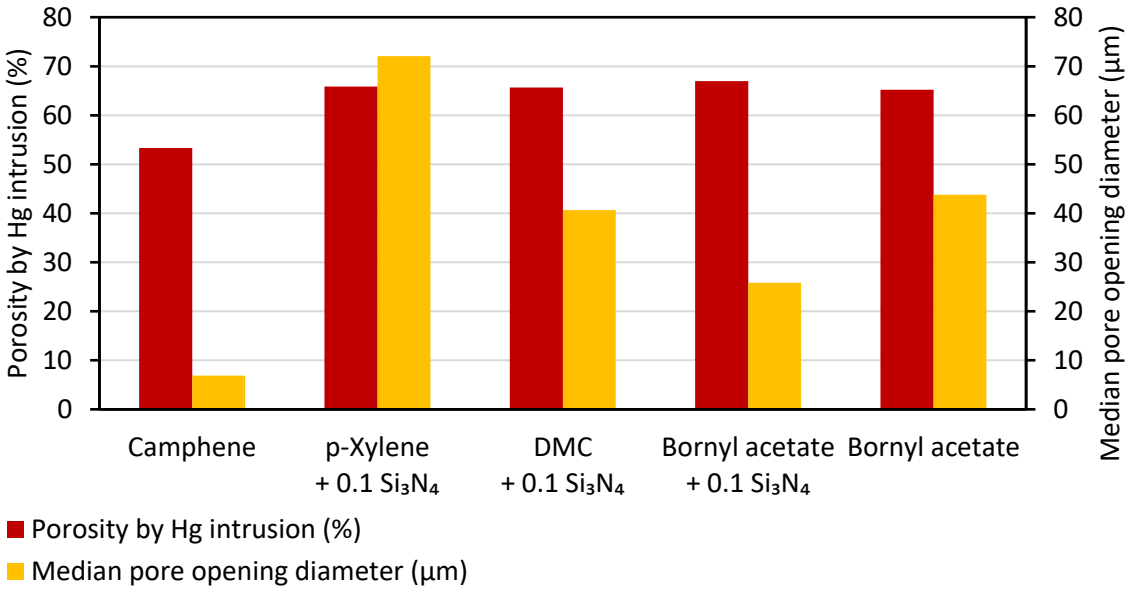

Figure 49: Porosity by Hg intrusion & median pore opening diameter, measured by Hg-Porosimetry; Following samples, all with a PSZ/TT loading of 25 wt%, are displayed: 071_Cam_25, 109_DMC_25, 111_Xyl_25, 110_BA_25 (with 0.1 wt% Si_3N_4), 084_BA_25 (without Si_3N_4)

Properties like the apparent porosity and bulk density were heavily affected by the choice of solvent. Table 24, listing results for different samples but same PSZ/TT loading with and without nucleating agent, gives reason to make such a statement. Bulk density was starting as low as 0.545 g/cm³ for p-xylene and ended at 0.930 g/cm³ for camphene. Apparent porosity showed a similar picture with camphene displaying the lowest value of 53.7 % this time and p-xylene exhibiting the highest one with 73.4 %. The structural changes caused by the solvent directly affected bulk density and apparent porosity. The fluctuations of apparent solid density (Table 24) could be caused by density differences of the solvents. Differences in phase separation behaviour might be another explanation.

The permeability values obtained from varying solvent and Si_3N_4 content span over several orders of magnitude and are displayed in Figure 50. The Non-Darcian permeability fluctuates quite a lot around $1 \cdot 10^{-5}$ m for the solvents p-xylene, dimethyl carbonate and bornyl acetate. No clear influence of the addition of Si_3N_4 on the Non-Darcian permeability can be seen. The value for camphene is by far the smallest with $k_2 = 2.21 \cdot 10^{-8}$ m. The Darcian permeability k_1 ranks highest for p-xylene, followed by dimethyl carbonate, bornyl acetate and camphene in descending order. k_1 gets smaller when nucleating agent is added to the sample. It has been previously shown that the pore size gets smaller for bornyl acetate, when Si_3N_4 is present. No Hg-Porosimetry testing was performed for the other solvents with the addition of Si_3N_4 and no visible refinement of the pore structure can be seen in Figure 48 for p-xylene and dimethyl carbonate. Still it seems that the structure got refined a little, causing the lowering of k_1. It was not possible to cure camphene in the presence of Si_3N_4.

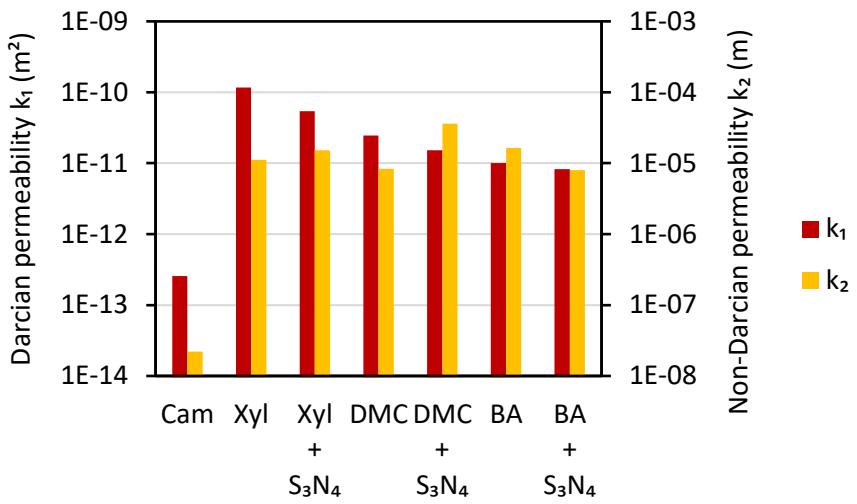

Figure 50: Permeability for different solvents and Si_3N_4 content; Xyl = p-Xylene, DMC = Dimethyl carbonate, BA = Bornyl acetate, Cam = Camphene; following samples are shown in this figure: 075_Xyl_25 (no Si_3N_4), 111_Xyl_25 (with Si_3N_4), 078_DMC_25 (no Si_3N_4), 109_DMC_25 (with Si_3N_4), 084_BA_25 (no Si_3N_4), 110_BA_25 (with Si_3N_4), 124_Cam_25 (no Si_3N_4)

The compressive strength comparison from the results section is depicted again in Figure 51. The importance of connective ceramic bridging between the pores oriented in longitudinal direction (parallel to freezing direction) becomes apparent when looking at the compressive strength. The solvent camphene, yielding the highest compressive strength, also has a higher connectivity in transversal direction than the other structuring agents due to its dendritic growth. Pore size also seems to play an important role for compressive strength. Smaller pores result in stronger ceramics. Bornyl acetate ranks second, thanks to the pore morphology obtained from the addition of the nucleating agent. It also has the second lowest median pore opening diameter (Figure 49). Dimethyl carbonate, having the second-to-lowest median pore opening diameter, ranks third, leaving the p-xylene at the last place. As mentioned previously, the large tilting of the crystal orientation away from the longitudinal sample axis, as well as the coarse structure and the lack of connective ceramic bridging cause the compressive strength to plummet.

The results of the photocalorimetry measurements (Figure 45 & Table 33) show that each of the solvents can be cured fast and effectively. The following facts make this apparent: The maximal reaction rate was always reached between 1.6 s to 2.0 s, 95 % of the reaction had finished in less than 2 min, and 50 % of the photopolymerization reaction had finished even after only 10 s of irradiation. This was true for the four solvents camphene, p-xylene, dimethyl carbonate and bornyl acetate. Because the facts stated until now do not allow judgement over which one performed best, the peak area was compared. p-Xylene had the largest value, followed by dimethyl carbonate, bornyl acetate and camphene. Thus, camphene seemed to interfere most with the photopolymerization, leading to a smaller energy release from the reaction, represented by the peak area.

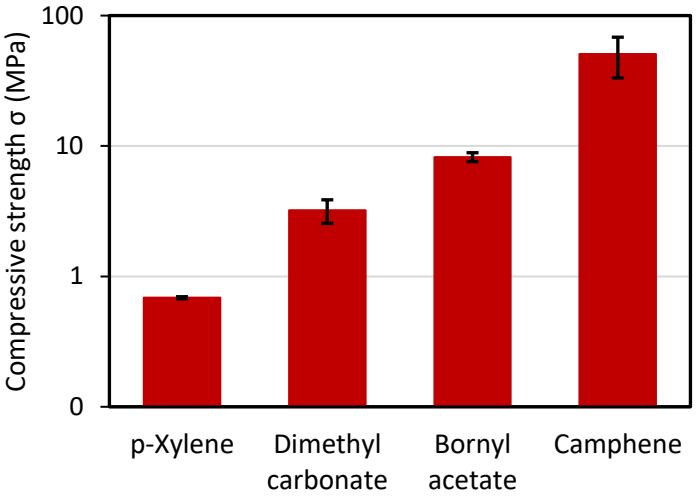

Figure 51: Compressive strength for samples using p-xylene, dimethyl carbonate, bornyl acetate and camphene as structuring agents

Table 36 lists the entropic terms of the Jackson α-factor for the different solvents. Higher values predict more anisotropic and faceted growth of the crystal structure. The entropic terms for dimethyl carbonate, p-xylene and bornyl acetate are higher than for camphene. The directionality of the camphene structure should therefore be lower, which agrees with the other results (Figure 30 & Figure 31). The other solvents have much more pronounced unidirectional pores than camphene. The striking difference between measurement and literature can possibly be explained by measurement errors. The weighed-out mass for the solvent prior to measurement is very small (in the order of 10 mg) and when the vapor pressure is reasonably high, as is the case for all tested solvents, leaving the sample holder open for a little too long will result in drastic deviations for the mass. As the results are mass dependent, the measurement will then be faulty.

Table 36: Entropic terms of the Jackson α-factor for measured (Meas.) and literature (Lit.) values of different solvents

Solvent	L/RT_m	
	Meas.	Lit.
Camphene	0.17	3.50
Dimethyl carbonate	2.94	5.01
p-Xylene	3.67	7.19
Bornyl acetate	6.27	5.35

5.3 Influence of PSZ/TT loading and nucleating agent in bornyl acetate samples

The influence of PSZ/TT loading was investigated with samples where bornyl acetate served as a structuring agent and solvent. As expected, different loadings resulted in enormous changes of several properties of the samples. Samples of 15 – 40 wt% PSZ/TT content were produced. For further discussion it must be born in mind, that the samples with 35 wt% and 40 wt% PSZ/TT, which also contained Si_3N_4, could not be fabricated completely free of cracks.

Looking at the mass loss in Table 17, the percentage of solvent or amount of nucleating agent used in the casting did not seem to influence the total loss of mass. Therefore, a mean value of 42.4 ± 0.7 % for the total loss of mass could be calculated from 12 samples. The loss of mass from cured to thermally post-cured sample with 6.4 ± 1.0 % is considerably smaller than the loss of mass from thermally post-cured to pyrolyzed sample with 36.0 ± 0.8 %. This was to be expected, because the thermal post-curing is performed at a maximal temperature of 200 °C, which is too low to cleave and breakdown most bonds in the structure. The pyrolysis step, going up to 1000 °C, can utilize a much bigger temperature interval to initiate chemical breakdown and evaporation of gaseous organic molecules. The large variations in mass loss for the thermal post-curing step (4.6 – 7.7 %) could be caused by leftover bornyl acetate, which was not removed during sublimation. Maybe some solvent was caught in closed pores, which only opened and released the remaining bornyl acetate after temperature and thus pressure in the pore increased. An insufficient sublimation time could also be taking part in this issue. PSZ/TT ratio was not varied, which probably would have caused a more distinct and possibly statistically relevant difference in loss of mass.

Linear shrinkage also seems to be independent of bornyl acetate or Si_3N_4 content, as no trend could be identified (Table 20). A mean value of total linear shrinkage was therefore calculated for all the 12 samples, which amounted to 30.0 ± 1.1 % for the diameter and 30.8 ± 1.3 % for the sample height. The thermal post-curing step yielded immense variations in linear shrinkage. Two factors quite possibly played a role in causing this, measurement errors and the set-up for freeze drying. The freshly sublimated samples were quite rough on their edges and small parts breaking off would result in dimension changes that cannot be neglected. As the PTFE-foil surrounding the samples for freeze drying was secured with a rubber band, a different size or elasticity of the band could have caused larger pressure and therefore deformation during the procedure.

The apparent solid density (Table 25) showed some variation, but no trend. The calculated mean value amounts to 2.072 ± 0.018 g/cm³. Figure 40 shows the effect of different loading on apparent porosity and bulk density quite clearly. Increasing loading results in an almost linear increase of bulk density. Apparent porosity acts the opposite way with linearly decreasing with increasing loading. The addition 0.2 wt% of Si_3N_4 to half of the samples caused some minor deviations. The quite dramatic structural change could be reason for this difference.

Figure 52 shows the influence of PSZ/TT loading on porosity and median pore opening diameter for bornyl acetate samples. As expected, an increase in loading causes a decrease in porosity and a decrease in pore diameter. When the nucleating agent is missing, the substantial change in the structure is also reflected by the sharp increase of the median pore opening diameter. The value almost doubles from 26.6 µm to 43.8 µm. The porosity seems almost unaffected by the nucleating agent.

Porosity and pore opening diameter can also be compared for bornyl acetate samples with the same PSZ/TT loading of 25 wt%, but a different Si_3N_4 content. Values can be found in Table 31 & Table 32 and are summarised in Table 37. One would expect an increase of nucleating agent resulting in a decrease of the pore opening diameter. The opposite, a slight increase can be witnessed. Due to lack of repetitions it cannot be stated that this difference is statistically relevant. Maybe 0.1 wt% Si_3N_4 is already enough to provide enough nucleation seeds for the system to reach saturation, which does not allow the pore size to get even smaller. An interesting idea not carried out in this thesis would be to lower the Si_3N_4 content until a significant increase of the pore opening diameter can be witnessed. The porosity by Hg intrusion sinks with increasing Si_3N_4 concentration, but only very little and maybe not even with statistical relevance.

The permeability values can be found in Table 28. For a better visualization, the effect of PSZ/TT loading and Si_3N_4 is displayed in Figure 53. Darcian (k_1) and Non-Darcian (k_2) permeabilites sink with increasing loading. This is due to the densification of the samples. Darcian permeability is always lower for samples with Si_3N_4. Non-Darcian (k_2) values suffer from enormous variations, especially for smaller loadings. Since the samples are robust in longitudinal, but fragile in transversal direction (perpendicular to the freezing direction), the permeability measurement itself could have caused these alterations. The application of the shrinking tube and fixation with screw clamps may have damaged the samples without the user noticing it during the measurement. Removal of the sample out of the shrinking tube after measurement always crushed parts of the outside, which is why it was impossible to deduce if any damage had been done prior to measurement.

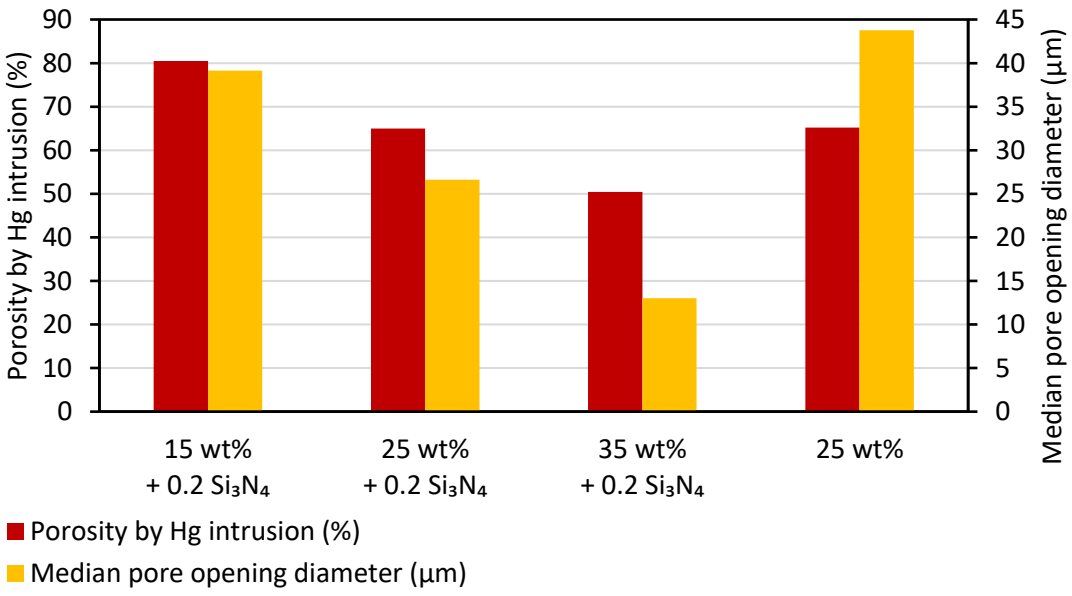

Figure 52: Porosity by Hg intrusion & median pore opening diameter, measured by Hg-Porosimetry; Following bornyl acetate samples, with different PSZ/TT loadings, are displayed: 107_BA_15, 102_BA_25, 095_BA_35, 084_BA_25 (sample without Si_3N_4)

Table 37: Influence of Si_3N_4 content on porosity and pore opening diameter of bornyl acetate samples

Sample	Si_3N_4 (wt%)	Porosity by Hg intrusion (%)	Median pore opening diameter (µm)
110_BA_25	0.1	66.98	25.80
102_BA_25	0.2	64.97	26.63

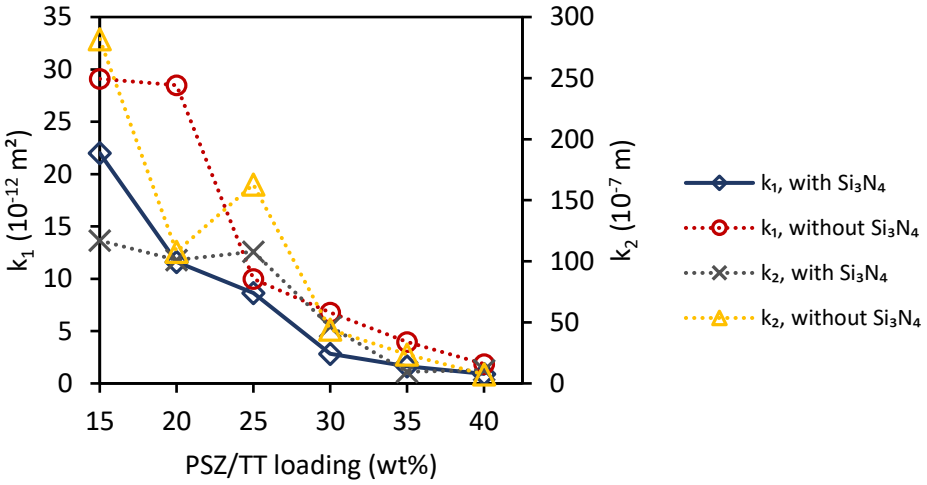

Figure 53: Effect of PSZ/TT loading and Si_3N_4 on Darcian (k_1) and Non-Darcian (K_2) permeabilities of samples fabricated with Bornyl acetate as a solvent

When changing the loading and Si_3N_4 content in bornyl acetate samples (Figure 32 - Figure 39), the biggest visible difference is the change in structure with the addition of the nucleating agent. Spirals and tubes replace the lamellas. The increased loading densifies the structure but does not alter the pore morphology. The densification is shown by an increase in bulk density when looking at higher loadings and visible from comparison of the pictures, which had been taken with the scanning electron microscope. Comparing the two extremes, a loading of 15 wt % and the loading of 40 wt%, the difference becomes obvious. The hole formation, seen in Figure 35 (d), could be caused by gas present in the solvent. Upon freezing of the casting solution, gas release from the casting solution had occurred to some extent. Some of the smaller bubbles were not able to rise fast enough and would get outpaced by the freezing front. The small grooves Figure 35 (a, c, e), which evolved perpendicular to the freezing direction, could be the result of fluctuations in the casting solution during freezing. Temperature and concentration gradients may have caused convection on a microscopic level, leading to this type of morphology. The grooves are hardly visible in samples missing the nucleating agent, seen in Figure 35 (b, d, f). This leads to the conclusion that the Si_3N_4 plays an important role in the formation of said grooves, because the presence of nucleating agent had been the only difference in sample preparation.

6 Summary & Outlook

6.1 Summary

During this thesis macroporous ceramics with unidirectional and open pore channels could be successfully fabricated by using photopolymerization-assisted solidification templating. A method was developed which allows for the control of the pore morphology by using different structuring and nucleating agents in the process.

Starting with a preceramic polymer, a crosslinking agent, a structuring agent also acting as solvent, a photoinitiator and, at times, a nucleating agent, a sample could be obtained by freeze-casting and photocuring the solution. The following sublimation of the solvent would leave the crystal structure of the structuring agent behind as pores. Thermal post-curing at 200 °C and pyrolysis at 1000 °C, both under nitrogen atmosphere, would lead to a black macroporous ceramic. Polyvinylsilazane (PSZ) was used as a preceramic polymer and tetrathiol (TT) was present to work as a cross-linking agent utilizing a thiolene reaction for curing. Two different photoinitiators, camphorquinone and ETPP, were tested. ETPP proved to work a lot faster with the same efficiency as camphorquinone. As ETPP needs 400 nm for initiation, a lamp emitting this wavelength was built.
Cooling rates of 2 K/min and 8 K/min were tested for the freeze-casting step. Since 8 K/min worked faster and provided refined structures, it was set to be a fixed parameter for the final method. Four different structuring agents and their influence on the pore morphology and other parameters were investigated. These were camphene, bornyl acetate, dimethyl carbonate and p-xylene.

Camphene showed no full miscibility with tetrathiol but was used regardless because previous work in the research group by Richard Obmann had led to successful sample fabrication. The camphene grew dendritically which was reflected in the resulting pore structure. Due to its melting point the sample preparation, including mixing and addition of chemicals, had to be performed at 55 °C. The nucleating agent Si_3N_4 could not be deagglomerated well in camphene. When using it nonetheless, no effective curing could be done, and the sample could not be processed further. While curing with camphorquinone worked fine, samples fabricated with ETPP were frequently deformed or collapsed after sublimation. The ETPP seemed to be reacting with camphene to a non-negligible extent which resulted in too little left for sufficient photocuring. This led to low reproducibility of properties measured with several different characterization techniques.

p-Xylene showed excellent miscibility and non-reactivity with all chemicals necessary for the process. Directional crystal growth was observed during freeze casting although the orientation of the growing p-xylene crystals was not parallel to the freezing direction. A very coarse structure was obtained regardless if a nucleating agent was present or not. Very little connective ceramic bridging between the coarse crystals as well as the tilted growth direction during freeze-casting resulted in samples, which were very delicate to handle. Properties like compressive strength were affected detrimentally because of these reasons. Supercooling could not be eliminated with any tested nucleating agent, including a roughened surface of the freeze-casting plate.

Dimethyl carbonate showed excellent miscibility with all chemicals necessary for the process. It is not clear though, if it acted non-reactive towards all educts present in the casting solution. Upon addition of dimethyl carbonate, a faint colour change of the solution could be witnessed. Because the purity of the educt is unknown and dimethyl carbonate sensitive to H_2O and decomposition resulting thereof,

other substances could have caused this behaviour. The sublimation step proved to be a challenge because the removal of the sample from the mould after curing and putting it into the vacuum desiccator had to be done very quickly. If not, destruction of the sample would follow. The microstructure of the samples obtained with dimethyl carbonate as a structuring agent showed lamellar pore morphology. The tested nucleating agents didn´t seem to cause a relevant and clearly visible change in the pore structure. The porosity was directional, with large unidirectional parts pervading the sample.

Bornyl acetate showed excellent miscibility and non-reactivity with all chemicals necessary for the process. Directional crystal growth could be observed with an orientation diverging from the freezing direction to some extent. Sublimation had to be carried out in a freeze-dryer because the vacuum grease used for vacuum desiccators is not compatible with bornyl acetate. Of all the tested solvents, the addition of nucleating agents had by far the largest effect on the pore morphology of the bornyl acetate samples. Depending on the PSZ/TT loading, an addition of Si_3N_4 will not only refine the structure, but also change the structure type. Samples with a loading of 15 – 30 wt% show spiral-like and circular-shaped pores with Si_3N_4. A slight increase of directionality can also be witnessed. When the nucleating agent is left out or loading is higher than 30 wt%, the pores are predominantly lamellar. Because bornyl acetate responds in a very interesting way to the addition of Si_3N_4, a special focus was kept on this structuring agent. Samples with different PSZ/TT loading and varying Si_3N_4 content were fabricated to study the influence of said parameters on pore morphology, permeability, density and porosity. An almost linear increase of apparent porosity can be witnessed when the loading is reduced. Increased loading on the other hand results in an almost linear increase of bulk density. Darcian and Non-Darcian permeability sinks with higher loadings, caused by the smaller pore opening diameters.

Loss of mass and linear shrinkage fluctuated to some extent for all the tested solvents. A specific ranking could not be made though, because the extent of introduced measurement errors due to the fragility of the samples is unclear. The solvent should ideally be completely removed before thermal post-curing and pyrolysis, which would then result in little to no influence of the solvent in mass loss and linear shrinkage of the final ceramic. The delicate structure of the pyrolyzed samples most probably was the major cause for the fluctuations. This is because small bits would easily break off during measurements. Freezing front velocities were measured for p-xylene, dimethyl carbonate and bornyl acetate when no nucleating agent was present. At a cooling rate of 8 K/min the recorded range of freezing front velocities spans an interval of 0.84 – 0.98 mm/min. These values might be different for samples containing nucleating agents. The extreme turbidity caused by them made a tracking of the freezing front nearly impossible.
The source materials building the structure of the final ceramic always were PSZ and TT with a mass ratio of 2.7 : 1 (equal to a molar ratio of vinyl groups : thiol groups = 1 : 1). Testing of other ratios with vinyl groups/thiol groups > 1 yielded worse results in terms of polymerization behaviour.

The speed and efficiency of the photopolymerization reaction was tested using differential photocalorimetry measurements at -10 °C. This low temperature was chosen to simulate photocuring conditions during sample fabrication. 95 % of the reaction had finished after less than two minutes, regardless of the structuring agent. The energy release was lowest for camphene though, which indicates some involvement of the solvent during the curing process.

The entropic terms of the Jackson α-factor were determined by measuring enthalpy of fusion and melting temperature of the used solvents and compared with the observed microstructure of the

ceramic. The values obtained were in good agreement with the pore morphology with higher ones indicating higher anisotropy and faceted growth. The lowest value was measured for camphene, which also shows the lowest anisotropy in the crystal structure. The determined values must be treated with caution though, because they differ widely from the literature values. The most probable reasons for this discrepancy are impurities and measurement errors arising from the high vapor pressures of the structuring agents.

Bulk density, apparent solid density and apparent porosity were determined by using the Immersion test method. The apparent solid density showed values around 2 g/cm³. A significant influence of the solvent on this property could not be proven. Apparent porosity was highest for p-xylene, followed by dimethyl carbonate, bornyl acetate and camphene in descending order. As expected, bulk density showed the opposite order. For this trend to manifest itself, PSZ/TT loading must be kept constant. The addition of nucleating agent did not affect bulk density and apparent porosity much. Porosity measured by Hg intrusion showed values around 65 % for bornyl acetate (67.0 %), dimethyl carbonate (65.7 %) and p-xylene (65.8 %). Camphene deviated significantly with a value of 53.3 %. The median pore opening size of bornyl acetate samples with 25 wt% PSZ/TT loading was highly affected by the addition of nucleating agents (43.8 µm without and 25.8 µm with 0.1 wt% Si_3N_4). Higher loadings caused the pore size to shrink.

Permeability values deviate with several orders of magnitude, depending on the solvent. Camphene samples display the lowest Darcian and Non-Darcian permeability values by far. A trend of decreasing Darcian permeability starting with p-xylene, followed by dimethyl carbonate and bornyl acetate, could be observed. Non-Darcian permeability fluctuates around 10^{-5} m for the three just mentioned solvents. Compressive strength is highest for camphene with 50.76 ± 17.53 MPa, followed by bornyl acetate with 8.23 ± 0.64 MPa, dimethyl carbonate with 3.21 ± 0.66 MPa and p-xylene with 0.69 ± 0.01 MPa.

Supercooling was a problem arising with every solvent apart from camphene. As the top and bottom of the samples were cut off after curing, dimethyl carbonate and p-xylene could be handled quite well. Bornyl acetate though showed catastrophic supercooling, which was ultimately dealt with by providing nucleating seeds of the structuring agent itself by pre-freezing a small layer onto the freeze-casting plate. Except for camphene yielding a dendritic pore morphology, all three other solvents produced highly directional mostly lamellar pores. The nucleating agent of choice (Si_3N_4) had a big impact only on the bornyl acetate pore size and morphology. Previously not seen spiral-like and tubular pores were appearing upon addition of Si_3N_4.

6.2 Outlook

The macroporous ceramics fabricated during this thesis could be tested for applications like heterogeneous catalysis or filtering. Cross-linking agents other than tetrathiol, which was solely used during this thesis, could be tested. This way, oxygen input into the final ceramic could be potentially reduced. The search after a structuring agent, which will produce tubular unidirectional porosity, could be carried on.

Bibliography

1. D.J. Green and P. Colombo, *Cellular Ceramics: Intriguing Structures, Novel Properties, and Innovative Applications.* MRS Bulletin, 2003. **28**(4): p. 296-300.
2. M. Naviroj, P.W. Voorhees, and K.T. Faber, *Suspension- and solution-based freeze casting for porous ceramics.* Journal of Materials Research, 2017. **32**(17): p. 3372-3382.
3. T. Ohji, *Chapter 11.2.2 - Porous Ceramic Materials*, in *Handbook of Advanced Ceramics (Second Edition)*, S. Somiya, Editor. 2013, Academic Press: Oxford. p. 1131-1148.
4. R. Obmann, S. Schörpf, C. Gorsche, R. Liska, T. Fey, T. Konegger, *Porous polysilazane-derived ceramic structures generated through photopolymeriaztion-assisted solidification templating.* Accepted for publication in Journal of the European Ceramic Society, 2018
5. P. Colombo, G. Mera, R. Riedel, and G.D. Sorarù, *Polymer-Derived Ceramics: 40 Years of Research and Innovation in Advanced Ceramics.* Journal of the American Ceramic Society, 2010. **93**(7): p. 1805-1837.
6. F.S. Kipping and J.E. Sands, *XCIII.—Organic derivatives of silicon. Part XXV. Saturated and unsaturated silicohydrocarbons, Si4Ph8.* Journal of the Chemical Society, Transactions, 1921. **119**(0): p. 830-847.
7. R.D. Miller, *Polysilanes—A New Look at Some Old Materials.* Angewandte Chemie International Edition in English, 1989. **28**(12): p. 1733-1740.
8. C. Aitken, J.F. Harrod, and E. Samuel, *Polymerization of primary silanes to linear polysilanes catalyzed by titanocene derivatives.* Journal of Organometallic Chemistry, 1985. **279**(1): p. C11-C13.
9. C.T. Aitken, J.F. Harrod, and E. Samuel, *Identification of some intermediates in the titanocene-catalyzed dehydrogenative coupling of primary organosilanes.* Journal of the American Chemical Society, 1986. **108**(14): p. 4059-4066.
10. M. Birot, J.-P. Pillot, and J. Dunogues, *Comprehensive Chemistry of Polycarbosilanes, Polysilazanes, and Polycarbosilazanes as Precursors of Ceramics.* Chemical Reviews, 1995. **95**(5): p. 1443-1477.
11. E. Kroke, Y.-L. Li, C. Konetschny, E. Lecomte, C. Fasel, and R. Riedel, *Silazane derived ceramics and related materials.* Materials Science and Engineering: R: Reports, 2000. **26**(4): p. 97-199.
12. S.D. Brewer and C.P. Haber, *Alkylsilazanes and Some Related Compounds.* Journal of the American Chemical Society, 1948. **70**(11): p. 3888-3891.
13. D.L. Bailey, L.H. Sommer, and F.C. Whitmore, *Some Reactions of Trialkylaminosilanes.* Journal of the American Chemical Society, 1948. **70**(1): p. 435-436.
14. H.-H. Moretto, M. Schulze, and G. Wagner, *Silicones*, in *Ullmann's Encyclopedia of Industrial Chemistry*. 2000.
15. A. Lavedrine, D. Bahloul, P. Goursat, N. Choong Kwet Yive, R. Corriu, D. Leclerq, H. Mutin, and A. Vioux, *Pyrolysis of polyvinylsilazane precursors to silicon carbonitride.* Journal of the European Ceramic Society, 1991. **8**(4): p. 221-227.
16. C.M. Gerardin, F. Taulelle, and J. Livage, *Structural Characterization of Silicon Carbonitride Ceramics from Polymeric Precursors using Nuclear Magnetic Resonance.* MRS Proceedings, 2011. **287**: p. 233.
17. K.A. Andrianov and G.V. Kotrelev, *Synthesis and properties of organocyclosilazanes.* Journal of Organometallic Chemistry, 1967. **7**(2): p. 217-225.
18. J. He, M. Scarlete, and J.F. Harrod, *Silicon Nitride and Silicon Carbonitride by the Pyrolysis of Poly(methylsiladiazane).* Journal of the American Ceramic Society, 1995. **78**(11): p. 3009-3017.

19. G. Mera, R. Riedel, F. Poli, and K. Müller, *Carbon-rich SiCN ceramics derived from phenyl-containing poly(silylcarbodiimides).* Journal of the European Ceramic Society, 2009. **29**(13): p. 2873-2883.
20. S. Otoishi and Y. Tange, *Growth rate and morphology of silicon carbide whiskers from polycarbosilane.* Journal of Crystal Growth, 1999. **200**(3): p. 467-471.
21. K.B. Schwartz and D.J. Rowcliffe, *Modeling Density Contributions in Preceramic Polymer/Ceramic Powder Systems.* Journal of the American Ceramic Society, 1986. **69**(5): p. C-106-C-108.
22. T. Konegger, C.-C. Tsai, H. Peterlik, S.E. Creager, and R.K. Bordia, *Asymmetric polysilazane-derived ceramic structures with multiscalar porosity for membrane applications.* Microporous and Mesoporous Materials, 2016. **232**: p. 196-204.
23. Y.D. Blum, K.B. Schwartz, and R.M. Laine, *Preceramic polymer pyrolysis.* Journal of Materials Science, 1989. **24**(5): p. 1707-1718.
24. R. Riedel, G. Passing, H. Schönfelder, and R.J. Brook, *Synthesis of dense silicon-based ceramics at low temperatures.* Nature, 1992. **355**: p. 714.
25. R. Riedel, G. Mera, R. Hauser, and A. Klonczynski, *Silicon-Based Polymer-Derived Ceramics: Synthesis Properties and Applications - A Review.* Journal of the Ceramic Society of Japan, 2006. **114**(1330): p. 425-444.
26. G. Ziegler, H.J. Kleebe, G. Motz, H. Müller, S. Traßl, and W. Weibelzahl, *Synthesis, microstructure and properties of SiCN ceramics prepared from tailored polymers.* Materials Chemistry and Physics, 1999. **61**(1): p. 55-63.
27. G.D. Sorarù, S. Modena, E. Guadagnino, P. Colombo, J. Egan, and C. Pantano, *Chemical Durability of Silicon Oxycarbide Glasses.* Journal of the American Ceramic Society, 2002. **85**(6): p. 1529-1536.
28. R. Gadow and F. Kern, *Liquid-Phase Coating of Carbon Fibers with Pre-Ceramic Polymer Precursors: Process and Applications.* Advanced Engineering Materials, 2002. **4**(11): p. 883-886.
29. M. Fukushima, Y. Zhou, H. Miyazaki, Y.-i. Yoshizawa, K. Hirao, Y. Iwamoto, S. Yamazaki, and T. Nagano, *Microstructural Characterization of Porous Silicon Carbide Membrane Support With and Without Alumina Additive.* Journal of the American Ceramic Society, 2006. **89**(5): p. 1523-1529.
30. U.F. Vogt, M. Gorbar, P. Dimopoulos-Eggenschwiler, A. Broenstrup, G. Wagner, and P. Colombo, *Improving the properties of ceramic foams by a vacuum infiltration process.* Journal of the European Ceramic Society, 2010. **30**(15): p. 3005-3011.
31. H.-Y. Song, S. Islam, and B.-T. Lee, *A Novel Method to Fabricate Unidirectional Porous Hydroxyapatite Body Using Ethanol Bubbles in a Viscous Slurry.* Journal of the American Ceramic Society, 2008. **91**(9): p. 3125-3127.
32. T. Banno, Y. Yamada, and H. Nagae, *Fabrication of porous alumina ceramics by simultaneous thermal gas generating and thermal slurry solidification.* Journal of the Ceramic Society of Japan, 2009. **117**(1365): p. 713-716.
33. P. Colombo and M. Modesti, *Silicon Oxycarbide Ceramic Foams from a Preceramic Polymer.* Journal of the American Ceramic Society, 1999. **82**(3): p. 573-578.
34. G.-J. Zhang, J.-F. Yang, and T. Ohji, *Fabrication of Porous Ceramics with Unidirectionally Aligned Continuous Pores.* Journal of the American Ceramic Society, 2001. **84**(6): p. 1395-1397.
35. S. Gaydardzhiev, H. Gusovius, V. Wilker, and P. Ay, *Gel-casted porous Al2O3 ceramics by use of natural fibres as pore developers.* Journal of Porous Materials, 2008. **15**(4): p. 475-480.

36. S. Deville, E. Saiz, and A.P. Tomsia, *Ice-templated porous alumina structures.* Acta Materialia, 2007. **55**(6): p. 1965-1974.
37. T. Waschkies, R. Oberacker, and M.J. Hoffmann, *Investigation of structure formation during freeze-casting from very slow to very fast solidification velocities.* Acta Materialia, 2011. **59**(13): p. 5135-5145.
38. D. Ghosh, M. Banda, H. Kang, and N. Dhavale, *Platelets-induced stiffening and strengthening of ice-templated highly porous alumina scaffolds.* Scripta Materialia, 2016. **125**: p. 29-33.
39. W.W. Mullins and R.F. Sekerka, *Stability of a Planar Interface During Solidification of a Dilute Binary Alloy*, in *Dynamics of Curved Fronts*, P. Pelcé, Editor. 1988, Academic Press: San Diego. p. 345-352.
40. S.M. Miller, X. Xiao, and K.T. Faber, *Freeze-cast alumina pore networks: Effects of freezing conditions and dispersion medium.* Journal of the European Ceramic Society, 2015. **35**(13): p. 3595-3605.
41. Y. Chino and D.C. Dunand, *Directionally freeze-cast titanium foam with aligned, elongated pores.* Acta Materialia, 2008. **56**(1): p. 105-113.
42. B.-H. Yoon, E.-J. Lee, H.-E. Kim, and Y.-H. Koh, *Highly Aligned Porous Silicon Carbide Ceramics by Freezing Polycarbosilane/Camphene Solution.* Journal of the American Ceramic Society, 2007. **90**(6): p. 1753-1759.
43. S. Deville, *Freeze-Casting of Porous Ceramics: A Review of Current Achievements and Issues.* Advanced Engineering Materials, 2008. **10**(3): p. 155-169.
44. T. Fukasawa, M. Ando, T. Ohji, and S. Kanzaki, *Synthesis of Porous Ceramics with Complex Pore Structure by Freeze-Dry Processing.* Journal of the American Ceramic Society, 2001. **84**(1): p. 230-232.
45. B.-H. Yoon, C.-S. Park, H.-E. Kim, and Y.-H. Koh, *In-situ fabrication of porous hydroxyapatite (HA) scaffolds with dense shells by freezing HA/camphene slurry.* Materials Letters, 2008. **62**(10): p. 1700-1703.
46. S. Deville, E. Saiz, and A.P. Tomsia, *Freeze casting of hydroxyapatite scaffolds for bone tissue engineering.* Biomaterials, 2006. **27**(32): p. 5480-5489.
47. J.-W. Moon, H.-J. Hwang, M. Awano, and K. Maeda, *Preparation of NiO–YSZ tubular support with radially aligned pore channels.* Materials Letters, 2003. **57**(8): p. 1428-1434.
48. Y.-H. Koh, J.-J. Sun, and H.-E. Kim, *Freeze casting of porous Ni–YSZ cermets.* Materials Letters, 2007. **61**(6): p. 1283-1287.
49. S.W. Sofie, *Fabrication of Functionally Graded and Aligned Porosity in Thin Ceramic Substrates With the Novel Freeze–Tape-Casting Process.* Journal of the American Ceramic Society, 2007. **90**(7): p. 2024-2031.
50. L. Ren, Y.-P. Zeng, and D. Jiang, *Fabrication of Gradient Pore TiO2 Sheets by a Novel Freeze–Tape-Casting Process.* Journal of the American Ceramic Society, 2007. **90**(9): p. 3001-3004.
51. T. Fukasawa, M. Ando, and T. Ohji, *Filtering Properties of Porous Ceramics with Unidirectionally Aligned Pores.* Journal of the Ceramic Society of Japan, 2002. **110**(1283): p. 627-631.
52. S.R. Mukai, H. Nishihara, and H. Tamon, *Formation of monolithic silica gel microhoneycombs (SMHs) using pseudosteady state growth of microstructural ice crystals.* Chemical Communications, 2004(7): p. 874-875.
53. H. Nishihara, S.R. Mukai, Y. Fujii, T. Tago, T. Masuda, and H. Tamon, *Preparation of monolithic SiO2–Al2O3 cryogels with inter-connected macropores through ice templating.* Journal of Materials Chemistry, 2006. **16**(31): p. 3231-3236.

54. J. Tang, Y.F. Chen, H. Wang, H.L. Liu, and Q.S. Fan, *Preparation of Oriented Porous Silicon Carbide Bodies by Freeze-Casting Process.* Key Engineering Materials, 2004. **280-283**: p. 1287-1290.
55. R. Chen, C.-A. Wang, Y. Huang, L. Ma, and W. Lin, *Ceramics with Special Porous Structures Fabricated by Freeze-Gelcasting: Using tert-Butyl Alcohol as a Template.* Journal of the American Ceramic Society, 2007. **90**(11): p. 3478-3484.
56. M. Naviroj, S.M. Miller, P. Colombo, and K.T. Faber, *Directionally aligned macroporous SiOC via freeze casting of preceramic polymers.* Journal of the European Ceramic Society, 2015. **35**(8): p. 2225-2232.
57. S. Deville, E. Saiz, R.K. Nalla, and A.P. Tomsia, *Freezing as a Path to Build Complex Composites.* Science, 2006. **311**(5760): p. 515.
58. S. Deville, E. Saiz, and A.P. Tomsia, *Using Ice to Mimic Nacre: From Structural Applications to Artificial Bone*, in *Handbook of Biomineralization*, P. Behrens and E. Baeuerlein, Editors. 2007, Wiley-VCH: Weinheim.
59. S.-H. Lee, S.-H. Jun, H.-E. Kim, and Y.-H. Koh, *Fabrication of Porous PZT–PZN Piezoelectric Ceramics With High Hydrostatic Figure of Merits Using Camphene-Based Freeze Casting.* Journal of the American Ceramic Society, 2007. **90**(9): p. 2807-2813.
60. P. Bennema, *Handbook on Crystal Growth*. 1993, Amsterdam: North-Holland.
61. X.-Y. Liu and P. Bennema, *Theoretical consideration of the growth morphology of crystals.* Physical Review B, 1996. **53**(5): p. 2314-2325.
62. K.A. Jackson, *Constitutional supercooling surface roughening.* Journal of Crystal Growth, 2004. **264**(4): p. 519-529.
63. J.-P. Fouassier and Lalevée, *Photoinitiators for Polymer Synthesis: Scope, Reactivity and Efficiency*. First ed. 2012: Wiley-VCH.
64. J.-P. Fouassier, X. Allonas, and J. Lalevée, *Polymerization under Light and Other External Stimuli*, in *Macromolecular Engineering*, K. Matyjaszewski, Y. Gnanou, and L. Leibler, Editors. 2011. p. 634-672.
65. M.R. Zonca, B. Falk, and J.V. Crivello, *LED-Induced Thiol–ene Photopolymerizations.* Journal of Macromolecular Science, Part A, 2004. **41**(7): p. 741-756.
66. C.E. Hoyle and C.N. Bowman, *Thiol–Ene Click Chemistry.* Angewandte Chemie International Edition, 2010. **49**(9): p. 1540-1573.
67. N.B. Cramer, S.K. Reddy, A.K. O'Brien, and C.N. Bowman, *Thiol−Ene Photopolymerization Mechanism and Rate Limiting Step Changes for Various Vinyl Functional Group Chemistries.* Macromolecules, 2003. **36**(21): p. 7964-7969.
68. C.E. Hoyle, T.Y. Lee, and T. Roper, *Thiol–enes: Chemistry of the past with promise for the future.* Journal of Polymer Science Part A: Polymer Chemistry, 2004. **42**(21): p. 5301-5338.
69. S.K. Reddy, N.B. Cramer, T. Cross, R. Raj, and C.N. Bowman, *Polymer-Derived Ceramic Materials from Thiol-ene Photopolymerizations.* Chemistry of Materials, 2003. **15**(22): p. 4257-4261.
70. C.N. Bowman and C.J. Kloxin, *Toward an enhanced understanding and implementation of photopolymerization reactions.* AIChE Journal, 2008. **54**(11): p. 2775-2795.
71. T.M. Roper, T.Y. Lee, C.A. Guymon, and C.E. Hoyle, *In Situ Characterization of Photopolymerizable Systems Using a Thin-Film Calorimeter.* Macromolecules, 2005. **38**(24): p. 10109-10116.
72. C.N. Bowman and N.A. Peppas, *Coupling of kinetics and volume relaxation during polymerizations of multiacrylates and multimethacrylates.* Macromolecules, 1991. **24**(8): p. 1914-1920.

73. H. Lu, J.W. Stansbury, and C.N. Bowman, *Towards the elucidation of shrinkage stress development and relaxation in dental composites.* Dental Materials, 2004. **20**(10): p. 979-986.
74. K.S. Anseth, C.M. Wang, and C.N. Bowman, *Kinetic evidence of reaction diffusion during the polymerization of multi(meth)acrylate monomers.* Macromolecules, 1994. **27**(3): p. 650-655.
75. C. Decker, *Kinetic Study and New Applications of UV Radiation Curing.* Macromolecular Rapid Communications, 2002. **23**(18): p. 1067-1093.
76. G.P. Simon, P.E.M. Allen, D.J. Bennett, D.R.G. Williams, and E.H. Williams, *Nature of residual unsaturation during cure of dimethacrylates examined by CPPEMAS carbon-13 NMR and simulation using a kinetic gelation model.* Macromolecules, 1989. **22**(9): p. 3555-3561.
77. A.R. Kannurpatti, J.W. Anseth, and C.N. Bowman, *A study of the evolution of mechanical properties and structural heterogeneity of polymer networks formed by photopolymerizations of multifunctional (meth)acrylates.* Polymer, 1998. **39**(12): p. 2507-2513.
78. J.D. Menczel and R.B. Prime, *Thermal Analysis of Polymers: Fundamentals and Applications*. 2008: John Wiley & Sons, Inc.
79. ProLight-Opto, *PM2L-3LLx-LC 3W UV Power LED Technical Datasheet Version: 1.9*.
80. https://www.tme.eu/en/details/pm2l-3lle-lc/uv-leds/prolight-opto/. [cited 2018 -08-21].
81. Merck, *Safety Data Sheet for (+)-Camphene (Article number 820254, Lot number S7165554)*
82. W.M. Haynes, *Handbook of Chemistry and Physics*. 96th ed. 2015, Boca Raton: CRC Press.
83. Alfa Aesar, *Safety Data Sheet for L-(-)-Bornyl acetate (Article number B22957, Lot number 10210378)*
84. European Standard EN 623, *Advanced technical ceramics - Monolithic ceramics - General and textural properties - Part 2: Determination of density and porosity: EN 623-2.* 1993.
85. M.D. de Mello Innocentini, P. Sepulveda, and F. dos Santos Ortega, *Permeability*, in *Cellular Ceramics*, M. Scheffler and P. Colombo, Editors. 2005, Wiley-VCH: Weinheim. p. 313-338.
86. Kion Defense Technologies, Inc., KDT HTT 1800 Technical Data Sheet (Product Code: K-1034)
87. D. Wei, L. Wang, and C. Zhang, *Solid–Liquid Equilibria in Binary Mixtures of 1,8-Cineole with p-Cymene, β-Pinene, and Camphene.* Journal of Chemical & Engineering Data, 2010. **55**(3): p. 1456-1458.
88. https://www.chemeo.com/cid/32-790-9/camphene. *Chemical Properties of Camphene (CAS 79-92-5)*. [cited 2018 -11-16].
89. M.S. Ding, *Liquid–Solid Phase Equilibria and Thermodynamic Modeling for Binary Organic Carbonates.* Journal of Chemical & Engineering Data, 2004. **49**(2): p. 276-282.
90. E.S. Domalski and E.D. Hearing, *Heat Capacities and Entropies of Organic Compounds in the Condensed Phase. Volume III.* Journal of Physical and Chemical Reference Data, 1996. **25**(1): p. 1-525.
91. https://www.chemeo.com/cid/15-368-7/Bicyclo%5B2.2.1%5Dheptan-2-ol%2C%201%2C7%2C7-trimethyl-%2C%20acetate%2C%20%281S-endo%29-. *Chemical Properties of Bicyclo[2.2.1]heptan-2-ol, 1,7,7-trimethyl-, acetate, (1S-endo)- (CAS 5655-61-8)*. [cited 2018 11-16].

Appendix

A.1 Pore opening size distributions measured by Hg-Porosimetry

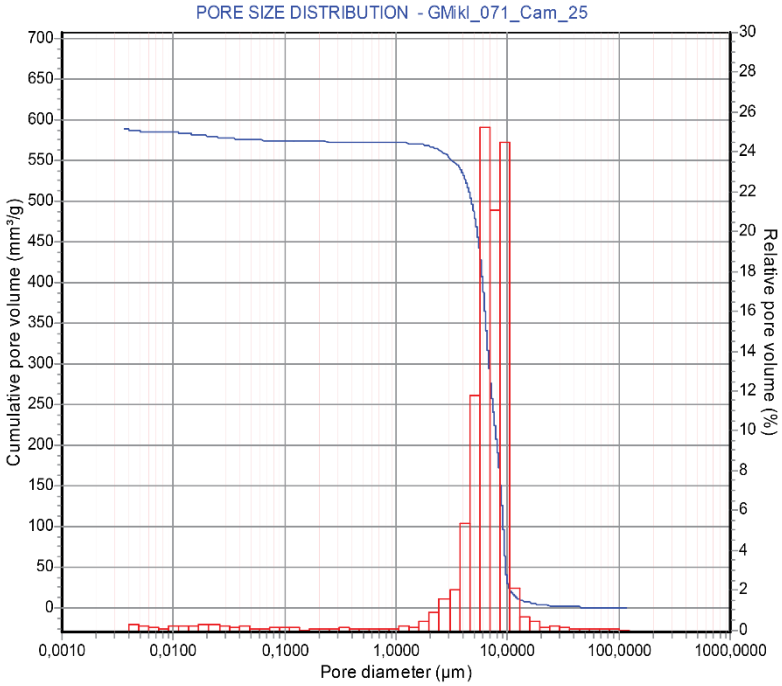

Figure A1: Pore opening size distribution of 071_Cam_25, a camphene sample with a PSZ/TT loading of 25 wt% and no nucleating agent

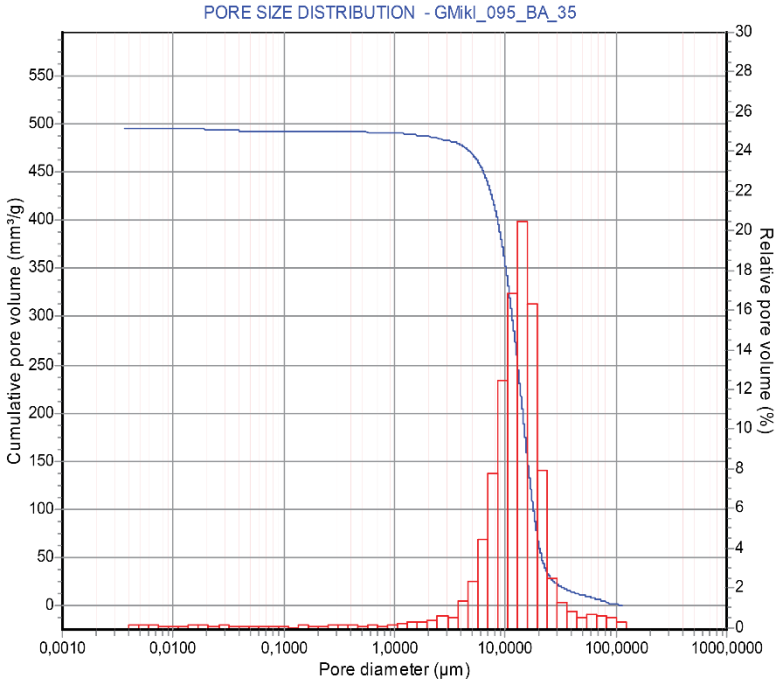

Figure A2: Pore opening size distribution of 095_BA_35, a bornyl acetate sample with a PSZ/TT loading of 35 wt% and 0.2 wt% Si_3N_4

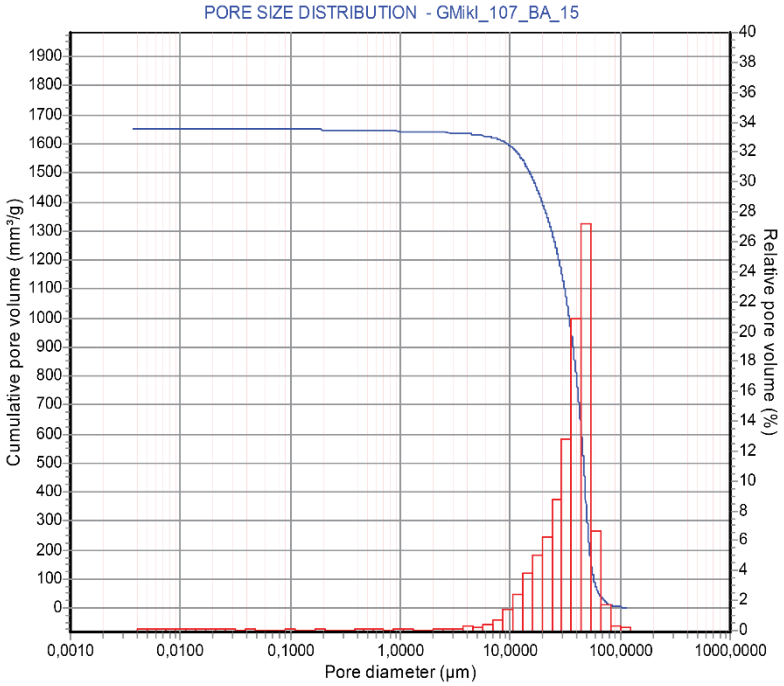

Figure A3: Pore opening size distribution of 107_BA_15, a bornyl acetate sample with a PSZ/TT loading of 15 wt% and 0.2 wt% Si_3N_4

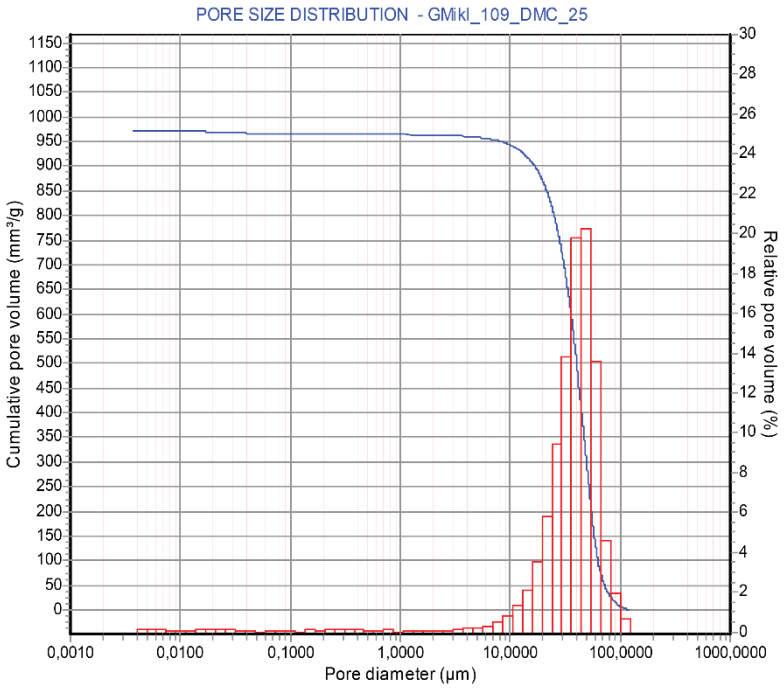

Figure A4: Pore opening size distribution of 109_DMC_25, a dimethyl carbonate sample with a PSZ/TT loading of 25 wt% and 0.1 wt% Si_3N_4

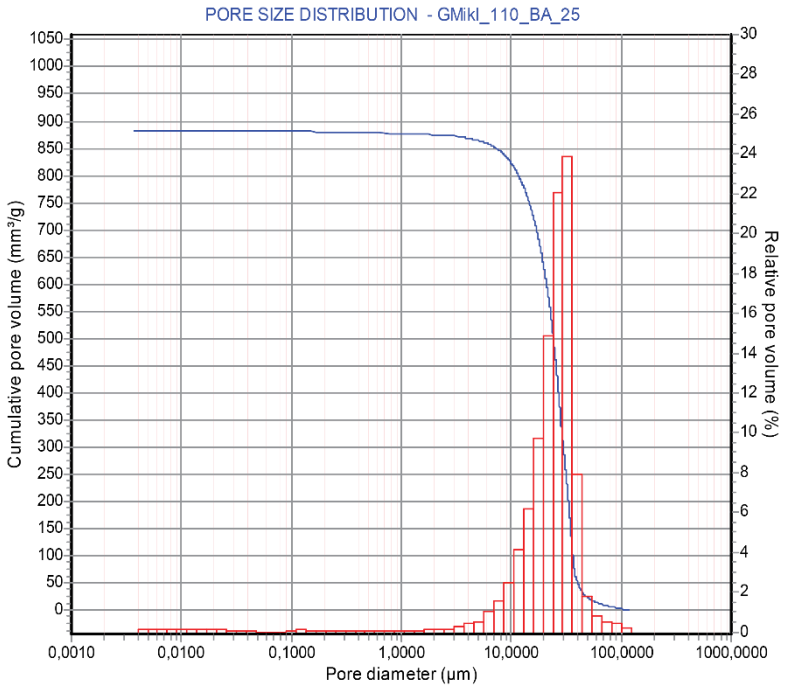

Figure A5: Pore opening size distribution of 110_BA_25, a bornyl acetate sample with a PSZ/TT loading of 25 wt% and 0.1 wt% Si_3N_4

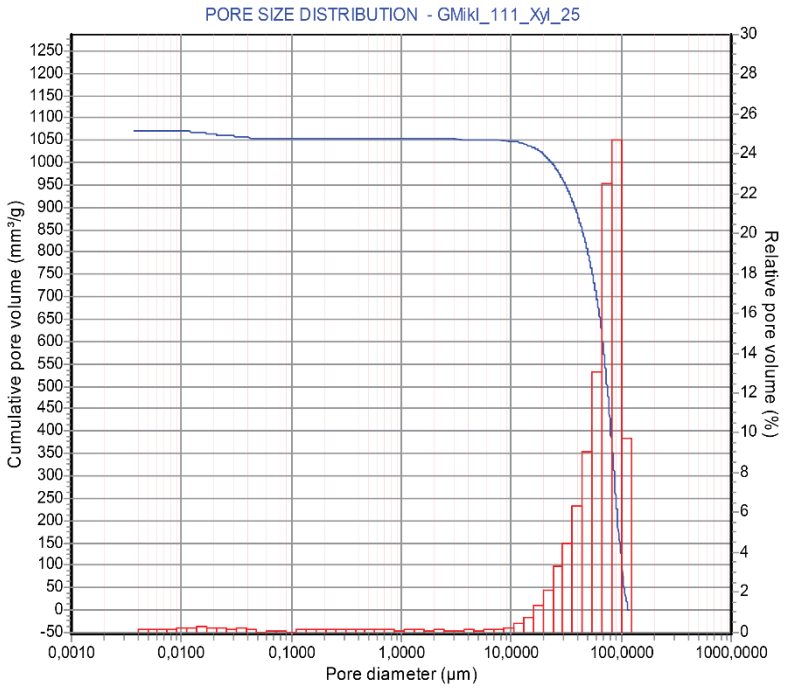

Figure A6: Pore opening size distribution of 111_Xyl_25, a p-xylene sample with a PSZ/TT loading of 25 wt% and 0.1 wt% Si_3N_4

A.2 Gas flow curves from permeability measurements

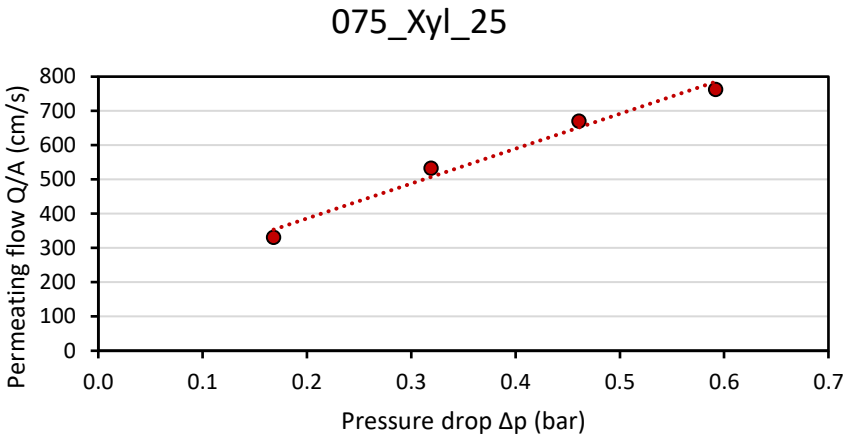

Figure A7: Gas flow curve for 075_Xyl_25, a p-xylene sample with a PSZ/TT loading of 25 wt% and no nucleating agent

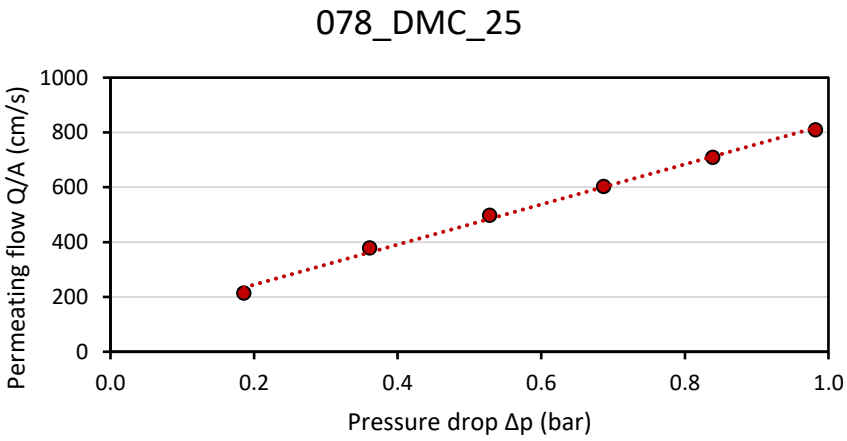

Figure A8: Gas flow curve for 078_DMC_25, a dimethyl carbonate sample with a PSZ/TT loading of 25 wt% and no nucleating agent

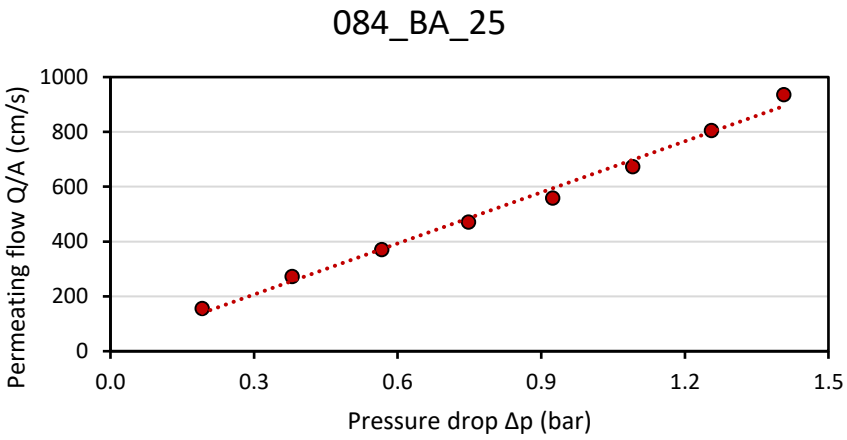

Figure A9: Gas flow curve for 084_BA_25, a bornyl acetate sample with a PSZ/TT loading of 25 wt% and no nucleating agent

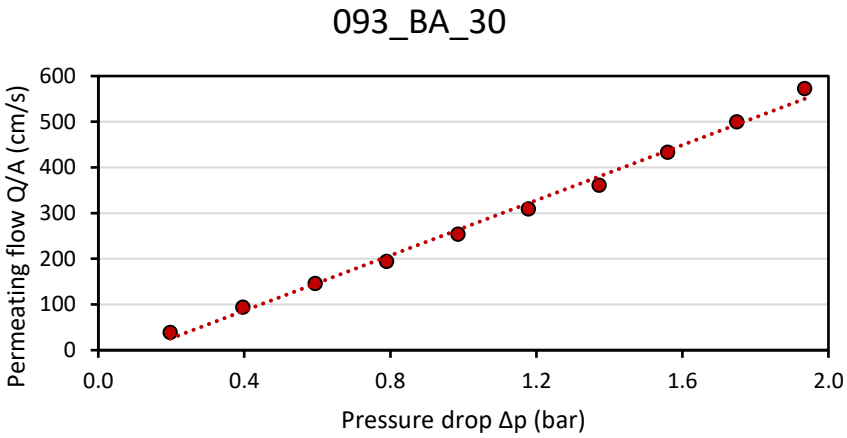

Figure A10: Gas flow curve for 093_BA_30, a bornyl acetate sample with a PSZ/TT loading of 30 wt% and 0.2 wt% Si_3N_4

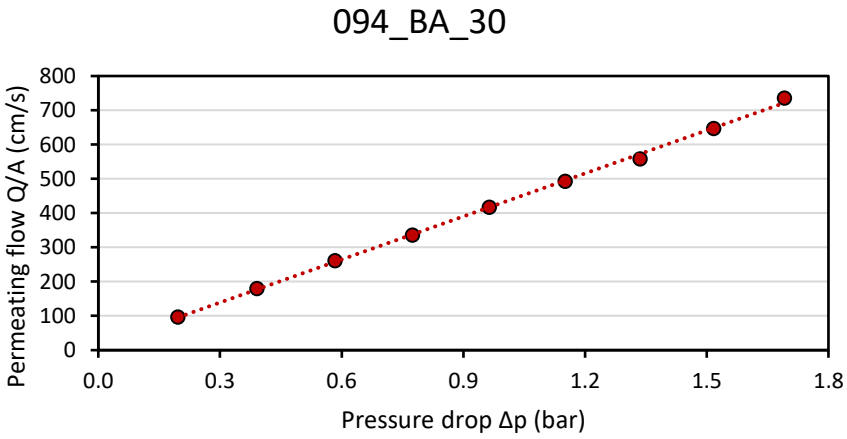

Figure A11: Gas flow curve for 094_BA_30, a bornyl acetate sample with a PSZ/TT loading of 30 wt% and no nucleating agent

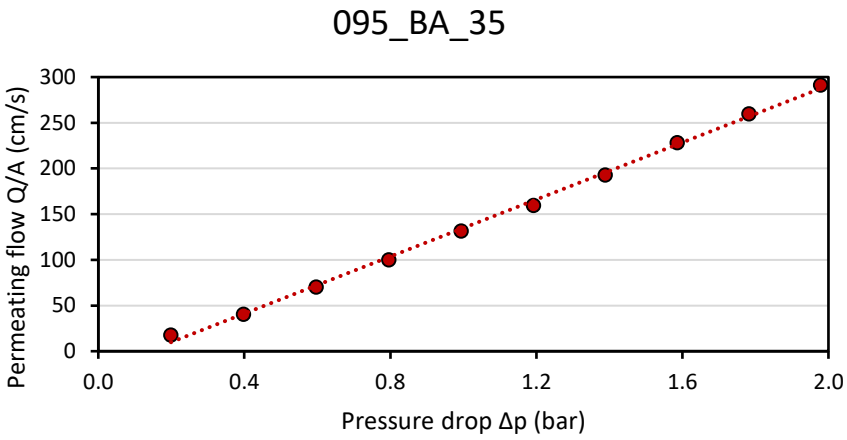

Figure A12: Gas flow curve for 95_BA_35, a bornyl acetate sample with a PSZ/TT loading of 35 wt% and 0.2 wt% Si_3N_4

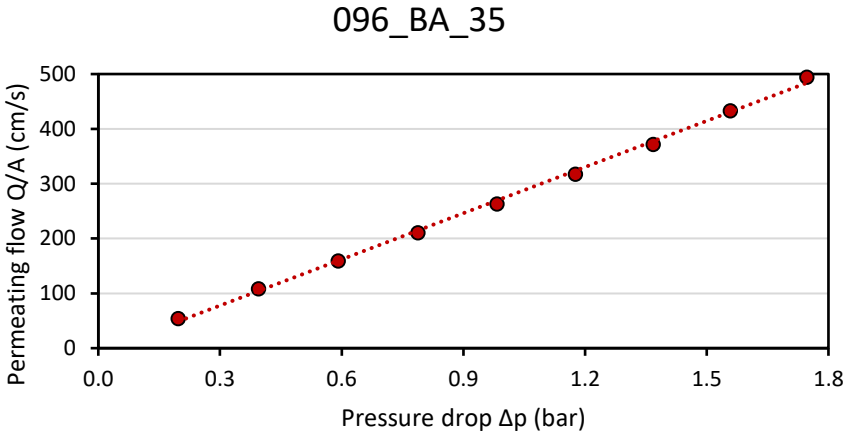

Figure A13: Gas flow curve for 096_BA_35, a bornyl acetate sample with a PSZ/TT loading of 35 wt% and no nucleating agent

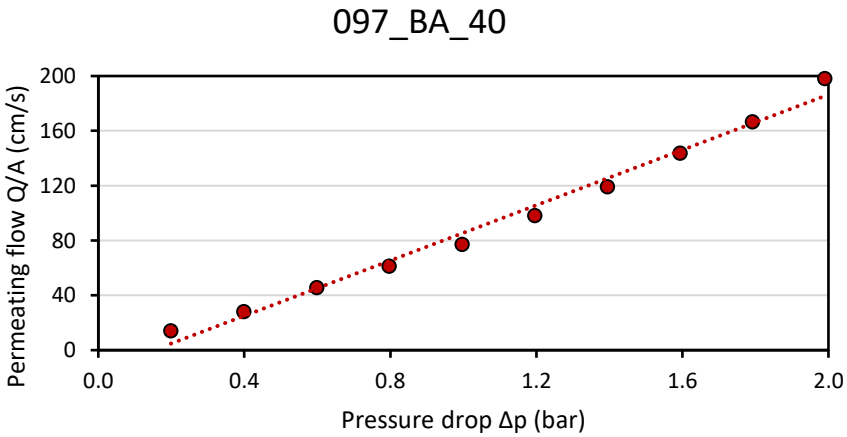

Figure A14: Gas flow curve for 097_BA_40, a bornyl acetate sample with a PSZ/TT loading of 40 wt% and 0.2 wt% Si_3N_4

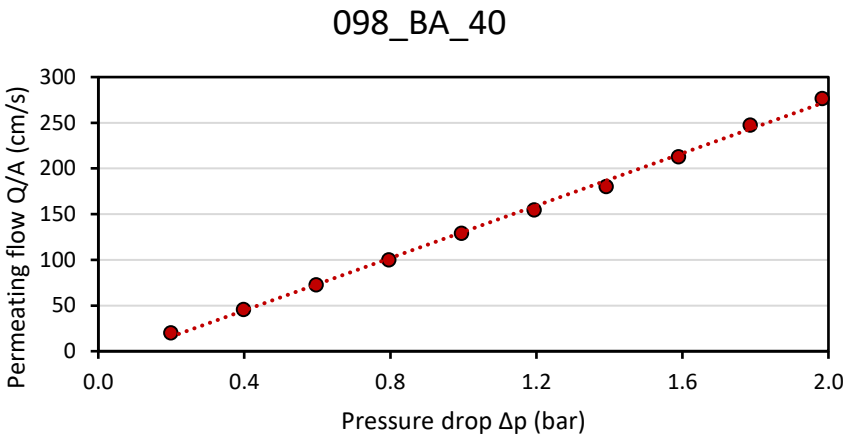

Figure A15: Gas flow curve for 098_BA_40, a bornyl acetate sample with a PSZ/TT loading of 40 wt% and no nucleating agent

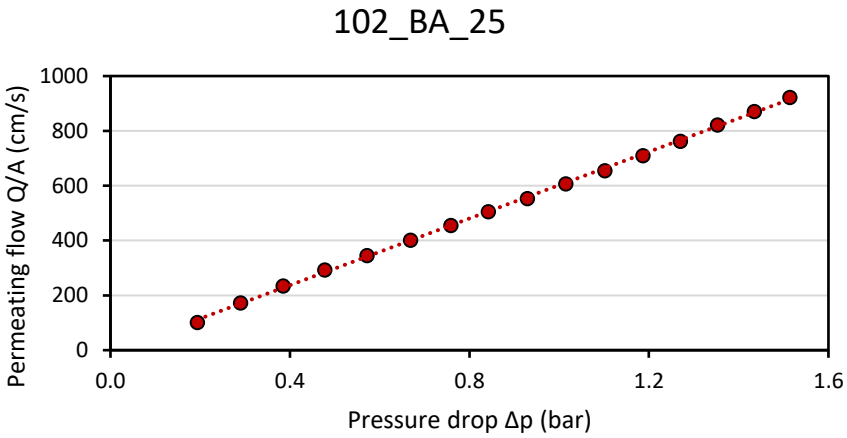

Figure A16: Gas flow curve for 102_BA_25, a bornyl acetate sample with a PSZ/TT loading of 25 wt% and 0.2 wt% Si_3N_4

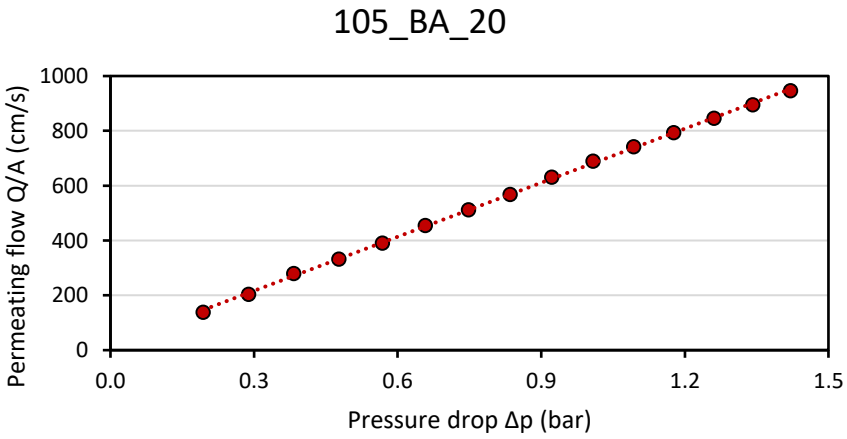

Figure A17: Gas flow curve for 105_BA_20, a bornyl acetate sample with a PSZ/TT loading of 20 wt% and 0.2 wt% Si_3N_4

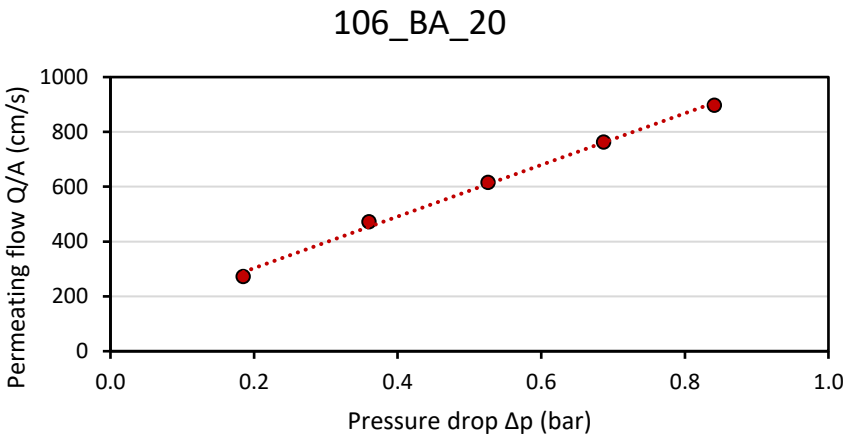

Figure A18: Gas flow curve for 106_BA_20, a bornyl acetate sample with a PSZ/TT loading of 20 wt% and no nucleating agent

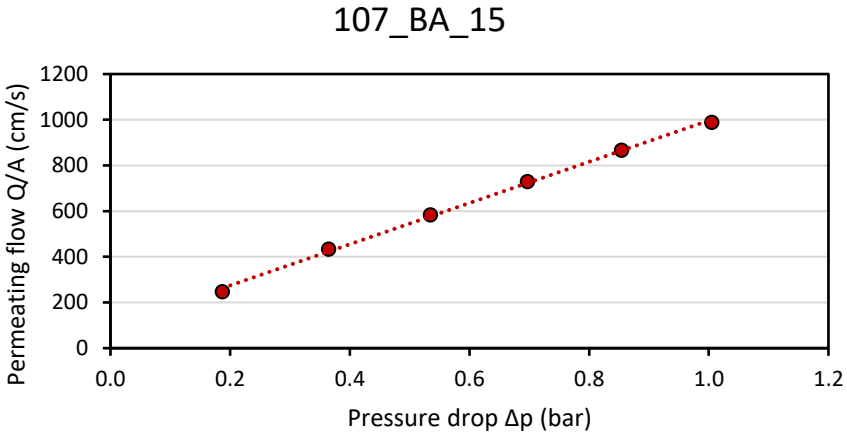

Figure A19: Gas flow curve for 107_BA_15, a bornyl acetate sample with a PSZ/TT loading of 15 wt% and 0.2 wt% Si_3N_4

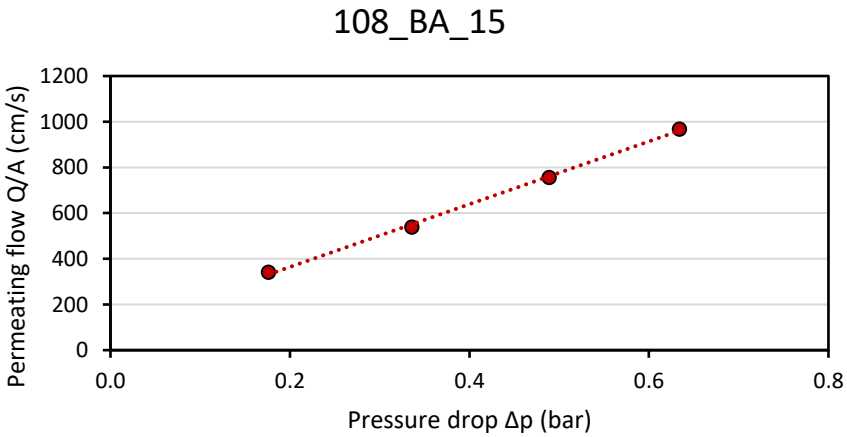

Figure A20: Gas flow curve for 108_BA_15, a bornyl acetate sample with a PSZ/TT loading of 15 wt% and no nucleating agent

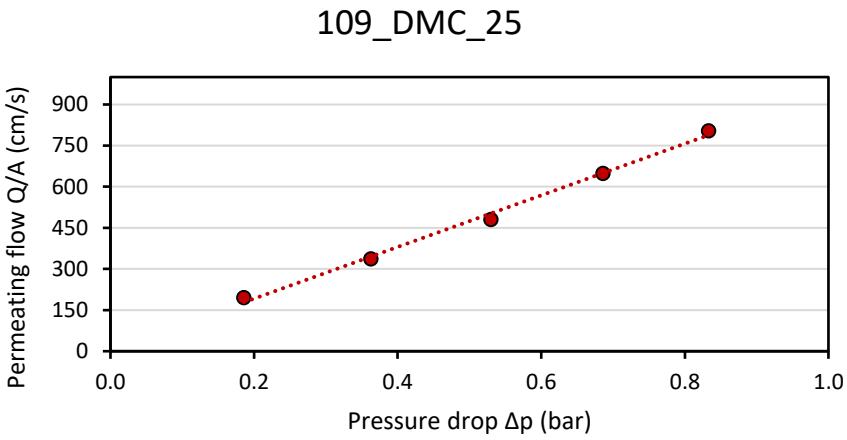

Figure A21: Gas flow curve for 109_DMC_25, a dimethyl carbonate sample with a PSZ/TT loading of 25 wt% and 0.1 wt% Si_3N_4

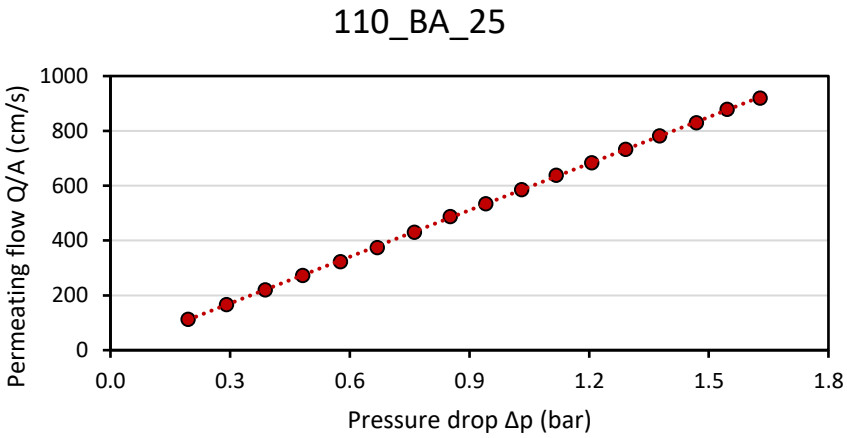

Figure A22: Gas flow curve for 110_BA_25, a bornyl acetate sample with a PSZ/TT loading of 25 wt% and 0.1 wt% Si_3N_4

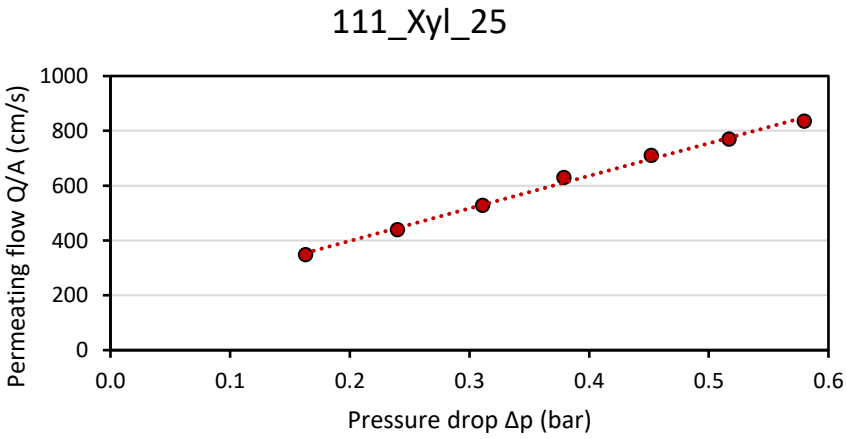

Figure A23: Gas flow curve for 111_Xyl_25, a p-xylene sample with a PSZ/TT loading of 25 wt% and 0.1 wt% Si_3N_4

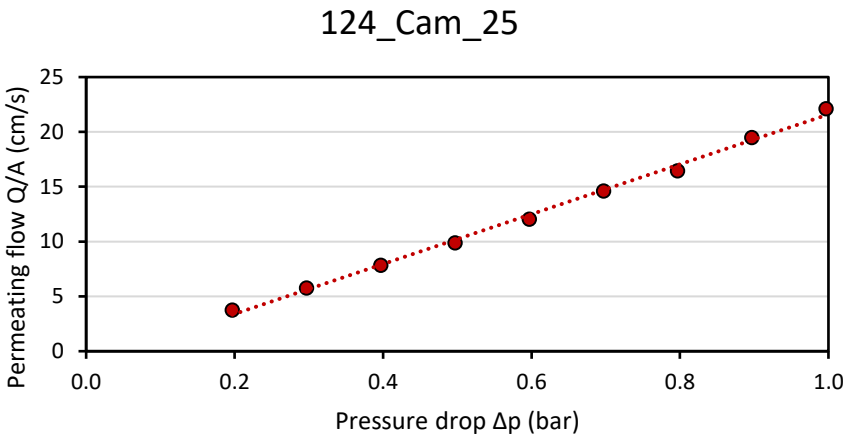

Figure A24: Gas flow curve for 124_Cam_25, a camphene sample with a PSZ/TT loading of 25 wt% and no nucleating agent